PHOTOREFRACTIVE PROPERTIES AND APPLICATIONS OF BARIUM TITANATE AND TUNGSTEN BRONZE FERROELECTRICS

Thesis by

George Anthony Rakuljic

In Partial Fulfillment of the Requirements

for the Degree of

Doctor of Philosophy

California Institute of Technology

Pasadena, California

1987

(Submitted May 19, 1987)

To my parents,

Marijan and Katica Rakuljic

ACKNOWLEDGEMENTS

First and foremost I must acknowledge the guidance, support, and supervision provided me by my advisor, Prof. Amnon Yariv. It truly has been both a privilege and a rewarding experience to work in the creative atmosphere of his laboratory. I thank and respect you, Professor Yariv.

Special thanks go to Dr. Ratnakar R. Neurgaonkar, who gave me his expert guidance and generous professional support. Over the past few years, he has not only been an advisor to me, but has also become a friend.

Thanks are also extended to my colleagues Dr. Sze-Keung (Norman) Kwong, Prof. Mark Cronin-Golomb, Mr. Koichi Sayano and Mr. Victor Leyva with whom I have often collaborated on a number of projects. Their assistance and scientific insight proved invaluable.

Finally, I would like to express appreciation to Jana Mercado, who prepared many of the published papers, to Desmond Armstrong for his technical expertise, and to Prof. George R. Rossman for the many wonderful discussions we have had.

ABSTRACT

This thesis is an experimental and theoretical investigation of the photorefractive properties of barium titanate and tungsten bronze ferroelectrics, and applications thereof. In the first part, the physics of the photorefractive effect is presented. The band transport equations are solved for three cases that describe the photorefractive mechanism in a crystal with one photorefractive species and either one or two types of charge carriers, or in a crystal with two photorefractive species, but only one type of charge carrier.

In the second part, the coupled wave theory of two-wave mixing in photorefractive crystals is reviewed. Effects of energy coupling between the two interacting beams are discussed along with experimental methods for determining the two-beam coupling coefficient and the photorefractive response time.

The photorefractive crystals barium titanate, strontium barium niobate, and barium strontium potassium sodium niobate are described in the third part. A summary of their optical, physical and electrical properties is presented for use in subsequent sections of the thesis.

In the fourth part, the photorefractive properties of these crystals are presented. Data from two-beam coupling experiments are used to obtain the two-beam coupling coefficients and the photorefractive response times of the crystals under a variety of experimental conditions. The band transport models are then applied to these results.

Figures of merit are defined in the fifth part that are then used in a comparison of several photorefractive materials, including the barium titanate, the strontium barium niobate, and the barium strontium potassium sodium niobate crystals. Both ferroelectric and non-ferroelectric materials are considered.

In the last part, applications using barium titanate and the tungsten bronze ferroelectrics are described. By using the self-focusing properties of barium titanate and strontium barium niobate, the compensation of nonlinear optical distortions with phase conjugation is demonstrated. A passive phase conjugator that relies on no external mirrors and uses strontium barium niobate as the nonlinear medium is also described. Finally, a thresholding passive phase conjugate mirror is then presented along with several devices that can perform mathematical operations on images such as subtraction and differentiation.

TABLE OF CONTENTS

1. INTRODUCTION

1.1 Photorefractive Materials and Applications

Strictly speaking, one might define a photorefractive medium as a material in which light induces a refractive index change. Over the past fifteen years, however, the term has come to be understood to refer to a much smaller subset of such materials. Photorefractive materials to be considered in this work are those in which absorbed photons cause charge migration (drift, diffusion, hopping, etc.), the distortion of charge results in a space charge field, and the field modulates the refractive index through the electrooptic effect. All photorefractive materials must thus absorb light and have both mobile charges and a nonzero electrooptic coefficient.

Current photorefractive materials consist of electrooptic crystals such as $LiNbO_3$[1], $KNbO_3$[2], $BaTiO_3$[3], $Sr_xBa_{1-x}Nb_2O_6$ (SBN)[4] (ferroelectrics), $Bi_{12}(Si,Ge,Ti)O_{20}$[5,6] (nonferroelectric oxides), and GaAs[7,8], InP[7], CdTe (compound semiconductors). The mobile charge in these materials is provided by a donor (or acceptor) trap system such as provided by iron in two valence states (Fe^{2+} and Fe^{3+}) in $KNbO_3$[2], $LiNbO_3$[9], InP[7], and probably SBN[4] and $BaTiO_3$[10], or by the defect EL2 and EL2+ in nominally undoped GaAs[7].

Photorefractive materials permit construction of unique devices. Optical amplifiers with gain factors of 4000 have been constructed using photorefractive materials and CW

lasers[11]. Efficient self-pumped phase conjugators that are self-starting and require no external pump beams have also been constructed using CW lasers[12,13]. Here the only competing technology is stimulated Brillouin scattering conjugators that usually require pulsed lasers with more than a millijoule per pulse[14].

A wide variety of other applications have been performed in devices constructed from photorefractive materials. These operations include real-time image subtraction[15], beam clean-up[16], beam combining or locking[17], associative memory[18,19,20], threshold detection[21], convolution and correlation[22], edge enhancement[23], holographic storage[3], optical limiters[24], incoherent to coherent conversion, and beam steering[25] or real-time holographic optical interconnection, imaging of phase objects[26], and rf signal correlation[27].

A number of factors appear to be hindering the conversion of these prototypical devices into commercial products. First, not all photorefractive materials have a large enough nonlinearity to efficiently perform these operations. Second, commercial availability of materials with large nonlinearities is limited. To be specific, $BaTiO_3$, which is available from one commercial supplier, has been used for many of these experiments. Other materials with large nonlinearities, such as $KNbO_3$, SBN, and other tungsten bronzes, and $KTa_{1-x}Nb_xO_3$ (KTN) are not available commercially with good optical quality.

Growth of these crystals of the size and optical quality needed for optical signal processing requires an investment of several years, substantial funding, and talented personnel.

A third factor limiting application is low sensitivity. It requires typically $0.5J/cm^2$ to produce a phase conjugate beam with $BaTiO_3$ using self-pumping. Thus for a moderate input intensity of 1 W/cm^2 the response time is of the order of 0.5 sec. At this speed photorefractive materials cannot compete with light valves or electronic computers. Finally, available crystals of $BaTiO_3$ and SBN are somewhat smaller than desirable for the typical optical processing algorithms.

Other photorefractive materials such as $Bi_{12}SiO_{20}$[28] and GaAs[7] are faster or available in larger pieces (GaAs, $LiNbO_3$) but none of these are as nonlinear as $BaTiO_3$ or SBN, and $LiNbO_3$ is slower[29]. Other materials such as semiconductors like CdTe or InP have simply not been the subject of much investigation.

1.2 Outline of the Thesis

In Chapter 2 the band transport theory of the photorefractive mechanism is presented. From an initial, generalized set of equations, three solutions are found that describe the photorefractive effect in three limiting cases. These results will then be used throughout the chapters which follow.

The coupled wave equations for two-wave mixing in photorefractive crystals are derived and solved in Chapter 3.

Effects of energy coupling between the two interacting beams are discussed along with experimental methods for determining the two-beam coupling coefficient and photorefractive response time.

In Chapter 4 the photorefractive materials barium titanate, strontium barium niobate, and barium strontium potassium sodium niobate are described. Their physical, optical, and electrical properties are summarized for use in later chapters. Preparation of these materials is also considered.

The photorefractive properties of these crystals are presented in Chapter 5. Data from two-beam coupling measurements are used to obtain the coupling coefficients, response times, and absorption coefficients under a variety of experimental conditions. The band transport models are then applied to these results in order to further understand their dependence on variables such as temperature and laser intensity.

In Chapter 6 barium titanate, strontium barium niobate, and barium strontium potassium sodium niobate are compared to other ferroelectric and non-ferroelectric photorefractive crystals. This comparison is based upon a number of criteria which serve as useful figures of merit for numerous device applications.

Finally, Chapter 7 deals with the applications of photorefractive crystals. By using the self-focusing properties of barium titanate and strontium barium niobate,

the compensation of nonlinear distortions with phase conjugation is demonstrated. A passive phase conjugator that relies on no external mirrors and uses strontium barium niobate as the nonlinear medium is also described. A thresholding passive phase conjugate mirror is then presented along with several devices that can perform mathematical operations on images.

1.3 References

1. F. S. Chen, J. T. La Macchia, and D. B. Fraser, Appl. Phys. Lett. 13, 223 (1968).

2. P. Gunter, U. Fluckiger, J. P. Huignard, and F. Micheron, Ferroelectrics 13, 297 (1976).

3. J. Feinberg, D. Heiman, A. R. Tanguay, Jr., and R. W. Hellwarth, J. Appl. Phys. 51, 1297 (1980).

4. G. A. Rakuljic, A. Yariv, and R. R. Neargaonkar, Opt. Eng. 25, 1212 (1986).

5. J. P. Huignard and F. Micheron, Appl. Phys. Lett. 29, 591 (1976).

6. S. I. Stepanov and M. P. Petrov, Sov. Tech. Phys. Lett. 10, 572 (1984).

7. M. B. Klein, Opt. Lett, 9, 350 (1984).

8. A. M. Glass, A. M. Johnson, D. H. Olson, W. Simpson, and A. A. Ballman, Appl. Phys. Lett. 44, 948 (1984).

9. G. E. Peterson, A. M. Glass, and T. J. Negran, Appl. Phys. Lett. 19, 130 (1971).

10. M. B. Klein and R. N. Schwartz, J. Opt. Soc. Am. B 3, 293 (1986).

11. F. Laeri, T. Tschudi, and J. Albers, Opt. Commun. 47, 387 (1983).

12. J. O. White, M. Cronin-Golcomb, B. Fischer, and A. Yariv, Appl. Phys. Lett. 40, 450 (1982).

13. J. Feinberg, Opt. Lett. 7, 486 (1982).

14. B. Ya. Zeldovich, V. I. Popovichev, V. V. Ragulskii, and F. S. Faizullov, Sov. Phys. JETP Lett. 15, 109 (1972).

15. S. K. Kwong, G. A. Rakuljic, and A. Yariv, Appl. Phys. Lett 48, 201 (1986).

16. A. E. T. Chiou and P. Yeh, Opt. Lett. 10, 621 (1985).

17. J. Feinberg and G. D. Bacher, Appl. Phys. Lett. 48, 570 (1986).

18. D. Z. Anderson, Opt. Lett. 11, 56 (1986).

19. B. H. Soffer, G. J. Dunning, Y. Owechko, and E. Marom, Opt. Lett. 11, 118 (1986).

20. A. Yariv and S. K. Kwong, Opt. Lett. 11, 186 (1986).

21. M. B. Klein, G. J. Dunning, G. C. Valley, R. C. Lind, and T. R. O'Meara, Opt. Lett. 11, 575 (1986).

22. J. O. White and A. Yariv, Appl. Phys. Lett. 37, 5 (1980).

23. J. P. Huignard and J.P. Herriau, App. Opt. 17, 2671 (1978).

24. M. Cronin-Golomb and A. Yariv, J. Appl. Phys. 57, 4906 (1985).

25. D. Rak, I. Ledoux, and J. P. Huignard, Opt. Commun. 49, 302 (1984).

26. P. S. Brody and R.P. Leavitt, "Dynamic Holographic Method of Imaging Phase Objects," in Technical Digest, Topical Meeting on Holography (Optical Society of America, Washington, D.C., 1986), p. 5.

27. P. S. Brody, "Signal Correlation with Phase-Conjugate Holographic Reconstruction Using a $BaTiO_3$ Crystal," Proc. SPIE 613 (1986).

28. R. A. Mullen and R. W. Hellwarth, J. Appl. Phys. 58, 40 (1985).

29. P. Gunter, Phys. Rep. 93, 199 (1982).

2. THE PHOTOREFRACTIVE EFFECT

The nature of the exact mechanism which is responsible for the photorefractive effect in a given material is still a subject of ongoing debate because of the many possible mechanisms that are potential contributors, and the relative importance of these efects is different in different materials. The basic phenomenon involves the holographic recording of a light interference pattern. As shown in Figure 2.1, charge carriers inside the crystal redistribute themselves because of the spatially varying light intensity, whereupon the electric field associated with the resulting space charge operates through the electrooptic effect to produce a refractive index grating. Many attempts, with varying degrees of sophistication, have been made to formulate theoretical models of the effect[1-26], and there has been considerable success in fitting experimental results to the predictions of these theories.

Most models of the dynamics of the charge migration have involved rate equations taking into consideration the effects of externally applied electric fields and the recursive effects of the space charge electric field on the space charge itself[9,11,13]. This theory also included the photovoltaic effect[4], in which the asymmetry of the crystal caused photoionized charge carriers to be ejected into the conduction band preferentially in a particular direction

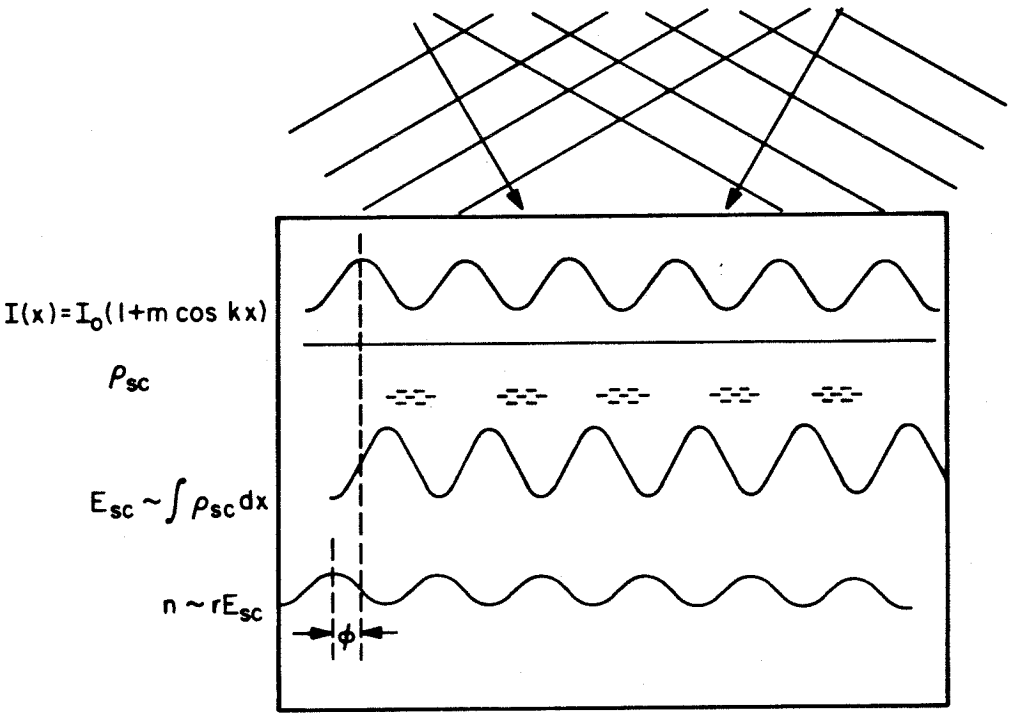

Figure 2.1. The photorefractive mechanism. Two laser beams intersect, forming an interference pattern. Charge is excited where the intensity is large and migrates to regions of low intensity. The electric field associated with the resultant space charge operates through the electrooptic coefficients to produce a refractive index grating.

relative to the optic axis of the crystal thus giving rise to a photocurrent. Feinberg and coworkers[15], however, used a different theory to analyze their results. Their theory, the hopping model, involved a simple physical picture of charge carriers hopping from site to site, with the probability to hop dependent on the local light intensity and electric field. Most recently, a new photorefractive mechanism, the ε model, was proposed by Agranat and Yacoby[18] in which light induced variations of the Curie point of the material are used to modulate the index of refraction.

In the following paragraphs the band transport model will be presented starting from a viewpoint somewhat more general than that used by Kukhtarev[9,11,13]. Three solutions will then be found that describe the photorefractive effect in three limiting cases.

2.1 The Band Transport Theory

In the band transport theory charge carriers are believed to move between trapping centers via a three-step process of photoexcitation, drift or diffusion in the conduction or valence band, and recombination into a neighboring trapping site. Figure 2.2 depicts the process for the case where there are two donor species, two types of trapping centers, and both hole and electron charge transport.

Consider the writing of a refractive index grating by the simultaneous illumination by two mutually coherent beams in a sufficiently thin slice of the photorefractive medium

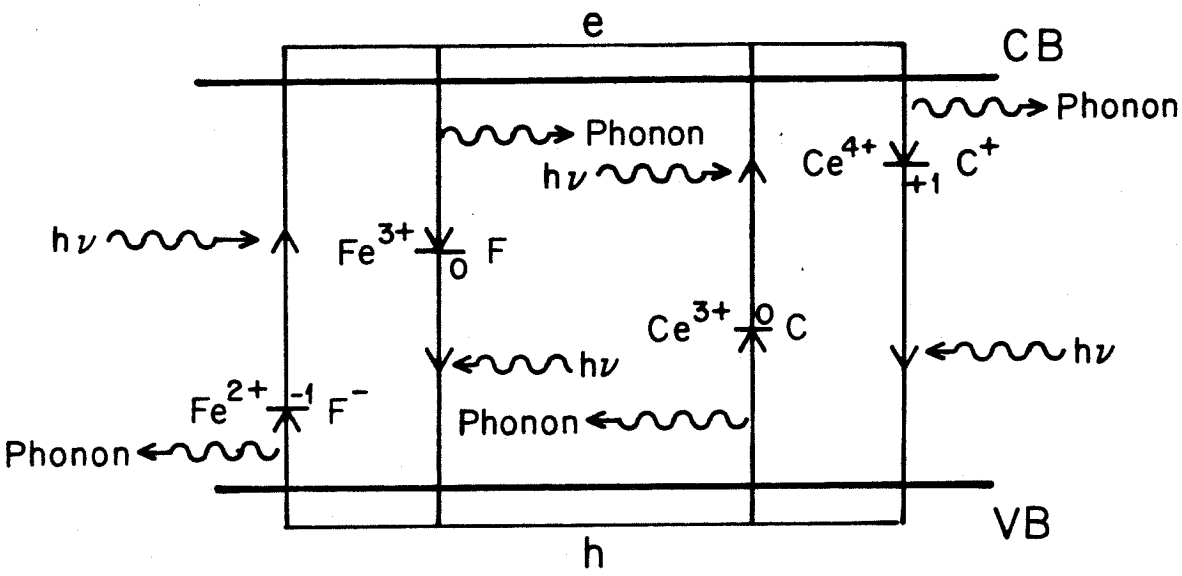

Figure 2.2. Schematic of the band transport model of photorefractivity for the case where there are two donor species, two types of trapping centers, and both hole and electron charge transport. Electrons (holes) are photoexcited into the conduction (valence) band from Fe^{2+} (Fe^{3+}) and Ce^{3+} (Ce^{4+}) donor ions, leaving behind Fe^{3+} (Fe^{2+}) and Ce^{4+} (Ce^{3+}) acceptor ions, respectively. The electrons (holes) then recombine with Ce^{4+} (Ce^{3+}) and Fe^{3+} (Fe^{2+}) traps in regions of low irradiance, thereby completing a cycle of the band transport mechanism.

depicted in Figure 2.2 so that the intensity modulation is constant. Assume that the light intensity interference pattern, which is possibly moving in the x direction, is given by

$$I(x)=I_0+I_1e^{i(kx+\Omega t)}+I_1^*e^{-i(kx+\Omega t)}. \qquad [2.1]$$

The set of equations for determining the spatial distribution of the electric field that is responsible for modulating the refractive index is given in MKS units by (9,11,13,19,20,22)

The rate equations

$$\frac{\partial C}{\partial t} = -\frac{s_e^C I}{h_p \nu} C + \gamma_e^C n C^+, \qquad [2.2]$$

$$\frac{\partial C^+}{\partial t} = -\frac{s_h^C I}{h_p \nu} C^+ + \gamma_h^C h C, \qquad [2.3]$$

$$\frac{\partial F^-}{\partial t} = -\frac{s_e^C I}{h_p \nu} F^- + \gamma_e^F n F, \qquad [2.4]$$

$$\frac{\partial F}{\partial t} = -\frac{s_h^F I}{h_p \nu} F + \gamma_h^F h F^-, \qquad [2.5]$$

the continuity equation

$$\frac{\partial}{\partial t}(n-h+F^--C^+) = \frac{1}{e}\frac{\partial J}{\partial x}, \qquad [2.6]$$

the current equation

$$J = e(\mu_e n+\mu_h h)E+k_B T(\mu_e\frac{\partial n}{\partial x} - \mu_h\frac{\partial h}{\partial x}) \qquad [2.7]$$

Poisson's equation

$$\frac{\partial E}{\partial X} = \frac{-e}{\varepsilon}(n-h+F^{-}-C^{+}+N_A^C-N_A^F), \qquad [2.8]$$

and the number densities

$$F^{-} + F = N_{Fe} \qquad [2.9]$$

$$C + C^{+} = N_{Ce} \qquad [2.10]$$

where

- C is the number density of Ce that act as donors for electron transport or acceptors for hole transport,
- C^{+} is the number density of Ce that act as acceptors for electron transport or donors for hole transport,
- e is the charge on the electron,
- E is the total electric field,
- ε is the static dielectric constant,
- F is the number density of Fe that act as acceptors for electron transport or donors for hole transport,
- F^{-} is the number density of Fe that act as donors for electron transport or acceptors for hole transport,
- γ_e^C is the two-body recombination rate coefficient for elections at sites C^{+},
- γ_h^C is the two-body recombination rate coefficient for holes at sites C,
- γ_e^F is the two-body recombination rate coefficient for electrons at sites F,
- γ_h^F is the two-body recombination rate coefficient for holes at sites F-,

h is the hole number density,

h_p is Plank's constant,

J is the current density,

k_B is Boltzmann's constant,

μ_e is the electron mobility,

μ_h is the hole mobility,

n is the electron number density,

N_{Ce} is the total number density of species Ce,

N_{Fe} is the total number density of species Fe,

ν is the frequency of the optical wave,

N_A^C is the number density of negatively charged, nonphotoactive ions that compensate for the charge of C^+ in the dark,

N_A^F is the number density of positively charged, nonphotoactive ions that compensate for the charge of F^- in the dark,

s_e^C is the photoionization cross section of C,

s_h^C is the photoionization cross section of C^+,

s_e^F is the photoionization cross section of F^-,

s_h^C is the photoionization cross section of C^+, and

T is the temperature.

When the modulation index of the light interference pattern is significantly less than one, E, C^+, F^-, n, and h can be

approximated by

$$E=E_0 + E_1(t)e^{ikx}+E_1^*(t)e^{-ikx} \quad [2.11]$$

$$C^+=C_0^+ + C_1^+(t)e^{ikx}+(C_1^+)^*(t)e^{-ikx} \quad [2.12]$$

$$F^-=F_0^- + F_1^-(t)e^{ikx}+(F_1^-)^*(t)e^{-ikx} \quad [2.13]$$

$$n=n_0+n_1(t)e^{ikx}+n_1^*(t)e^{-ikx} \quad [2.14]$$

$$h=h_0+h_1(t)e^{ikx}+h_1^*(t)e^{-ikx} \quad [2.15]$$

where E_1, C_1^+, F_1^-, n_1, and h_1 are the first order harmonic amplitudes. Higher order terms become increasingly important as the modulation index approaches unity [27,28].

In the sections to follow three solutions to the above equations are found. The first one describes the case of only one photorefractive species and one carrier, while the second solution allows for two charge carriers. Finally, the third case considers the photorefractive mechanism when there are two photoactive species, but one type of charge carrier.

2.2 Solutions to the Band Transport Equations

2.2.1 The one species, one carrier solution

The equations that describe the situation in which there is only one photorefractive species, assumed to be Ce, and only one type of charge carrier, the electron, are still Eqs. [2.1]-[2.15], but with the following terms set to zero:

$$N_{Fe}=F=F^-=N_A^F=S_e^F=S_h^F=\gamma_e^F=\gamma_h^F=h=\mu_h=S_h^C=\mu_h^C=0. \quad [2.16]$$

The subsequent equations have been solved [29] for the electric field E under the assumption that $C>>C^+$. Extending this solution to include situations in which this condition may not necessarily hold results in the following expression for the induced electric field.

$$E_0 = \text{applied field normal to grating planes} \qquad [2.17]$$

and

$$E_1 = -iE_q \frac{I_1}{I_0} \frac{(E_0+iE_d)(e^{i\Omega t}-e^{-t/\tau})}{[E_0-\Omega t_0(E_d+E_\mu)]+i(E_d+E_q+\Omega t_0 E_0)}, \qquad [2.18]$$

where the characteristic fields are defined by

$$E_q = \frac{eN_A^C}{\varepsilon k}\,[1+N_A^C/(N_{Ce}-N_A^C)]^{-1}, \qquad [2.19]$$

$$E_d = \frac{k_B T k}{e}, \text{ and} \qquad [2.20]$$

$$E_\mu = \frac{\gamma_e^C N_A^C}{\mu_e k}, \qquad [2.21]$$

and where the response time is given by

$$\tau = t_0 \frac{E_0+i(E_d+E_\mu)}{E_0+i(E_d+E_q)}, \qquad [2.22]$$

and where

$$t_0 = \frac{h_p \nu N_A^C}{s_e^C I_0 (N_{Ce}-N_A^C)}. \qquad [2.23]$$

The refractive index change can now be obtained by considering the electrooptic effect in the material.

2.2.2 The one species, two carrier solution

The second case to be considered is similar to the one just presented. Again, only one photorefractive species is assumed, this time Fe, but a second type of charge carrier is now allowed; namely, the hole. Equations [2.1]-[2.15] are still valid with the following terms set to zero:

$$N_{Ce} = C^{+} = C = N_A^C = S_e^C = S_h^C = \gamma_e^C = \gamma_h^C = 0. \qquad [2.24]$$

A solution to the resulting set of equations has been found for the electric field E in the steady-state [22], assuming a stationary intensity interference pattern (Ω=0) and no externally applied electric field. It is

$$E_0 = 0 \qquad [2.25]$$

and

$$E_1 = iE_q \frac{I_1}{I_0} \frac{E_d \quad (\sigma_h - \sigma_e)}{(E_d + E_q) \quad (\sigma_h + \sigma_e)}, \qquad [2.26]$$

where the characteristic fields are defined by

$$E_q = \frac{e(N_{Fe} - N_A^F)}{\varepsilon k} \left[1 + (N_{Fe} - N_A^F)/N_A^F\right]^{-1} \qquad [2.27]$$

and

$$E_d = \frac{k_B T k}{e}, \qquad [2.28]$$

and where the mean electron and hole conductivities are given by

$$\sigma_e = \frac{e\mu_e S_e^F I_0 N_A^F}{\gamma_e^F (N_{Fe} - N_A^F) h_p \nu} \qquad [2.29]$$

and

$$\sigma_h = \frac{e\mu_h S_h^F I_0 (N_{Fe}-N_A^F)}{\gamma_h^F N_A^F h_p \nu}. \qquad [2.30]$$

The resulting refractive index change can be calculated by considering the electrooptic effect in the material.

2.2.3 The two species, one carrier solution

This final case considers the situation in which there are two photorefractive species, Ce and Fe, but only one type of charge carrier, assumed to be the electron. Equations [2.1]-[2.15] with the following terms set to zero describe photorefractive mechanism in this example:

$$S_h^F=S_h^C=\gamma_h^F=\gamma_h^C=h=\mu_p=0. \qquad [2.31]$$

These equations have been solved [19,30] for the electric field E assuming a stationary intensity interference pattern (Ω=0). The solution is

E_0=applied field normal to grating planes [2.32]

and

$$E_1=\frac{-ie}{\varepsilon k}I_1\left(\frac{i}{\tau_{diff}}-\frac{i}{\tau_E}\right)\left(\frac{\alpha_F}{\tau_{Ic}}+\frac{\alpha_C}{\tau_{IF}}\right)T_0^3(1+A_+e^{-t/\tau+}+A-e^{-t/\tau-}), \qquad [2.32]$$

where

$$A\pm = \pm\frac{1}{2}\left(\frac{T_1^{-2}}{\sqrt{T_1^{-4}-4T_2^{-1}T_0^{-3}}}\mp 1\right), \qquad [2.33]$$

where the response times are given by

$$\tau^{\pm} = \frac{2T_2^{-1}}{T_1^{-2} \pm \sqrt{T_1^{-4} - 4T_2^{-1}T_0^{-3}}}, \qquad [2.34]$$

where the absorption coefficients are defined by

$$\alpha_F = \frac{S_e^F N_A^F}{h_p \nu} \qquad [2.35]$$

and

$$\alpha_C = \frac{S_e^C (N_{Ce} - N_A^C)}{h_p \nu}, \qquad [2.36]$$

and where the characteristic times are defined by

$$T_0 = \left[\frac{1}{\tau_{di}}\left(\frac{1}{\tau_{IC}\tau_{IF}} + \frac{1}{\tau_{IC}\tau_F} + \frac{1}{\tau_{IF}\tau_C}\right) + \frac{1}{\tau_{IF}\tau_{IC}}\left(\frac{1}{\tau_{diff}} - \frac{i}{\tau_E}\right)\right]^{-\frac{1}{3}}, \qquad [2.37]$$

$$T_1 = \left[\left(\frac{1}{\tau_{diff}} - \frac{i}{\tau_E}\right)\left(\frac{1}{\tau_{IC}} + \frac{1}{\tau_{IF}}\right) + \frac{1}{\tau_{IC}\tau_{IF}} + \frac{1}{\tau_{IC}\tau_F} + \frac{1}{\tau_C\tau_{IF}} + \frac{1}{\tau_{di}}\left(\frac{1}{\tau_{IF}} + \frac{1}{\tau_F} + \frac{1}{\tau_{IC}} + \frac{1}{\tau_C}\right)\right]^{-\frac{1}{2}}, \qquad [2.38]$$

and

$$T_2 = \left[\frac{1}{\tau_{IF}} + \frac{1}{\tau_F} + \frac{1}{\tau_{IC}} + \frac{1}{\tau_C} + \frac{1}{\tau_{di}} + \frac{1}{\tau_{diff}} - \frac{i}{\tau_E}\right]^{-1} \qquad [2.39]$$

with

$$\tau_{di} = \frac{\varepsilon}{e\mu_e n_0}, \qquad [2.40]$$

$$\tau_{diff} = \frac{e}{k_B T \mu_e k^2}, \qquad [2.41]$$

$$\tau_E = (\mu_e k E_0)^{-1}, \qquad [2.42]$$

$$\tau_{IC} = (S_e^C I_0 + \gamma_e^C n_0)^{-1}, \qquad [2.43]$$

$$\tau_{IF} = (S_e^F I_0 + \gamma_e^F n_0)^{-1}, \qquad [2.44]$$

$$\tau_C = (\gamma_e^C N_A^C)^{-1}, \text{ and} \qquad [2.45]$$

$$\tau_F = [\gamma_e^C (N_{Fe} - N_A^F)]^{-1}$$

where the zeroth-order electron number density is given by

$$n_0 = \frac{[S_e^C (N_{Ce} - N_A^C) + S_e^F N_A^F] I_0}{[\gamma_e^C N_A^C + \gamma_e^F (N_{Fe} - N_A^F)] h_p \nu} . \qquad [2.46]$$

As before, the refractive index change can now be calculated by considering the electrooptic effect.

2.3 References

1. J. J. Amodei, RCA Rev. 32, 185 (1971).

2. Y. Ninomaya, J. Opt. Soc. Am. 63, 1124 (1973).

3. L. Young, W. K. Y. Wong, M. L. W. Thewalt, and W. D. Cornish, Appl. Phys. Lett. 24, 264 (1974).

4. A. M. Glass, D. Von der Linde, and T. J. Negran, Appl. Phys. Lett. 25, 233 (1974).

5. D. W. Vahey, J. Appl. Phys. 46, 2510 (1975).

6. D. M. Kim. R. R. Shah, T. A. Rabson, and F. K. Tittel, Appl. Phys. Lett. 28, 338 (1975).

7. S. F. Su and T. K. Gaylord, J. Appl. Phys. 47, 190 (1976).

8. R. Magnusson and T. K. Gaylord, J. Appl. Phys. 47, 190 (1976).

9. N. V. Kukhtarev, Sov. Tech. Phys. Lett. 2, 438 (1976).

10. M. G. Moraham and L. Young, J. Appl. Phys. 48, 3230 (1977).

11. N. K. Kukhtarev, V. B. Markov, and S. G. Odulov, Opt. Commun. 23, 338 (1977).

12. B. I. Sturman, Sov. Phys. Tech. Phys. 23, 589 (1978).

13. N. K. Kukhtarev, V. B. Markov, S. G. Odulov, M. S. Soskin, and V. L. Vinetskii, Ferroelectrics 22, 949 (1979).

14. M. G. Moharam, T. K. Gaylord, R. Magnusson, and L. Young, J. Appl. Phys. 50, 5642 (1979).

15. J. Feinberg, D. Heiman, A. R. Tanquay, Jr., and R. W. Hellwarth, J. Appl. Phys. 51, 1297 (1980).

16. J. Feinberg, Opt. Lett. 5, 330 (1980).

17. S. I. Stepanov, V. V. Kulikov, and M. P. Petrov, Opt. Commun. 44, 19 (1982).

18. A. Agranat and Y. Yacoby, Phys. Rev. B 27, 5712 (1983).

19. G. C. Valley, Appl. Opt. 22, 3160 (1983).

20. G. C. Valley and M. B. Klein, Opt. Eng. 22, 704 (1983).

21. J. M. Heaton and L. Solymar, Opt. Acta 32, 397 (1985).

22. M. B. Klein and G. C. Valley, J. Appl. Phys. 57, 4901 (1985).

23. G. A. Rakuljic, A. Yariv, and R. R. Neurgaonkar, Proc. SPIE 613, 110 (1986).

24. S. Ducharme and J. Feinberg, J. Opt. Soc. Am. B 3, 283 (1986).

25. M. B. Klein and R. N. Schwartz, J. Opt. Soc. Am. B 3, 293 (1986).

26. G. A. Rakuljic, A. Yariv, and R. R. Neurgaonkar, Opt. Eng. 25, 1212 (1986).

27. M. P. Petrov, S. V. Miridonov, S. I. Stepanov, and V. V. Kulikov, Opt. Commun. 31, 301 (1979).

28. E. Ochoa, F. Vachss, and L. Hesselink, J. Opt. Soc. Am A 3, 181 (1986).

29. M. Cronin-Golomb, Ph.D. Dissertation (California Institute of Technology, Pasadena, California 1983, unpublished).

30. J. O. White, Ph.D. Dissertation (California Institute of Technology, Pasadena, California 1984, unpublished).

3. TWO-WAVE MIXING IN PHOTOREFRACTIVE CRYSTALS

In the previous chapter the grating formation in photorefractive crystals was explained in terms of nonlinear differential equations which describe the coupling between the light and the mobile charges within the crystal. A spatially varying intensity pattern set up by two interfering plane waves was found to cause a redistribution of charge which then modulates the index of refraction through the electrooptic effect. The plane wave components which set up are subsequently coupled to each other by the self-induced diffraction. In this chapter, the problem of propagation of light within these crystals is investigated by means of a set of nonlinear differential equations which describe the coupling.

3.1 Coupled Wave Theory

Consider the two-wave mixing configuration shown in Figure 3.1 in which beams 1 and 2 are plane waves of the same polarization, but of different frequencies. Their optical electric fields can be written as

$$\vec{E}_1(\omega_1)=\vec{A}_1(\vec{r})e^{i(\vec{k}_1\cdot\vec{r}-\omega_1 t)}+c.c. \qquad [3.1]$$

and

$$\vec{E}_2(\omega_2)=\vec{A}_2(\vec{r})e^{i(\vec{k}_2\cdot\vec{r}-\omega_2 t)}+c.c. \qquad [3.2]$$

These two coherent beams form an intensity interference pattern in the crystal which gives rise to a refractive index

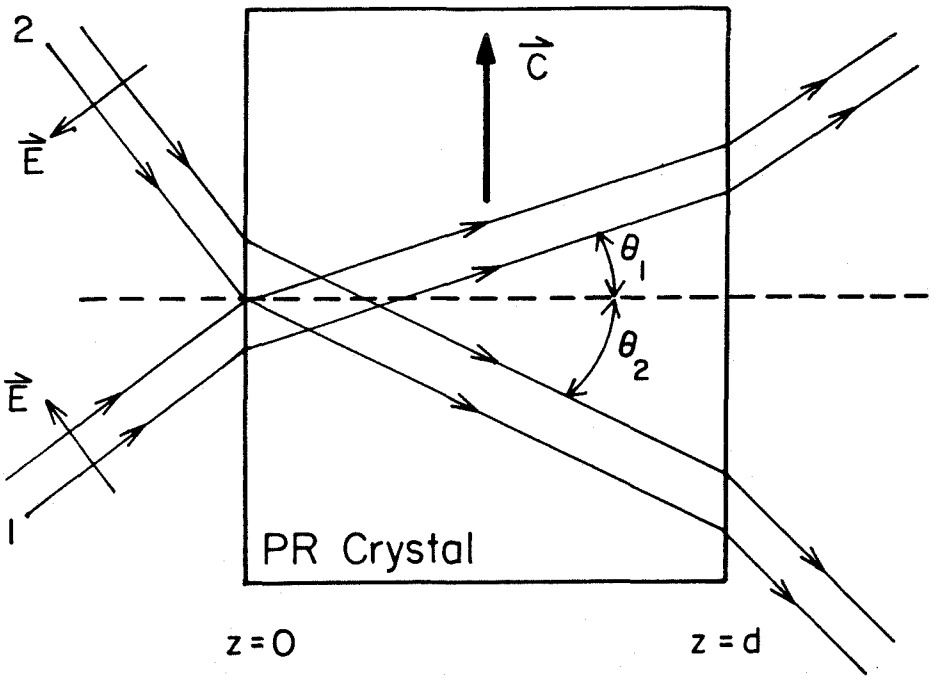

Figure 3.1. Two-wave mixing in photorefractive crystals.

variation through the photorefractive effect. From the photorefractive theory developed in Chapter 2, this index grating is given by

$$n = n_0 + \frac{1}{2} r_{eff} n_0^3 E_1 e^{i(\vec{k}_1 - \vec{k}_2)\cdot\vec{r}} + c.c. \qquad [3.3]$$

where n_0 is the background refractive index of the crystal and r_{eff} is the effective electrooptic coefficient.

Substituting this index variation into the scalar wave equation

$$\nabla^2 E + k^2 E = 0, \qquad [3.4]$$

and using the slowly varying field approximation [1]

$$\frac{d^2 A_j}{dz^2} << k \frac{dA_j}{dz}, \qquad [3.5]$$

the coupled wave equations

$$\cos\theta_1 \frac{dA_1}{dz} = -\gamma \frac{A_1 A_2^* A_2}{A_1 A_1^* + A_2 A_2^*} - \frac{\alpha}{2} A_1 \qquad [3.6a]$$

$$\cos\theta_2 \frac{dA_2}{dz} = \gamma^* \frac{A_1^* A_2 A_1}{A_1 A_1^* + A_2 A_2^*} - \frac{\alpha}{2} A_2 \qquad [3.6b]$$

are obtained where

$$\gamma = \frac{i\omega}{4c} r_{eff} n_0^3 E_1 \frac{A_1 A_1^* + A_2 A_2^*}{A_1 A_2^*}, \qquad [3.7]$$

θ_1 and θ_2 are the angles between the beams and the z-axis, and α is the intensity absorption coefficient. In most situations of interest, $(\omega_2 - \omega_1)/\omega_1 << 1$; otherwise, the response of the crystal would not be fast enough to follow

the moving light interference pattern. Therefore, ω_1 and ω_2 can be replaced by $\omega \simeq \omega_1 \simeq \omega_2$, except in the term E_1 in Eqs. [3.3] and [3.7].

The first term of the right side of Eq. [3.6] represents the contribution from self-diffraction, while the second one represents the linear absorption in the crystal. Equation [3.6] can be rewritten in terms of the intensity and phase of each beam:

$$\cos\theta_1 \frac{dI_1}{dz} = -\Gamma \frac{I_1 I_2}{I_0} - \alpha I_1 \qquad [3.8a]$$

$$\cos\theta_2 \frac{dI_2}{dz} = -\Gamma \frac{I_1 I_2}{I_0} - \alpha I_2 \qquad [3.8b]$$

$$\cos\theta_1 \frac{d\psi_1}{dz} = -\Gamma' \frac{I_2}{I_0} \qquad [3.8c]$$

$$\cos\theta_2 \frac{d\psi_2}{dz} = -\Gamma' \frac{I_2}{I_0}, \qquad [3.8d]$$

where $\Gamma = 2\mathrm{Re}\{\gamma\}$, $\Gamma' = \mathrm{Im}\{\gamma\}$,

$I_0 = I_1 + I_2$ is the total intensity,

$I_j = A_j^2$, and $A_j = A_j e^{i\psi_j}$, $j=1,2$. [3.9]

Note that the intensity coupling is due to the real part of the coupling constant γ, and the phase delay is due to the imaginary part of γ. The phase delay is independent of α and is always equal to zero when the phase of E_1 is $\pm\pi/2$. At this point the induced index grating is 90° out of phase from the interference pattern, which results in maximum intensity coupling. This condition is often satisfied in photo

refractive crystals to which no external electric fields have been applied.

3.2 Solutions to the Coupled Wave Equations

Equation [3.8] can be solved [2-4] in the symmetric case where $\theta_1=\theta_2=\theta$ given the initial values $I_1(0)$, $I_2(0)$, $\psi_1(0)$, and $\psi_2(0)$. The solution is

$$I_1(\xi) = \frac{[I_1(0)+I_2(0)]e^{-\alpha\xi}}{1 + \frac{I_2(0)}{I_2(0)}e^{-\Gamma\xi}} \qquad [3.10a]$$

$$I_2(\xi) = \frac{[I_1(0)+I_2(0)]e^{-\alpha\xi}}{1 + \frac{I_1(0)}{I_2(0)}e^{-\Gamma\xi}} \qquad [3.10b]$$

$$\psi_1(\xi) = \psi_1(0)-\Gamma'\xi+\frac{\Gamma'}{\Gamma}\ell n\left[\frac{1+\frac{I_1(0)}{I_2(0)}}{1+\frac{I_1(0)}{I_2(0)}e^{-\Gamma\xi}}\right] \qquad [3.10c]$$

$$\psi_2(\xi) = \psi_2(0)-\Gamma'\xi-\frac{\Gamma'}{\Gamma}\ell n\left[\frac{1+\frac{I_2(0)}{I_1(0)}}{1+\frac{I_2(0)}{I_1(0)}e^{\Gamma\xi}}\right] \qquad [3.10d]$$

where $\xi=z/\cos\theta$ and $0\leq\xi\leq\ell=d/\cos\theta$.

Equations [3.10a] and [3.10b] describe the coherent optical gain for beam 2 at the expense of beam 1 when Γ is positive. A coherent optical amplifier can be built based on this principle. Equations [3.10c] and [3.10d] describe the phase delays of the beams due to the nonlinear interaction.

Photorefractive crystals can thus be viewed as dynamic holographic media in which refractive index holograms can be

repeatedly and continuously rewritten. In general, a phase shift exists between the hologram and the light interference pattern creating the hologram which can result in energy coupling between the interacting beams. These two phenomena are the unique properties of photorefractive crystals that distinguish them from other holographic media such as photographic emulsions, dichromated gelatin [5], and photopolymer materials [6].

3.3 Experimental Methods of Two-Beam Coupling

The two-wave mixing experiment of Figure 3.1 can be used experimentally to determine the two-beam coupling coefficient Γ, which from Eq. [3.7] is a fundamental quantity of the photorefractive crystal. Equations [3.10a] and [3.10b] can be solved for Γ to give

$$\Gamma = \frac{1}{\ell} \ln \left[\frac{I_1^i(0) I_2^i(\ell)}{I_1^i(\ell) I_2^i(0)} \right] , \qquad [3.11]$$

where the superscript i denotes intensities inside the crystal.

In practice, however, it is the intensities outside the crystal are measured. They are related to the intensities

inside the crystal by [7]

$$I_1^i(0) = TI_1^0(0), \qquad [3.12a]$$

$$I_2^i(0) = TI_2^0(0), \qquad [3.12b]$$

$$I_1^0(\ell) = TI_1^i(\ell), \text{ and} \qquad [3.12c]$$

$$I_2^0(\ell) = TI_2^i(\ell), \qquad [3.12d]$$

where the superscript ^{0} denotes intensities outside the crystal. Incorporating these into Eq. [3.11] results in

$$\Gamma = \frac{1}{\ell} \ln \left[\frac{I_1^0(0) I_2^0(\ell)}{I_1^0(\ell) I_2^0(0)} \right]. \qquad [3.13]$$

Therefore, by measurement of the four intensities $I_1(0)$, $I_2(0)$, $I_1(\ell)$, and $I_2(\ell)$ outside the crystal, the two-beam coupling coefficient Γ can be obtained from Eq. [3.13].

The transient behavior of the two-beam coupling may be approximated [8,9] by

$$I_j(\ell;t) = (1-e^{-t/\tau}) I_j(\ell;t\to\infty) + e^{-t/\tau} I_j(\ell;t=0), \quad j=1,2, \qquad [3.14]$$

where τ is the photorefractive response time of the crystal. From the results of Chapter 2, τ is also a fundamental photorefractive quantity of the material. Therefore, by measurement of $I_1(\ell)$ and $I_2(\ell)$ as a function of time, the response time τ can be obtained by fitting the data to Eq. [3.14].

3.4 References

1. A. Yariv, Quantum Electronics, (Wiley, New York, 1975).

2. D. W. Vahey, J. Appl. Phys. 46, 3510 (1975).

3. M. G. Moraham and L Young, J. Appl. Phys. 48, 3230 (1977).

4. N. V. Kukhtarev, V. B. Markov, S. G. Odulov, M. S. Soskin, and V. L. Vinetskii, Ferroelectrics 22, 949 (1979).

5. T. Shankoff, Appl. Opt. 7, 2101 (1968).

6. O. H. Close, A. D. Jacobson, J. D. Margerum, R. G. Brault, and F. J. McClung, Appl. Phys. Lett. 14, 159 (1969).

7. See, for example, M. Born and E. Wolf, Principles of Optics, (Macmillan, New York, 1964).

8. J. M. Heaton and L. Solymar, Opt. Acta 32, 397 (1985).

9. G. A. Rakuljic, A. Yariv, and R. R. Neurgaonkar, Opt. Eng. 25, 1212 (1986).

4. PHOTOREFRACTIVE CRYSTALS

Photorefractive effects have been observed in many electrooptic crystals such as $Bi_{12}SiO_{20}$, $Bi_{12}GeO_{20}$, $LiNbO_3$, $LiTaO_3$, $(PbLa)(TiZr)O_3$, KH_2PO_4, CdS, $Bi_4Ti_3O_{12}$, $K(TaNb)O_3$, $KNbO_3$, $BaTiO_3$, $Ba_2NaNb_5O_{15}$, and $Sr_xBa_{1-x}Nb_2O_6$(SBN)[1-12], and may be considered a general property of electrooptic materials. Depending on the bandgap and the transport properties of the given crystal, the refractive index changes may be induced not only by visible light, but also by ultraviolet or infrared radiation.

In this chapter and in the ones to follow, attention will be focused on two classes of photorefractive crystals; namely, the perovskite $BaTiO_3$ and the tungsten bronze ferroelectrics.

4.1 Barium Titanate

Barium titanate ($BaTiO_3$) was the first ferroelectric perovskite to be discovered. The perfect perovskite structure is an extremely simple one with a general formula ABO_3, where A is a monovalent or divalent metal and B is a tetravalent or pentavalent one. As shown in Fig. 4.1, it is cubic, with the A atoms at the cube corners, B atoms at the body centers, and the oxygens at the face centers.

$BaTiO_3$ has the prototypical cubic perovskite structure, point group m3m, above 120°C. Below 120°C it transforms successively to three ferroelectric phases; first to 4mm

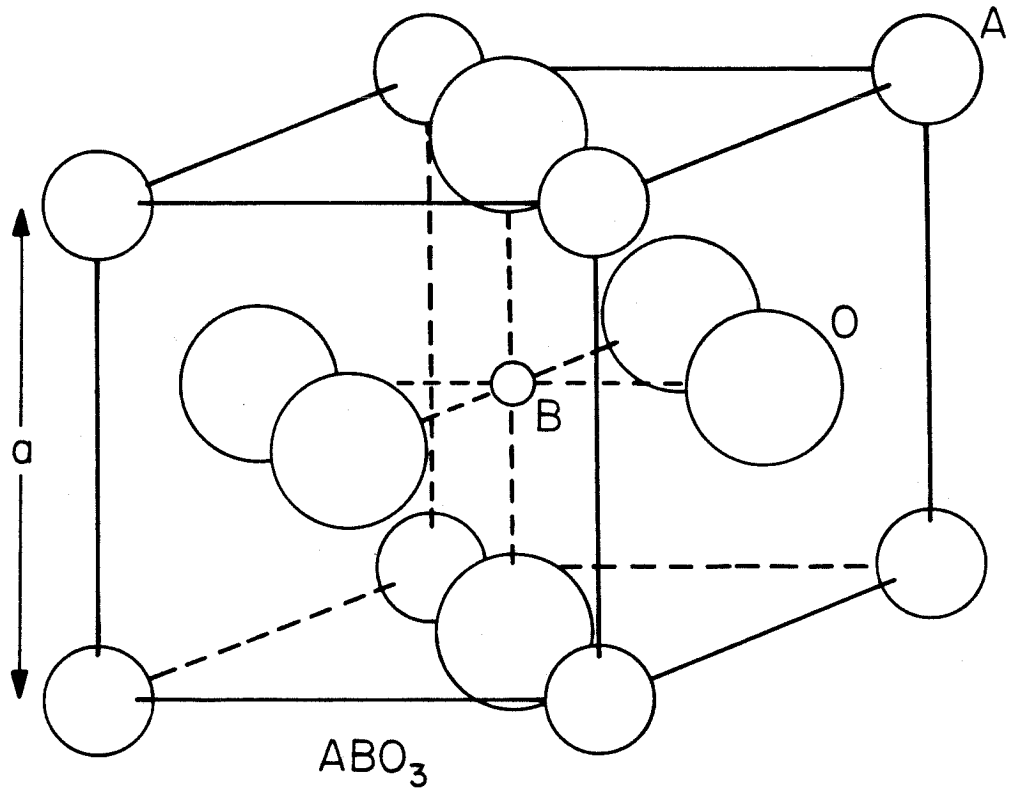

Figure 4.1. The cubic ABO_3 perovskite structure. (After Ref. 21)

tetragonal, then to mm orthorhombic at about 5°C, and finally to a 3m triagonal phase below -90°C. The polar axis in the three ferroelectric phases is [001], [011], and [111] respectively. All three transitions are of first order, and the temperature dependence of the dielectric constant shows discontinuities at the transitions and peak values as high as 10^4. Above T_c=120°C the dielectric constant follows a Curie-Weiss law[13].

At room temperature, $BaTiO_3$ has a tetragonal structure with very large electrooptic coefficients. The origin of these anomalously large constants is the phase change at 5°C. This phase change destabilizes the polar vector in the plane perpendicular to the fourfold axis of the tetragonal form, giving exceedingly high values for ε_{11} and thus the large electrooptic coefficients r_{51} and r_{42}. Furthermore, these values are strongly temperature dependent. Extreme care must be exercised when $BaTiO_3$ is cooled below room temperature since this phase transition can lead to catastrophic damage of the crystal; i.e., cracking. Additionally, twinning can occur and severely limit the application of large electric fields to $BaTiO_3$. These ferroelectric twins, unfortunately, are difficult to remove by poling.

4.2 Tungsten Bronze Ferroelectrics

Ferroelectric tungsten bronze oxides have been studied for their electrooptic and pyroelectric properties[14-16]. The bronze compositions can be represented by the general

formulas as $(A_1)_4(A_2)_2B_{10}O_{30}$, in which A_1, A_2, C, and B are 15-, 12-, 9-, and 6- fold coordinated sites in the structure. The basic octahedral framework of the tungsten bronze structure is shown in Fig. 4.2. A wide range of solid solutions can be obtained by the substitution of different A_1, A_2, and B cations[17-19], and a number of different types of ferroelectric phases have been identified. These phases can be divided into two groups; those with tetragonal symmetry (4mm) and those with orthorhombic symmetry (mm2).

Table 4.1 lists a number of tetragonal and orthorhombic tungsten bronze crystals along with values of their electrooptic coefficients. In general, the r_{42} coefficient is large for the orthorhombic bronzes, while either r_{33} or r_{51} can be large for the tetragonal bronze crystals, depending on the size of the unit cell. In the smaller unit cell crystals, such as SBN, the dominant electrooptic coefficient is r_{33}, whereas in the larger unit cell bronzes, such as BSKNN, r_{51} is the largest coefficient.

4.3 The Photorefractive Crystals That Were Studied

Eight photorefractive crystals were studied in this work. One was barium titanate, while the remaining seven were tungsten bronze ferroelectrics. Six of these were strontium barium niobate and barium strontium potassium sodium niobate was the seventh. All eight were, typically, single crystals in the shape of cubes, 0.5 cm on a side. Usually all six faces were polished while electrodes were

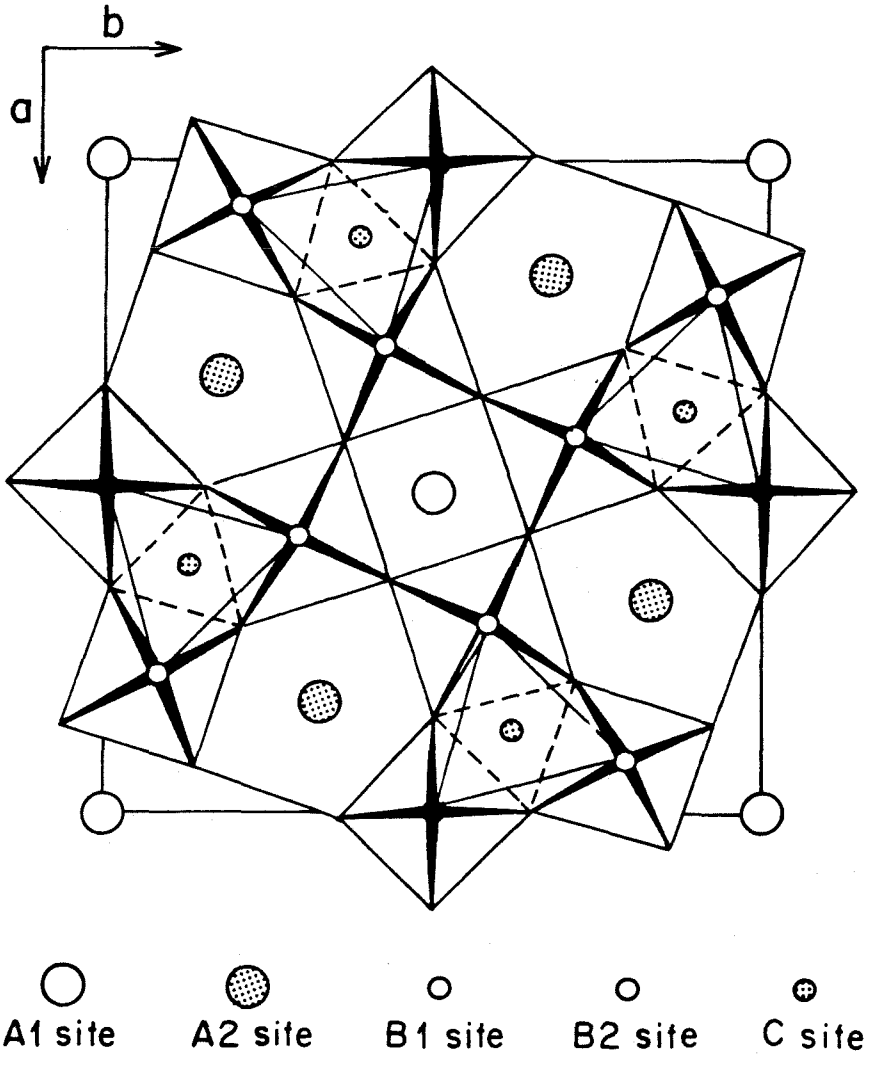

Figure 4.2. The basic octahedral framework of the tungsten bronze structure looking down the tetragonal c-axis. (After Ref. 23)

Table 4.1. List of important tungsten bronze crystals. (After Ref. 24)

Composition	T_c (°C)	Dielectric Coefficient ϵ_{33}	Dielectric Coefficient ϵ_{11}	Electrooptic Coefficient x 10^{-12} m/V	Unit Cell aÅ	Unit Cell bÅ	Unit Cell cÅ
Tetragonal crystals							
SBN:75	56	3400	-	1400	12.440	-	3.924
SBN:60	75	880	470	420	12.467	-	3.937
SBN:50	128	450	300	180	12.475	-	3.952
SKN	150	1000	800	270	12.470	-	3.939
BSKNN	207	200	350	380	12.560	-	3.973
$K_3Li_2Nb_5O_{15}$	405	115	306	80	12.580	-	4.015
PBN:60	350	310	560	1000	12.576	-	3.978
$Ba_6Ti_2Nb_8O_{30}$	245	209	193	420	12.589	-	4.020
Orthorhombic crystals							
$Pb_2KNb_5O_{15}$	460	129	1550	r_{42} = 100	17.780	17.961	7.784
$Ba_2NaNb_5O_{15}$	560	57	242	r_{42} = 92	17.590	17.613	7.982
$Sr_2NaNb_5O_{15}$	270	1500	-	r_{42} = 400	17.450	17.493	7.784
$K_2BiNb_5O_{15}$	405	500	400	-	17.851	17.852	7.804
$K_3Li_2Nb_{2.7}Ta_{2.3}O_{15}$	150	375	300	-	-	-	-

added to the C-faces of some of the crystals. Before conducting any experiments, the crystals were electrically poled by first being heated to above their Curie points and then being cooled to room temperature with an applied dc electric field of 5 to 8 kV/cm along their c-axis. When poling $BaTiO_3$, however, the temperature of the crystal was not allowed to rise above $110^{o}C$ and an electric field of only 1KV/cm was used; otherwise, cracking of the crystal occurred.

The $BaTiO_3$ single crystal was obtained from Sanders Associates[20]. Its absorption spectrum was taken and is shown in Fig. 4.3. Although the spectrum is rather featureless, slight perturbations near 550nm and 590nm indicate the presence of deep level impurities. Also, due presumably to the presence of a large Urbach tail[21], a distinct band edge cannot be identified. Finally, while optical absorption is rather large throughout the visible, the $BaTiO_3$ crystal becomes increasingly transparent in the near-infrared.

The strontium barium niobate (SBN) crystals were grown at Rockwell International Corporation[22] by the Czochralski technique. Undoped, the crystal is transparent and can be grown with a variety of ferroelectric and electrooptic properties, depending on the specific cation ratios introduced into the structure. In SBN the unit cell contains 10 NbO_6 octahedra, with only five alkaline earth cations to fill 10 interstitial sites[23]. The structure is thus incompletely filled, which permits the addition of a wide

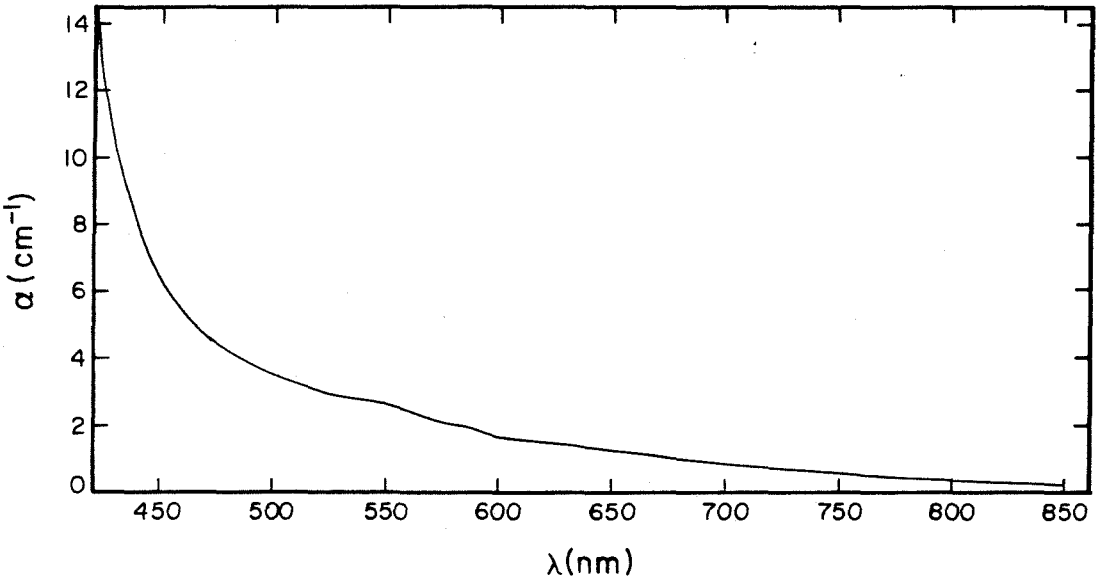

Figure 4.3. Absorption spectrum of $BaTiO_3$.

range of dopants into the host crystal. The general formula for SBN is $Sr_xBa_{1-x}Nb_2O_6$, so SBN:60 represents $Sr_{0.6}Ba_{0.4}Nb_2O_6$.

The six SBN crystals that were studied include both undoped and doped samples. They were (1): an undoped SBN:60; (2): a heavily cerium-doped SBN:60; (3): a heavily iron-doped SBN:60; (4): a lightly cerium-doped SBN:60; (5): a lightly cerium-doped SBN:75; and (6): a doubly calcium- and cerium-doped SBN:60. The absorption spectra of these six crystals are shown in Figs. 4.4 through 4.9.

Figures 4.5 and 4.6 show the effects of cerium and iron impurities on the absorption spectrum of undoped SBN:60, which is given in Fig. 4.4. Several interesting observations can be made. First, the band edge shifts from 400nm in undoped SBN:60 to 430nm in Ce-doped SBN:60. Second, deep level impurities in the undoped SBN:60 sample are evidenced by perturbations in its spectrum near 550nm. Finally, the effects of Ce and Fe in SBN:60 are seen to be significantly different. While the spectrum of Ce-doped SBN:60 is rather featureless, with a broad deep level centered at 480nm, the spectrum of Fe-doped SBN:60 displays a structured but broad absorption extending from 500nm to 700nm, with characteristic peaks at 550nm and 590nm.

The absorption spectrum of the doubly-doped SBN:60 crystal shown in Fig. 4.9 is markedly different from that of the other cerium-doped samples. While absorption in these crystals decreases monotonically with increasing wavelength

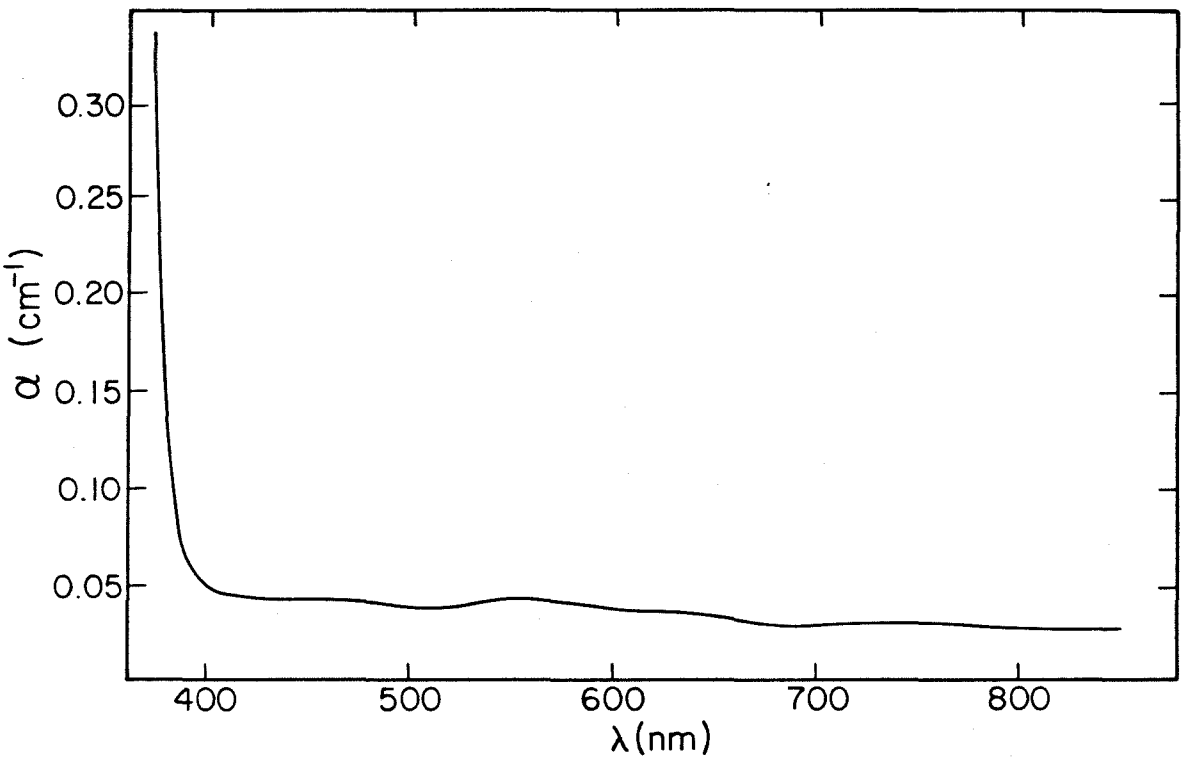

Figure 4.4. Absorption spectrum of undoped SBN:60.

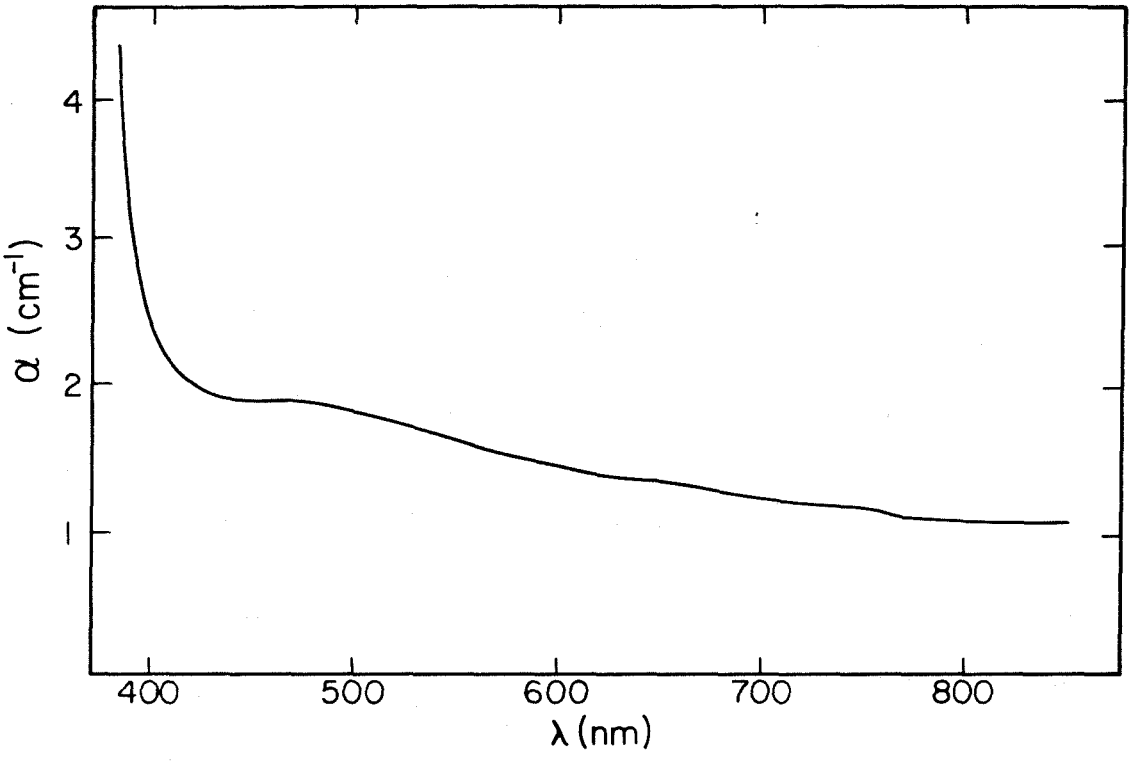

Figure 4.5. Absorption spectrum of heavily Ce-doped SBN:60.

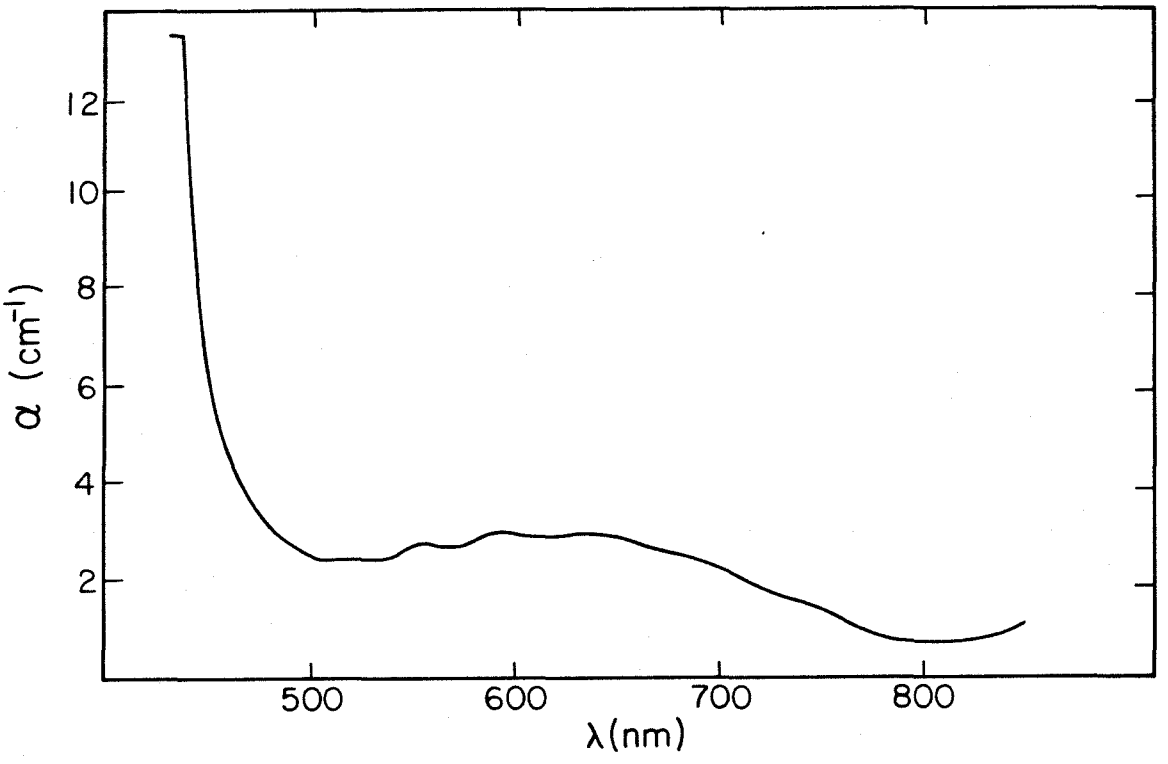

Figure 4.6. Absorption spectrum of heavily Fe-doped SBN:60.

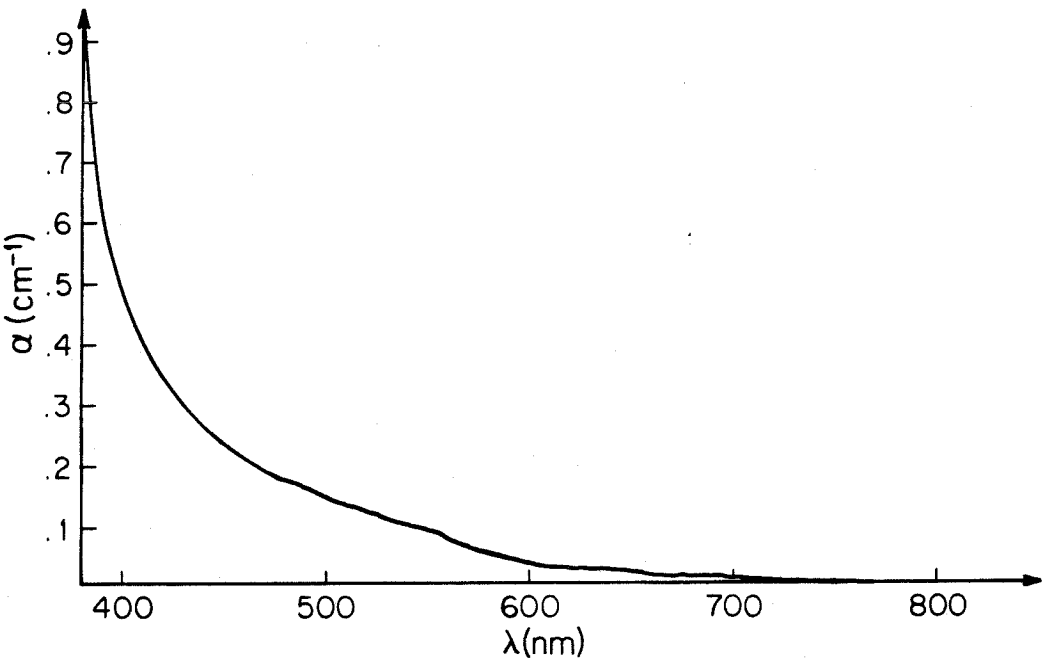

Figure 4.7. Absorption spectrum of lightly Ce-doped SBN:60.

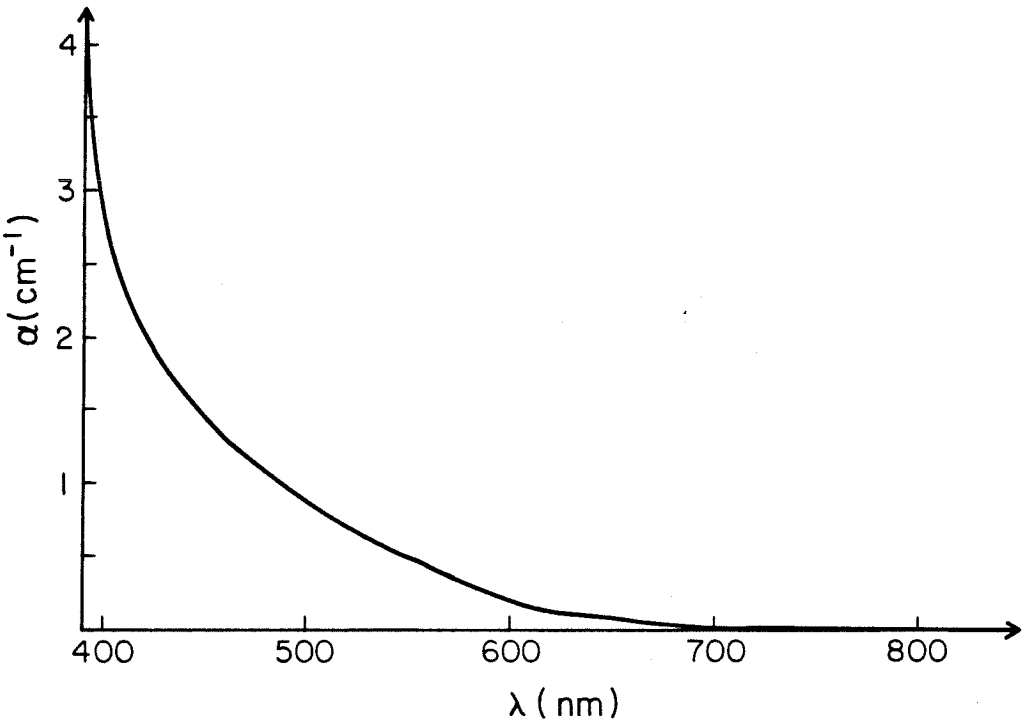

Figure 4.8. Absorption spectrum of lightly Ce-doped SBN:75.

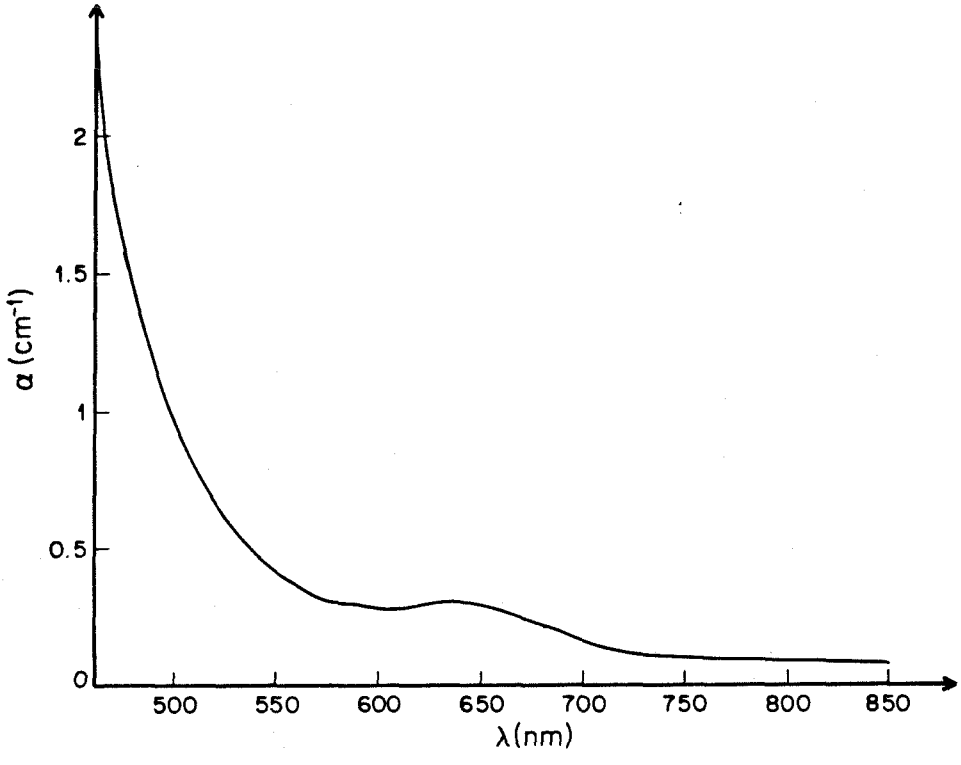

Figure 4.9. Absorption spectrum of doubly Ce- and Ca-doped SBN:60.

of light, the spectrum of the SBN:60 sample doped with Ce and Ca shows an absorption band in the red, centered about 650nm. Therefore, the addition of calcium impurities to cerium-doped SBN:60 should result in a photorefractive crystal with extended red response.

The last of the photorefractive crystals that were studied was barium strontium potassium sodium niobate (BSKNN). Its general formula is $Ba_{2-x}Sr_xK_{1-y}Na_yNb_5O_{15}$, and it was also grown at Rockwell International Corporation by the Czochralski technique. The structure of BSKNN, like that of SBN, permits the addition of dopants such as cerium to the host crystal.

The absorption spectrum of the BSKNN crystal, which was lightly doped with cerium impurities, is shown in Figure 4.10. Only visible light is significantly absorbed by the BSKNN sample, not unlike the absorption in the lightly Ce-doped SBN:60 and SBN:75 crystals, whose spectra are given in Figures 4.7 and 4.8. As the wavelength of the light is shifted towards the red and into the near-infrared, the BSKNN crystal becomes increasingly transparent.

The optical quality of nearly all of the samples was sufficiently high to allow measurements of their photorefractive properties. Data on iron-doped SBN:60 are not available since striations so affected the optical quality of the crystal that no reliable experimental values could be measured. It is believed[24] that better control of the growth conditions can eventually eliminate this problem.

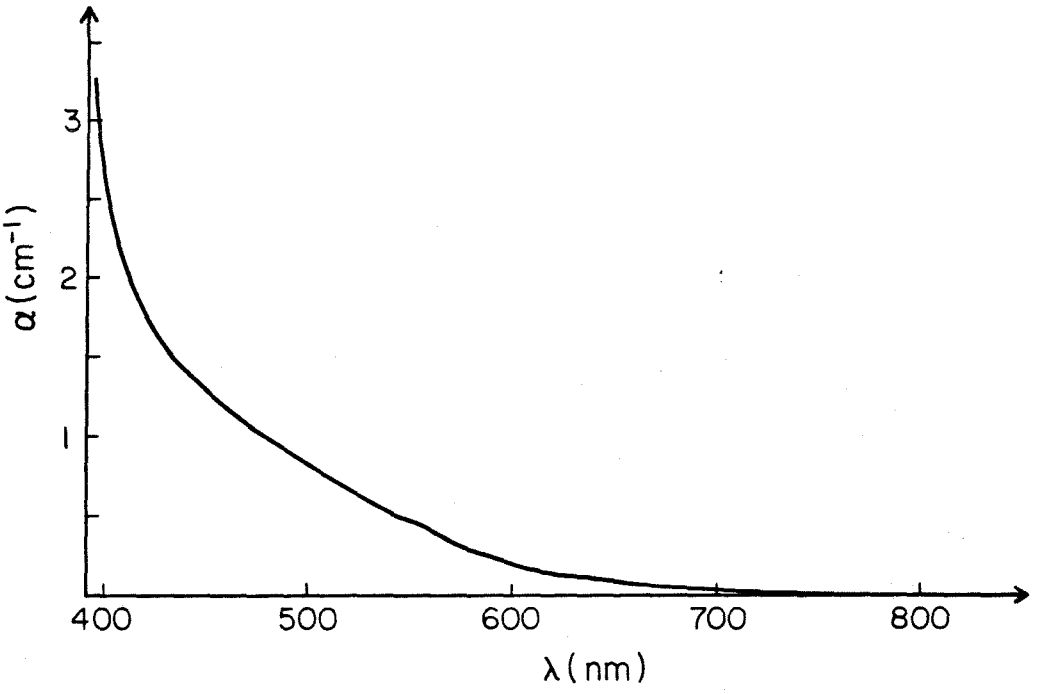

Figure 4.10. Absorption spectrum of lightly Ce-doped BSKNN.

4.4 References

1. R. L. Townsend and J. T. LaMacchia, J. Appl. Phys. 41, 5188 (1970).

2. P. Gunter, U. Fluckiger, J. P. Huignard, and F. Micheron, Ferroelectrics 13, 297 (1976).

3. F. S. Chen, J. Appl. Phys. 38, 3148 (1967).

4. R. Orlowski, L. A. Boatner, and E. Kratzig, Opt. Commun., 35, 45 (1980).

5. J. J. Amodei, D. L. Staebler, and A. W. Stephens, Appl. Phys. Lett. 18, 507 (1971).

6. J. B. Thaxter, Appl. Phys. Lett. 15, 210 (1969).

7. L. H. Lin, Proc. IEEE 57, 252 (1969).

8. M. Peltier and F. Micheron, J. Appl. Phys. 48, 3683 (1977).

9. V. M. Fridkin, B. N. Popov, and K. A. Verkhovskaya, Appl. Phys. 16, 313 (1978).

10. A. Ashkin, B. Tell, and J. M. Dziedzic, IEEE J. Quantum Electron QE-3, 400 (1967).

11. T. Nakamura, V. Fridkin, R. Magomadov, M. Takashige, and K. Verkhovskaya, J. Appl. Phys. Soc. Jpn. 48, 1588 (1980).

12. F. Micheron, A. Hermosin, G. B. Smith, and J. Nicolas, C.R. Acad. Sci. 8 (1971).

13. F. Jona and G. Shirane, Ferroelectric Crystals (Macmillan, New York, 1962).

14. P. V. Lenzo, E. G. Spencer, and A. A. Ballman, Appl. Phys. Lett. 11, 23 (1967).

15. S. T. Liu and R. B. Maciolek, J. Electron. Mater. 4, 91 (1975).

16. A. M. Glass, J. Appl. Phys. 40, 4699 (1969).

17. F. W. Ainger, W. P. Bickley, and G. V. Smith, Proc. Brit. Ceram. Soc. 18, 221 (1970).

18. T. Ikeda, K. Uno, K. Oyamada, A. Sagara, J. Kato, S. Takano, and H. Sato, Jpn. J. Appl. Phys. 17, 341 (1978).

19. J. Ravez and P. Hagenmuller, Mater. Res. Bull. 12, 769 (1979).

20. Sanders Associates, Nashua, NH 03061.

21. M. E. Lines and A. M. Glass, Principles and Applications of Ferroelectrics and Related Materials, (Clarendon, Oxford, 1977).

22. Rockwell International Corporation, Science Center, Thousand Oaks, CA 91360.

23. P. B. Jamieson, S. C. Abrahams, and J. L. Bernstein, J. Chem. Phys. 48, 5048 (1968).

24. R. R. Neurgaonkar and W. K. Cory, J. Opt. Soc. Am. B 3, 274 (1986).

5. PHOTOREFRACTIVE PROPERTIES

The photorefractive properties of the crystals introduced in the previous chapter are discussed here. Using the method of two-beam coupling, the photorefractive response times and the two-beam coupling coefficients of the crystals were determined experimentally. These values were measured under a variety of experimental conditions so that their dependence on variables such as intensity and optical wavelength could be determined.

The photorefractive properties were also investigated theoretically using the band transport models from Chapter 2, the results of which suggested a number of methods for enhancing or controlling the photorefractive effect in the crystals. Many of these techniques were implemented with varying degrees of success, some of which, for example, resulted in the development of an SBN crystal with an improved near-infrared photorefractive response.

5.1 The Two-Beam Coupling Experiment

Measurements of the two-beam coupling coefficients and photorefractive response times were performed with the experimental arrangement shown in Figure 5.1. Light from a number of possible laser sources first passed through an electrically controlled attenuator, composed of an electro-optic cell placed between crossed polarizers[1], so that the overall light intensity could be varied during the experi-

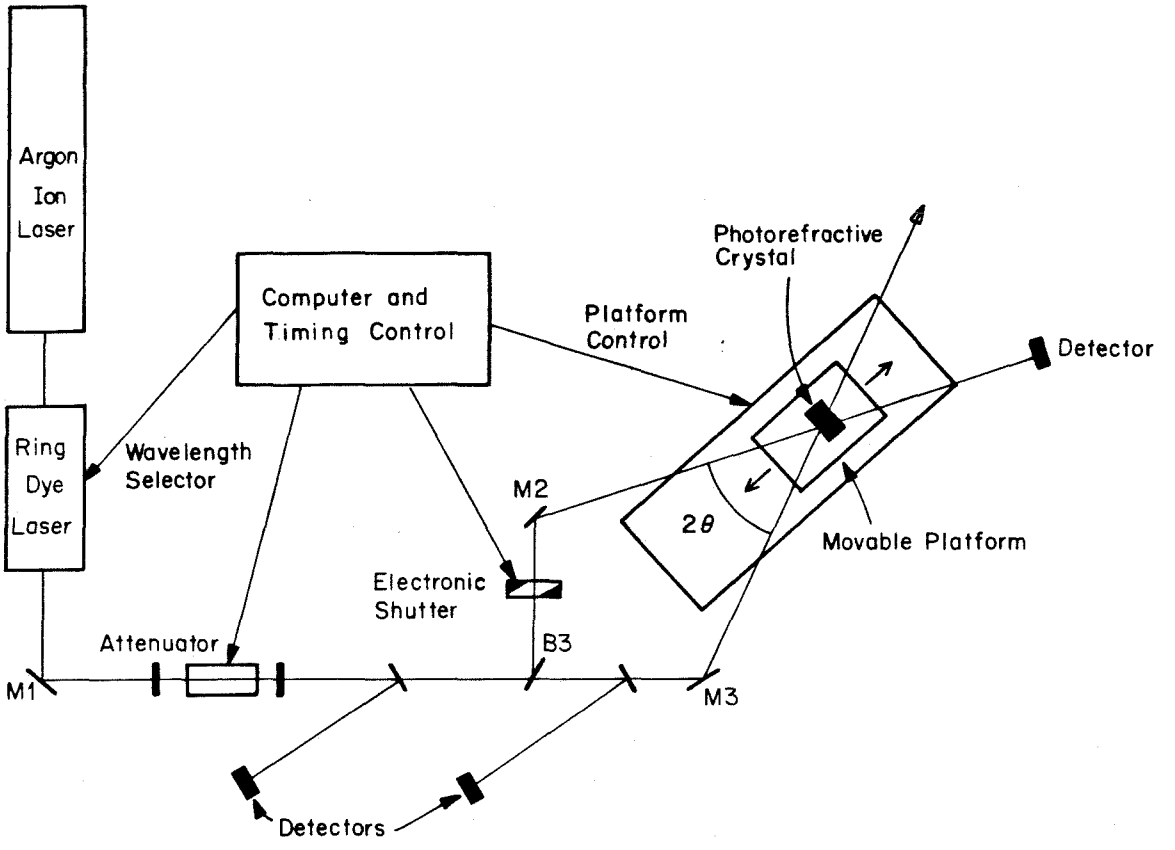

Figure 5.1. Experimental setup for two-beam coupling experiments.

ment. This attenuated beam was then split into two waves by a beamsplitter that ensured that the modulation index of the intensity interference pattern created by the intersection of these beams within the crystal was much less than one. The crystal was mounted on a movable platform that allowed the angle between the two beams to be varied so that the fringe spacing inside the crystal could be controlled. An electronic shutter was placed in the path of one of the beams so that any existing refractive index gratings within the crystal could be erased by illuminating the crystal with only one of the beams before the experiment was started. Finally, the input and output intensities were detected by four calibrated photodiodes which were connected to a computer that not only performed the calculations to determine Γ and τ, but also was used to control the experiment itself.

In order to observe a large photorefractive effect in these crystals, light of extraordinary polarization was used[2,3]. However, the orientation of the crystals was determined according to their electrooptic coefficients. Aligning the c-axis of the SBN samples parallel to the grating wave vector of the intensity interference pattern ensured that the large r_{33} coefficient was utilized. The $BaTiO_3$ and BSKNN crystals were oriented in such a manner that the angle between their c-axis and the grating wave vector was 10°. Although the optimal value[4] is 20°, 10° was chosen to avoid using beams close to 90° incidence, since the index of refraction of these crystals is so large (typically 2.3 to 2.4).

With this experimental set-up, the two-beam coupling coefficient Γ and the photorefractive response time τ of a given crystal could be obtained under a number of different conditions, since the light intensity, the wavelength of the light, and the period of the fringe spacing or the grating wavelength could be changed at will. At times, specific experiments were conducted in which the temperature of the crystals was varied, or in which an external electric field was applied to a sample. Thus, further dependencies of Γ and τ on experimental parameters were determined. Finally, some of the crystals were subjected to oxidation and reduction treatments to determine what effects the dark conductivity, oxygen vacancies, and the density of traps have on the photorefractive properties of these materials.

5.2 Dependence of Γ and τ on Grating Wavelength

The grating wavelength λ_g is defined by $\lambda_g=2\pi/k$, where k is the grating wave number of the intensity interference pattern (see Eq. [2.1]). In Figures 5.2 to 5.7, the two-beam coupling coefficients and response times of the photorefractive crystals are shown. An argon ion laser operating at 514.5 nm was used to obtain the data which were taken at room temperature with no electric fields applied to the crystals.

Although cerium is an effective dopant for enhancing the photorefractive effect in SBN, since its addition also decreases the response time of the crystal, the active

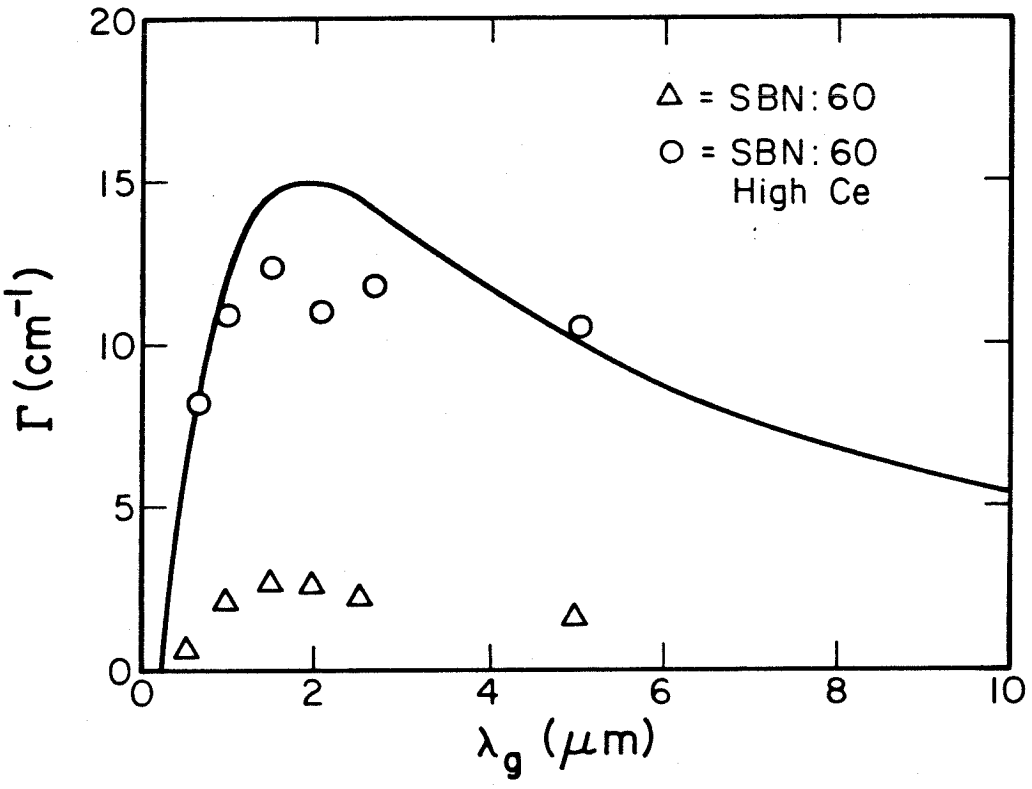

Figure 5.2. Two-beam coupling coefficient versus grating wavelength for E_0 = 0 V/cm.

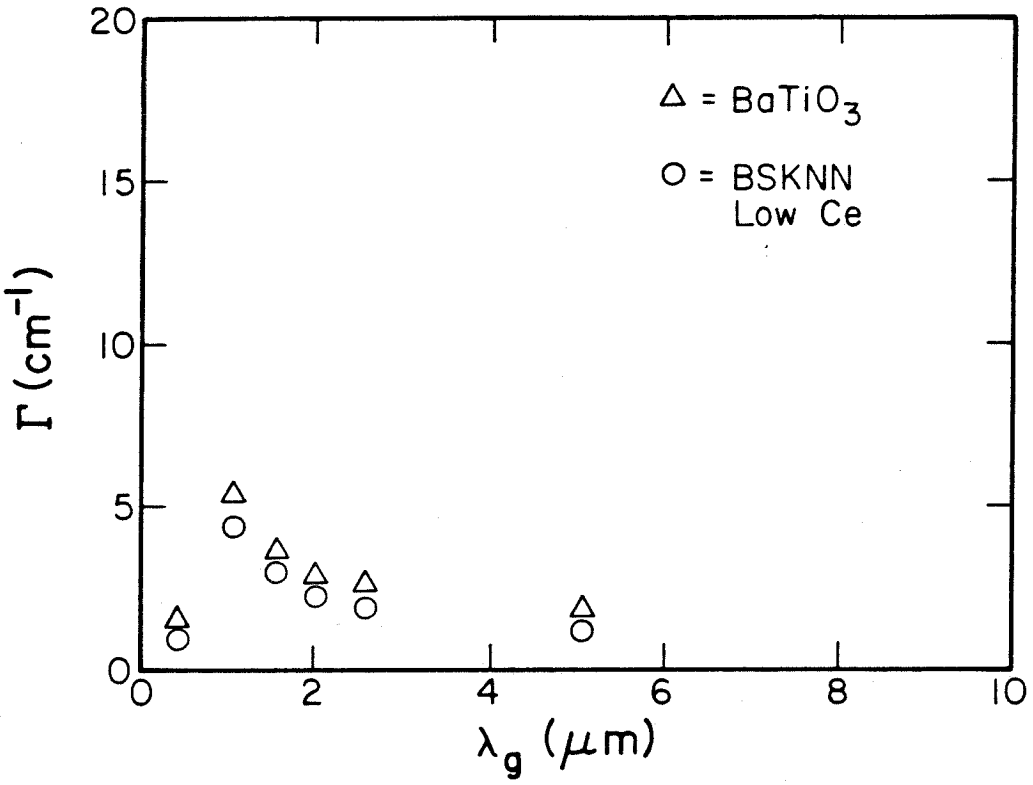

Figure 5.3. Two-beam coupling coefficient versus grating wavelength for E_0 = 0 V/cm.

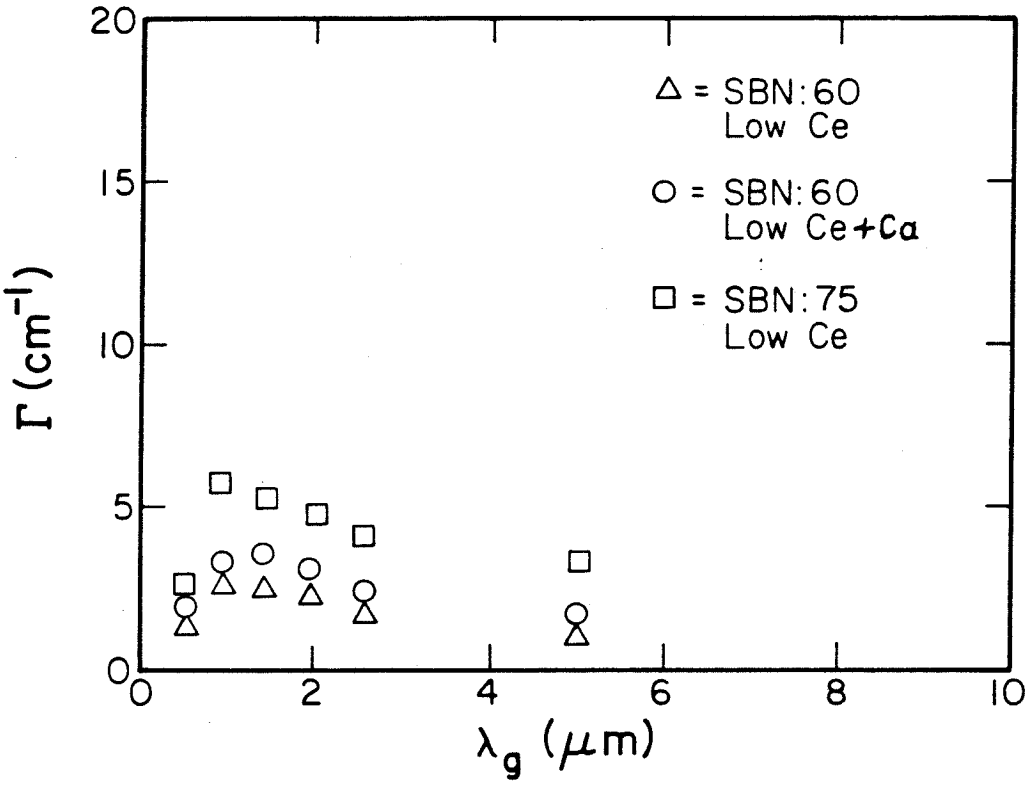

Figure 5.4. Two-beam coupling coefficient versus grating wavelength for E_0 = 0 V/cm.

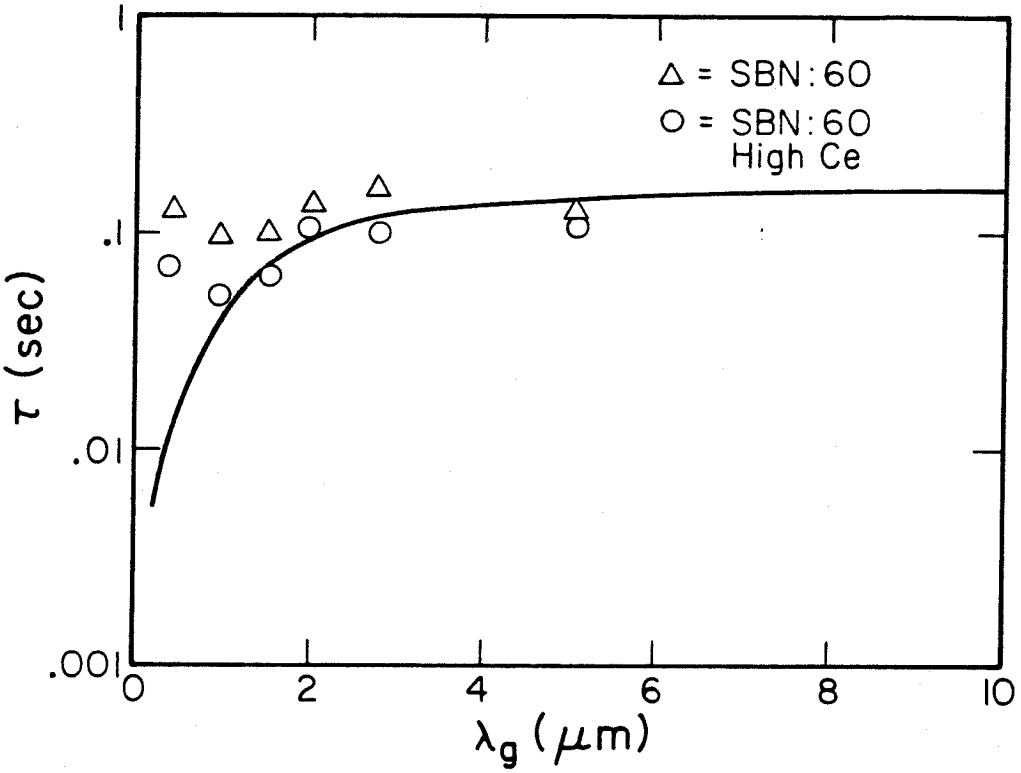

Figure 5.5. Photorefractive response time versus grating wavelength at I_0 = 1 W/cm^2 for E_0 = 0 V/cm.

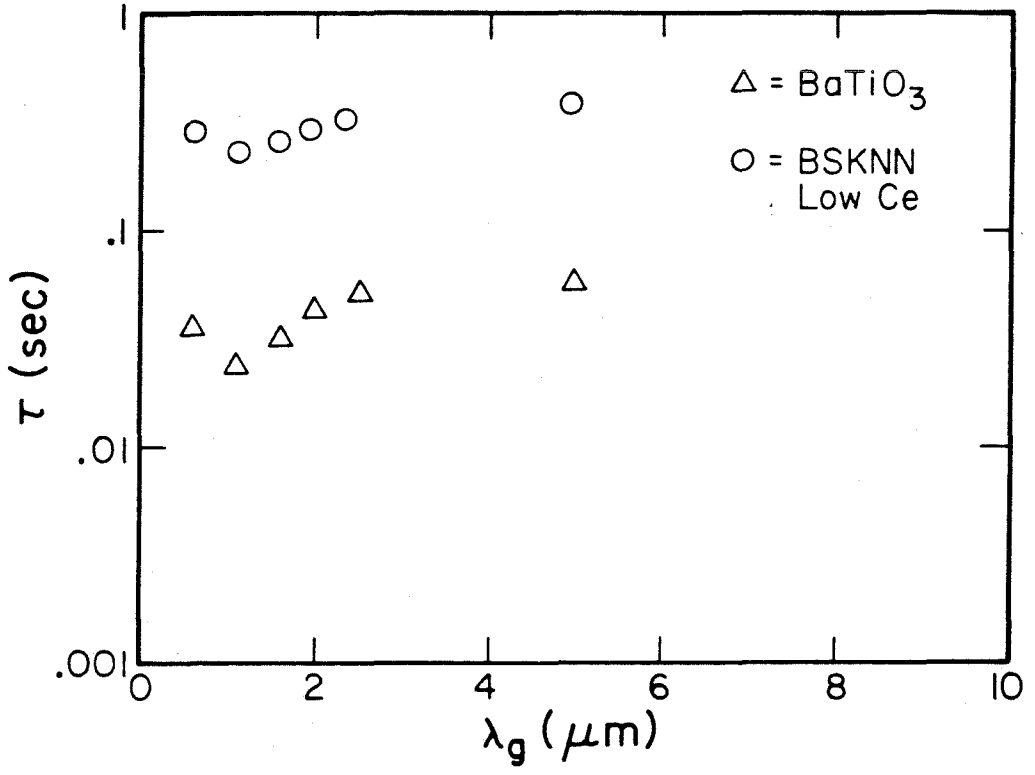

Figure 5.6. Photorefractive response time versus grating wavelength at I_0 = 1 W/cm^2 for E_0 = 0 V/cm.

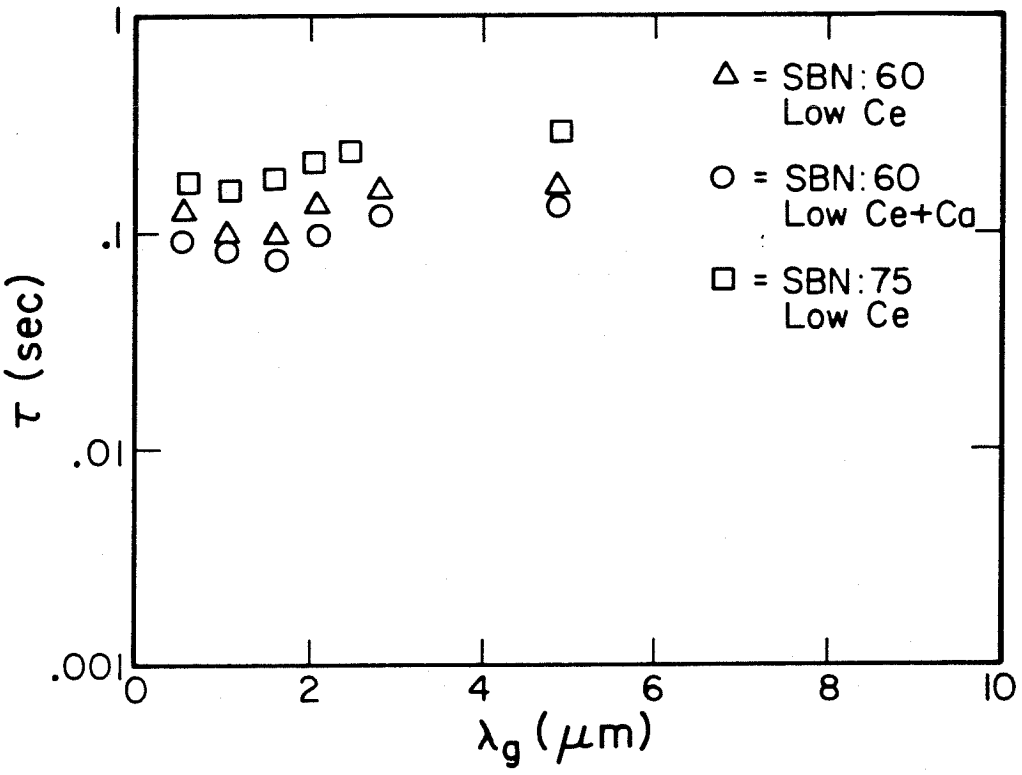

Figure 5.7. Photorefractive response time versus grating wavelength at I_0 = 1 W/cm^2 for E_0 = 0 V/cm.

impurity or impurities in the undoped SBN:60 and $BaTiO_3$ samples were initially not known. An elemental analysis by nuclear activation[5] of $BaTiO_3$, undoped SBN:60, and Ce-doped SBN:60 was performed as an attempt to identify these impurities. Table 5.1 shows the results. Since undoped SBN:60 is photorefractive while containing only trace levels of cerium, there must be other photorefractive species for SBN besides cerium. In fact, Table 5.1 indicates that there are significant amounts of Fe, Ni, Mo, and Ta impurities in the undoped SBN crystal, and Fe and Ni, for example, are known to be effective photorefractive centers in $LiNbO_3$[6]. Similarly, there are large quantities of iron and strontium in the $BaTiO_3$ crystal. Since strontium has yet to be directly associated with the photorefractive effect, the activity of $BaTiO_3$ is attributed to iron. This claim is further justified by the recent work of Klein and Schwartz[7] who found that Fe impurities in both the Fe^{2+} and Fe^{3+} states are the predominant photorefractive species for $BaTiO_3$.

The solid curves in Figures 5.2 and 5.5 were obtained from first principles calculations using the one species, one charge carrier band transport model of Chapter 2 to characterize the photorefractive effect in Ce-doped SBN:60. In order to apply these equations, several material parameters were needed. The relative dielectric constant, the electrooptic coefficient, and the background refractive index are readily available[8]; $\varepsilon_{33} = 880$, $r_{33} = 420$ pm/V, and $n_e = 2.3$. However, values for the mobility, the photoionization

Table 5.1. Elemental analysis by weight of $BaTiO_3$, undoped SBN:60, and heavily Ce-doped SBN:60.

Elements & Units	$BaTiO_3$	SBN:60	SBN:Ce
U PPM	< 0.1	< 0.1	< 0.1
TH PPM	< 0.2	< 0.3	< 0.2
NA PPM	< 30.0	30.0	< 30.0
SC PPM	1.2	0.04	0.03
CR PPM	< 5.0	< 5.0	< 5.0
FE %	0.040	0.029	0.014
CO PPM	0.2	0.3	0.3
NI PPM	< 50.0	50.0	50.0
ZN PPM	5.0	7.0	5.0
AS PPM	< 1.0	< 1.0	< 1.0
SE PPM	< 10.0	< 5.0	< 5.0
BR PPM	< 0.5	< 0.5	< 0.5
MO PPM	< 2.0	11.0	4.0
SB PPM	0.7	0.5	0.5
CS PPM	< 1.0	< 0.2	< 0.2
BA PPM	540000.0	160000.0	150000.0
LA PPM	0.4	0.2	1.0
HF PPM	< 2.0	< 0.2	< 0.2
TA PPM	< 0.5	< 12.0	13.0
W PPM	< 3.0	< 3.0	< 1.0
AU PPB	< 5.0	< 5.0	5.0
CE PPM	2.0	< 1.0	47.0
ND PPM	INTERFER	INTERFER	INTERFER
SM PPM	0.05	0.01	0.32
EU PPM	< 0.05	0.07	0.10
TB PPM	< 0.1	< 0.1	< 0.1
YB PPM	< 0.50	< 0.05	0.05
LU PPM	< 0.06	< 0.01	< 0.01
SR PPM	900.0	148000.0	135000.0
RB PPM	< 5.0	< 5.0	< 5.0

cross section, and the two-body recombination rate coefficient in Ce-doped SBN:60 are not known and are difficult to obtain.

Estimates of these quantities are given for $BaTiO_3$ [2,9-12]. Since both $BaTiO_3$ and SBN are very electrooptic, ferroelectric materials with similar photorefractive properties, values for Ce-doped SBN were approximated by the data given for $BaTiO_3$; that is, $s_e^C = s = 1.6\times10^{-19}$ cm^2, $\mu_e=\mu=0.5 cm^2/Vsec$, and $\gamma_e^C=\gamma_R=5\times10^{-8} cm^3/sec$, where it was implicitly assumed that the electron was the charge carrier in SBN. This assumption is justified in the next section.

The last two quantities needed were the dopant density N_{Ce} and the compensative acceptor density N_A^Cs. They were found by fitting the theory to the data in Figures 5.2 and 5.5. The results were $N_{Ce}=10^{19} cm^{-3}$ and $N_A^C=N_A=10^{16} cm^{-3}$.

In the sections to follow calculations using this model are presented that theoretically describe the dependence of the two-beam coupling coefficient and the photorefractive response time of Ce-doped SBN:60 on various parameters such as the external electric field and the carrier mobility.

5.3 The Sign of the Charge Carrier in the Crystals

Consider Eqs. [2.18], [3.7], and [3.8] with $\Omega=0$ and $E_0=0$. The sign of the two-beam coupling coefficient of a refractive index grating formed in a photorefractive index grating formed in a photorefractive crystal along the c-axis

can be written as

$$\text{Sign } \{\Gamma\}=\text{sign } \{e\}\text{sign}\{r_{33}\}. \qquad [5.1]$$

Thus, the sign of the charge carrier is given by

$$\text{Sign } \{e\}=\text{sign}\{\Gamma\}\text{sign}\{r_{33}\}. \qquad [5.2]$$

Therefore, by determining sign $\{\Gamma\}$ and sign $\{r_{33}\}$, the sign of the charge carrier and, hence, the type of carrier (electron or hole) in a crystal can be found from Eq. [5.2].

The coupling coefficients of the crystals were given in the previous section. The direction of the c-axis in the experiments was defined so that it pointed from the face of the crystal that was positive when poled to the face that was negative when poled. The signs of the r_{33} coefficients were found by considering the electrooptic effect in the crystals.

In birefringent crystals such as SBN, the functional dependence of the extraordinary and ordinary refractive indices are

$$n_e(E)=n_e-\tfrac{1}{2}n_e^3 r_{33}E \qquad [5.3]$$

and

$$n_o(E)=n_o-\tfrac{1}{2}n_0^3 r_{13}E, \qquad [5.4]$$

where $n_e(E)$ is the extraordinary index with applied field E, n_e is the extraordinary index with no applied field, $n_0(E)$ is the ordinary index with applied field E, and n_0 is the ordinary index with no applied field.

In crystals such as $BaTiO_3$ and SBN, $n_0>n_e$ and $|n_e^3 r_{33}| > |n_0^3 r_{13}|$ [1,8]. This implies that if $|n_e(E)-n_0(E)|$ decreases with increasing E, then $r_{33}<0$.

If a plane polarized wave is incident on such a

material, the ordinary and extraordinary rays are shifted in phase by $\Delta\phi$ relative to each other, after traveling a distance d in the substance.

$$\Delta\phi = \frac{2\pi}{\lambda_0} d \left| n_e(E) - n_0(E) \right| , \qquad [5.5]$$

where λ_0 is the wavelength in vacuum.

The crystal in question will, therefore, act as a retarder of increased or decreased magnitude, in a higher electric field, depending on the sign of r_{33}. To be specific, if the crystal acts as a waveplate of lower order as the electric field increases, then it must have an $r_{33}<0$. Using this characteristic the sign of the r_{33} coefficients in the crystals was determined with the following experiment.

A gypsum wedge placed between crossed polarizers displays dark fringes at points where the wedge acts as a full wave plate (gypsum is birefringent). A crystal is now placed, along with the wedge, between the crossed polarizers. As the electric field on the crystal is increased the fringes will be seen to shift. If the fringes move towards the thicker edge of the wedge, then the crystal is acting as a wave plate of lower order, so r_{33} must be negative. The opposite is true if the fringes move in the other direction.

The results of this experiment are shown in Table 5.2, which indicates that the electron is the charge carrier in the tungsten bronze ferroelectrics. Thus, the one carrier models of Chapter 2 are sufficient to describe the photorefractive effect in these crystals. However, charge trans-

Table 5.2. Sign of the charge carriers in the photorefractive crystals

Crystal	Sign (Γ)	Sign (r_{33})	Sign (e)	Type of Carrier
SBN:60	+	-	-	electron
SBN:60 (Low Ce)	+	-	-	electron
SBN:60 (High Ce)	+	-	-	electron
SBN:60 (Low Ce + Ca)	+	-	-	electron
SBN:75 (Low Ce)	+	-	-	electron
BSKNN (Low Ce)	+	-	-	electron
$BaTiO_3$[7,13,14]	+,-	+,-	+,-	electron/hole

port in $BaTiO_3$ is provided by both electrons and holes. The two carrier band transport model of Section 2.2.2 is, therefore, needed to describe the photorefractive properties of barium titanate.

5.4 Dependence of Γ on Applied Electric Field

Figure 5.8 shows the theoretical dependence of the two-beam coupling coefficient Γ on the grating wavelength λ_g of Ce-doped SBN:60 when an electric field of 2kV/cm is applied to the crystal along the c-axis. A maximum value of $35cm^{-1}$ is predicted at a grating spacing of 5μm. Such a large response would then make even very thin samples of cerium-doped SBN:60 useful photorefractive media.

Voltages of up to 3000V were applied to many of the crystals, including the heavily Ce-doped SBN:60. The electrical connections were made through contacts formed by depositing Au or Pt on the c-faces of the crystals. The values of Γ were then measured using the two-beam coupling technique.

In practice, very large values of Γ were never obtained. If the fields were applied with polarities opposite to that of the poling voltages, the two-beam coupling in the crystals would decrease. Furthermore, if the magnitude of these fields was sufficiently high, this decrease was irreversible since partial depoling of the crystals would result.

Reversing the polarity of the voltages so that they were

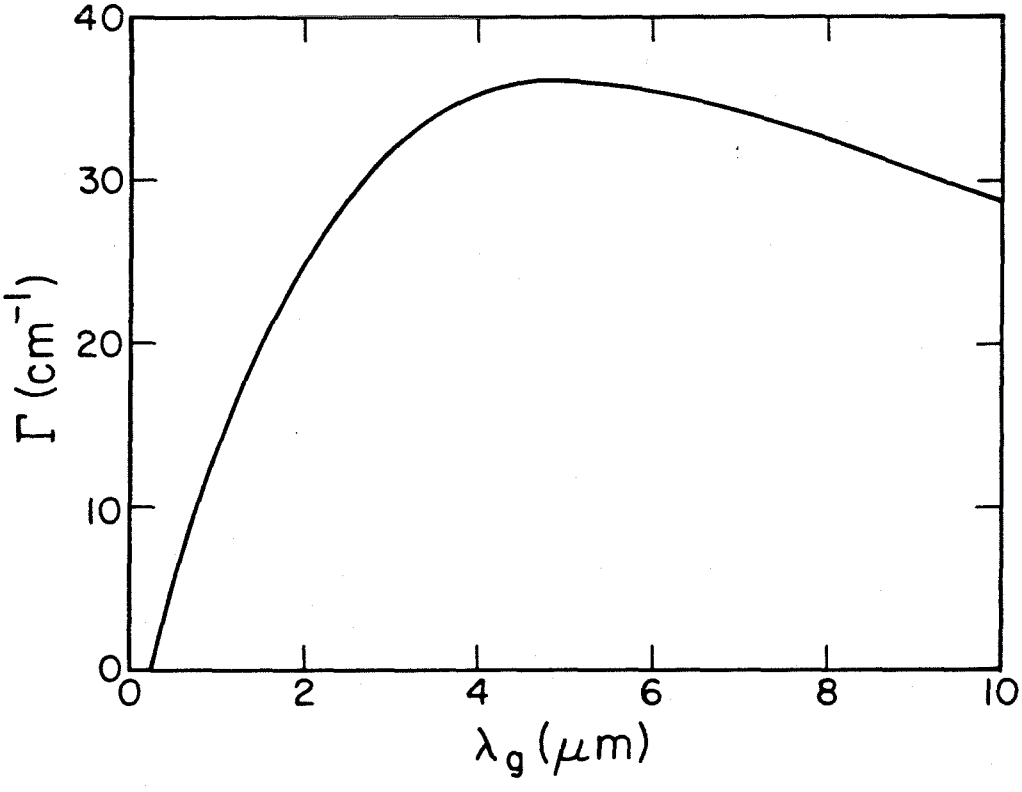

Figure 5.8. Two-beam coupling coefficient versus grating wavelength for E_0 = 2 kV/cm.

the same as the poling fields presented other difficulties. For fields below 1kV/cm in magnitude, no appreciable changes in Γ were detected. However, as the electric fields applied to the crystals were increased, induced stresses deformed the materials, and the incident beams were distorted, precluding any further measurements.

Therefore, the application of electric fields to the crystals to control their photorefractive two-beam coupling coefficients is of limited use.

5.5 Dependence of τ on Laser Intensity

According to the photorefractive theory of Chapter 2, the photorefractive response time τ is a decreasing function of total laser intensity I_0. As the intensity is increased, more energy is deposited into the crystal per unit time, and thus the photorefractive index grating forms more rapidly. The specific functional dependence of τ on I_0 depends on whether one or two photorefractive species are involved in the process.

For the case in which only one species contributes to the photorefractive effect, the response time can be written as (see Eq. [2.22])

$$\tau = a I_0^{-1}, \qquad [5.6]$$

where a is a constant of proportionality in units of J/cm^2. If two photorefractive species are involved, then, from Eq. [2.34], the response times can be written as

$$\tau_{\pm} = a_{\pm}^{(1)} I_0^{-1} + a_{\pm}^{(2)} I_0^{-2} + \ldots, \qquad [5.7]$$

where the $a_{\pm}^{(i)}$'s are the coefficients in the Laurent series expansion of $\tau\pm$.

An experiment to determine the functional dependencies of τ on I_0 in the $BaTiO_3$ and the heavily Ce-doped SBN:60 crystals was performed. Using a dye laser, the response times of the crystals were obtained as a function of light intensity over the spectral range of rhodamine 6G. A typical set of points is shown in Figures 5.9 and 5.10.

Next, a curve of the form $\tau=aI^{-x}$ was fit to each of the data sets, and the parameters a and x were determined. The results are given in Figures 5.11 to 5.14. They indicate that x is approximately unity in $BaTiO_3$ which suggests that only one photorefractive species is present in this crystal. This was expected since the only significant impurity in $BaTiO_3$ was iron (see Table 5.1). However, the values of x in the Ce-doped SBN:60 sample differed from unity. This implies that a second photorefractive species may exist in this crystal, and, indeed, the data in Table 5.1 indicate the same because of the substantial iron content of this crystal. Hence, the photorefractive properties of the Ce-doped SBN:60 crystal may be better explained with the two species model of Chapter 2, rather than with the one species theory. However, the latter is much simpler to apply, and, for this reason, it will continue to be used throughout the rest of this chapter.

5.6 Dependence of Γ and τ on Oxidation State

The oxidation state of a photorefractive crystal can be

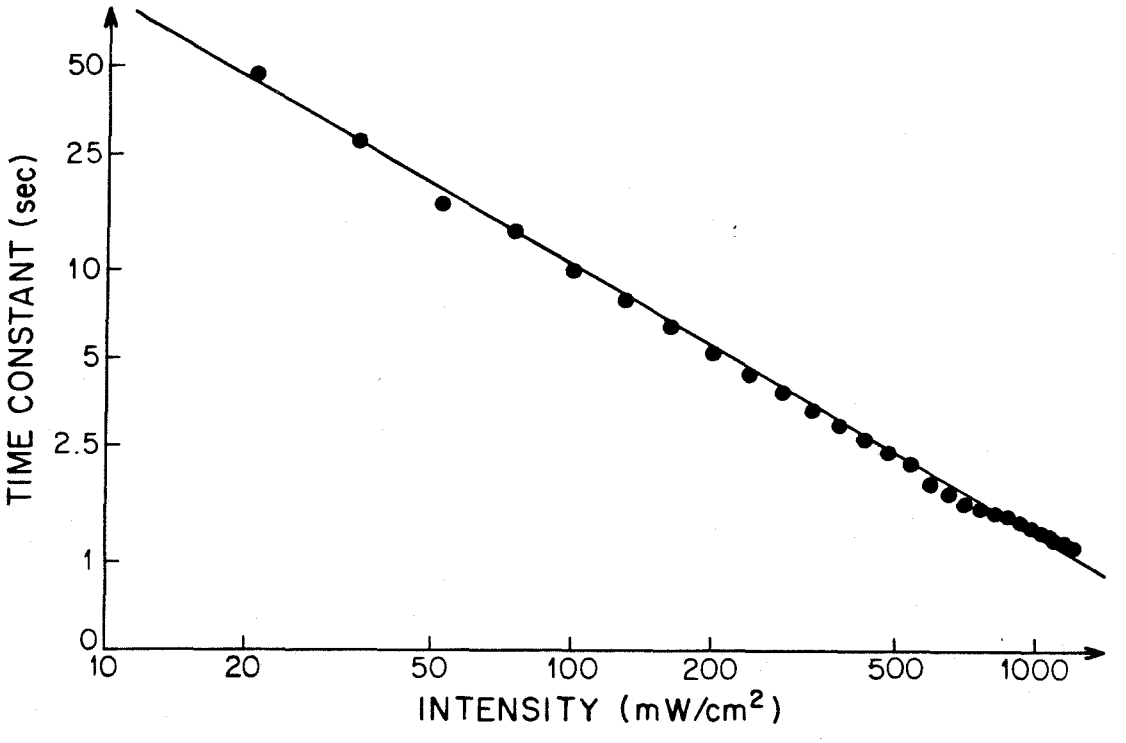

Figure 5.9. Photorefractive response time of the heavily Ce-doped SBN:60 crystal versus intensity for λ = 565 nm and λ_g = 1.4 μm.

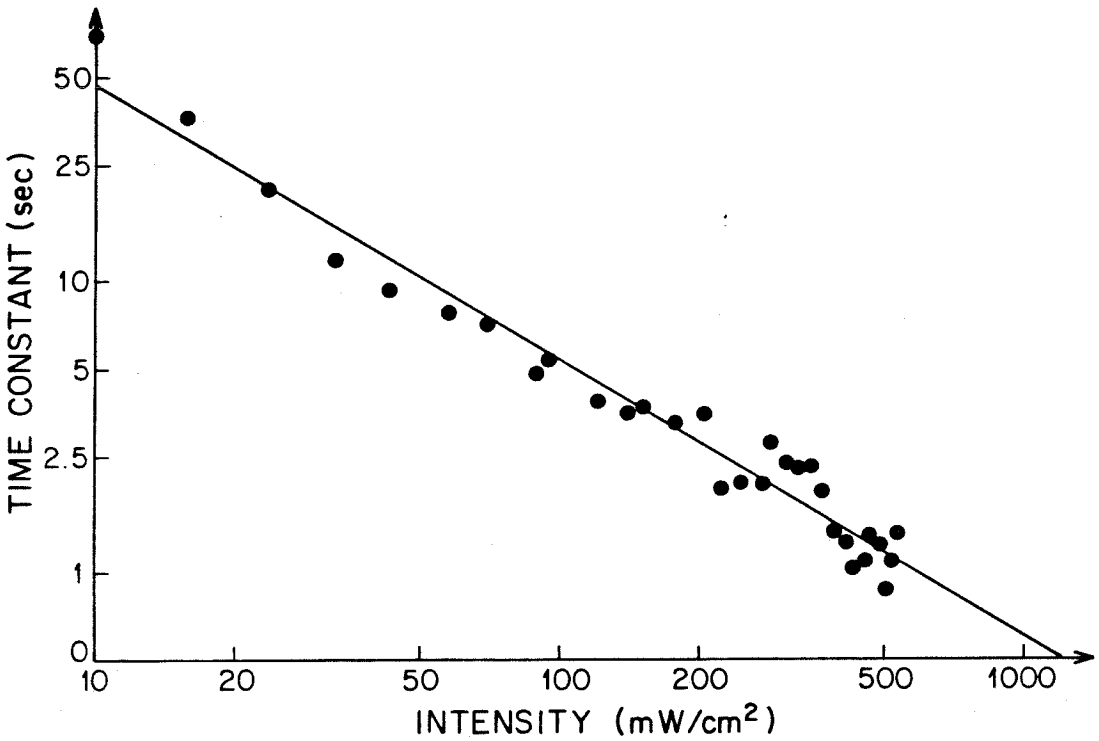

Figure 5.10. Photorefractive response time of the $BaTiO_3$ crystal versus intensity for λ = 605 nm and λ_g = 1.4 μm.

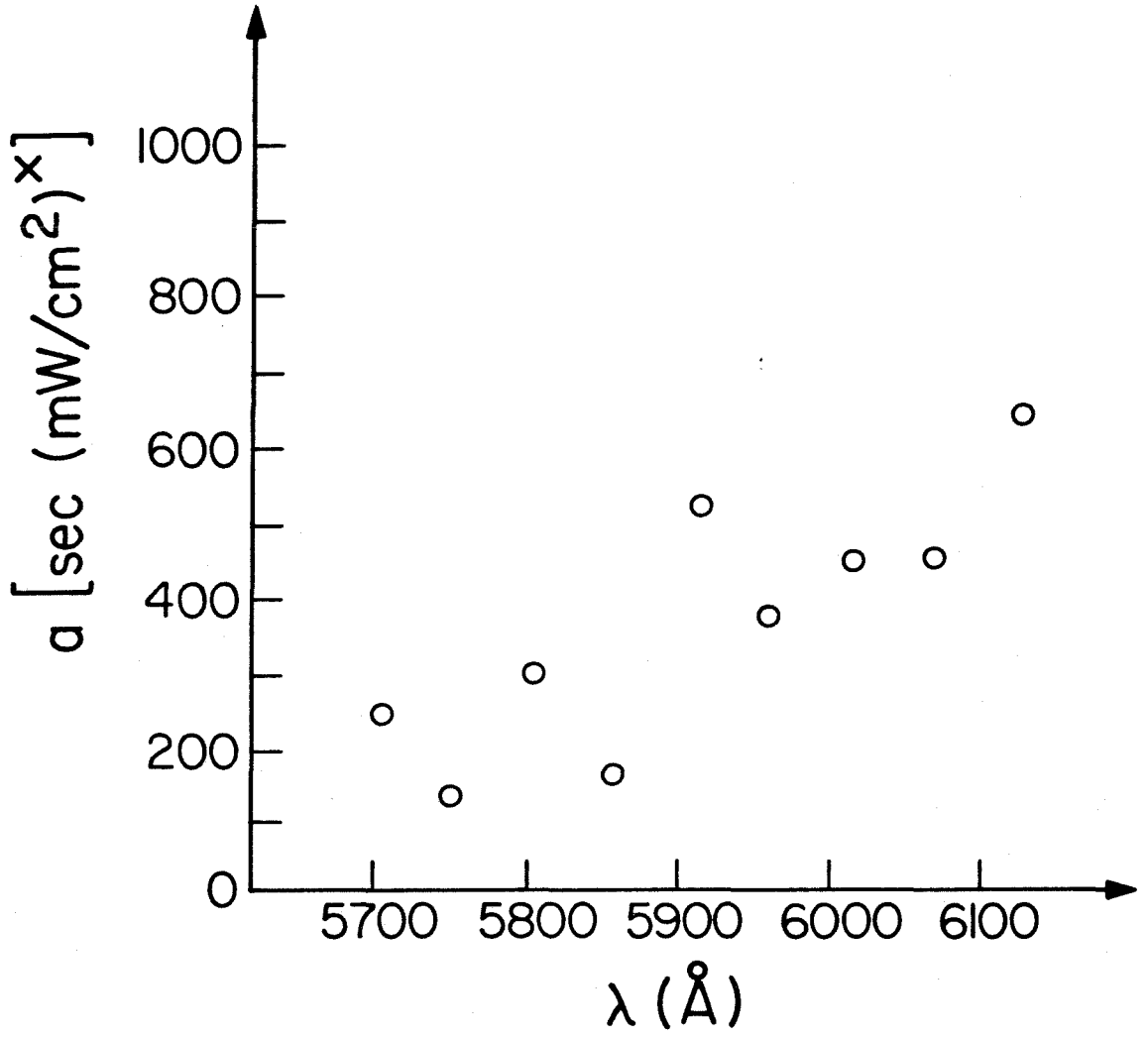

Figure 5.11. The constant a versus optical wavelength for $BaTiO_3$ at λ_g = 1.4 μm.

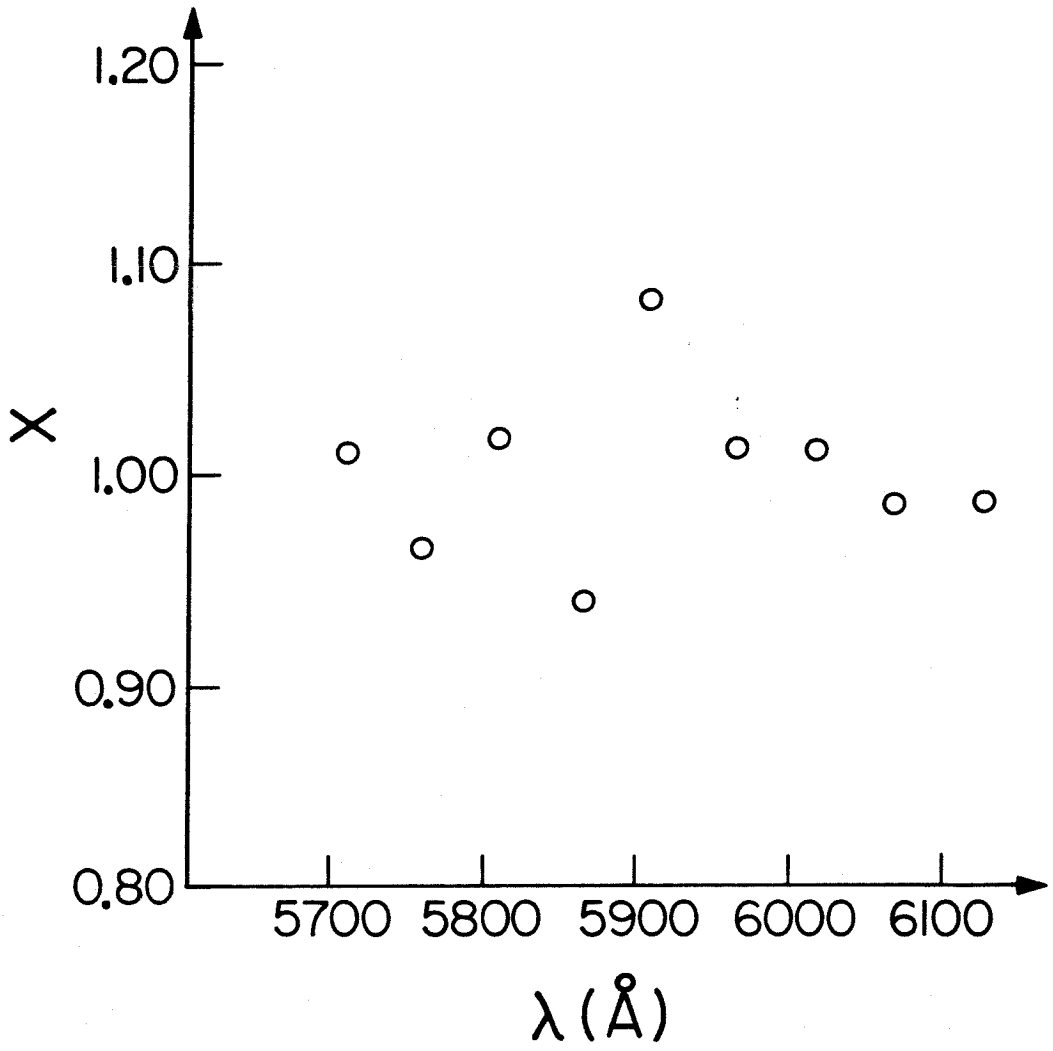

Figure 5.12. The exponent x versus optical wavelength for $BaTiO_3$ at λ_g = 1.4 μm.

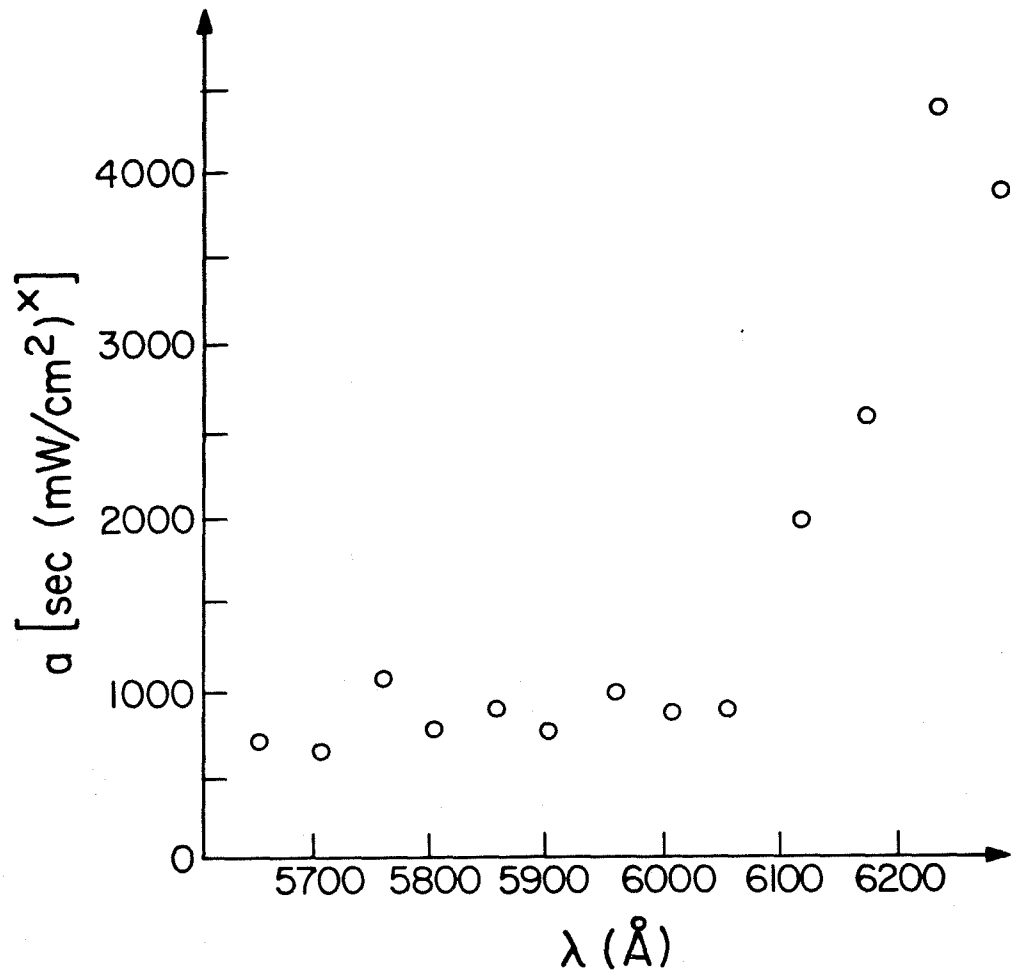

Figure 5.13. The constant a versus optical wavelength for heavily Ce-doped SBN:60 at λ_g = 1.4 μm.

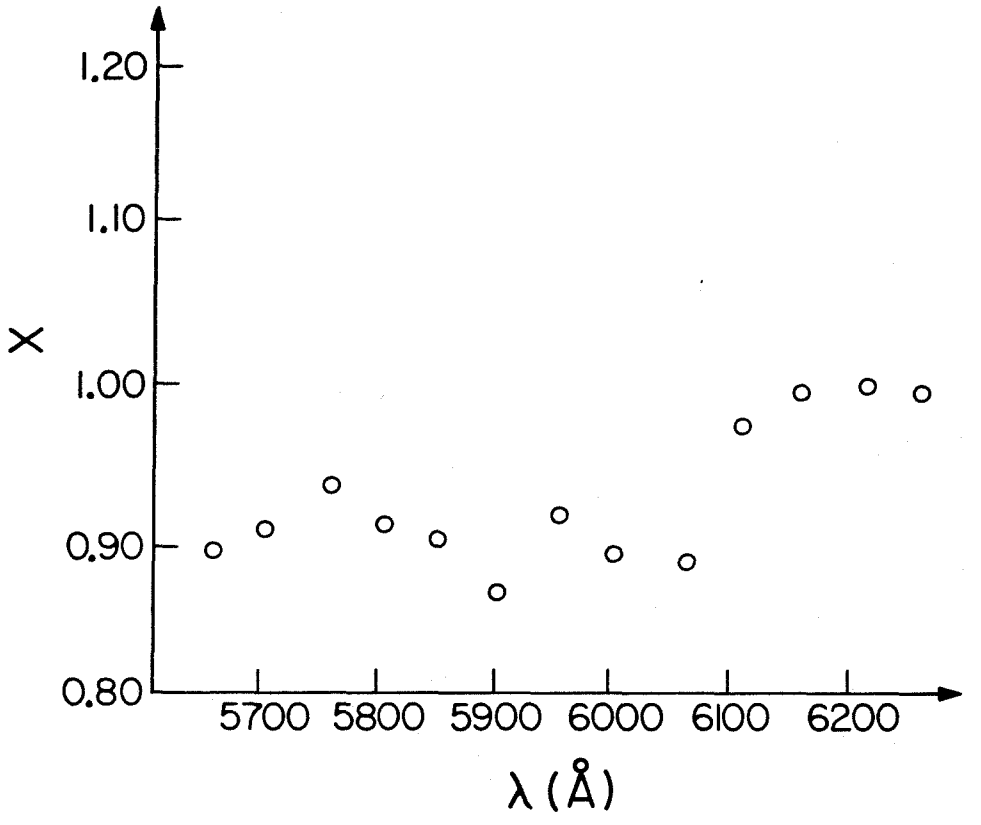

Figure 5.14. The exponent x versus optical wavelength for heavily Ce-doped SBN:60 at λ_g = 1.4 μm.

defined in terms of the number density of oxygen vacancies in the crystal. Oxygen vacancies[15-21] are formed to compensate for the charge imbalance created when sites in the crystal are filled by impurity ions of the wrong valence, such as when Fe^{3+} ion is substituted for Ti^{4+} in $BaTiO_3$. A crystal is said to be reduced if it contains a large number of oxygen vacancies, while in an oxidized crystal the number of oxygen vacancies is small.

The number of oxygen vacancies and, hence, the oxidation state of a material can be modified through oxidation and reduction treatments. Reduction is the process whereby oxygen is removed from a crystal, leaving behind oxygen vacancies. It is typically performed by heating a sample in an oxygen deficient atmosphere, or in a vacuum, to a high temperature, and then quickly cooling or quenching it back to room temperature. The reduction process is given by

$$O^{2-} \rightarrow \tfrac{1}{2}O_2 + V_0 + 2e^-, \qquad [5.8]$$

where V_0 represents an oxygen vacancy.

Oxidation is the inverse process. A crystal is heated to a high temperature in an oxygen rich atmosphere and is then quenched back to room temperature; it is given by

$$V_0 + 2e^- + \tfrac{1}{2}O_2 \rightarrow O^{2-} \qquad [5.9]$$

where oxygen is now added to the material, thereby reducing the number of oxygen vacancies.

Oxidation and reduction treatments were suggested[22] as methods for controlling and modifying the photorefractive

response of Ce-doped SBN:60. In this crystal, cerium is present in both the Ce^{3+} and the Ce^{4+} valence states. Since electron transport is dominant in SBN:60, the Ce^{3+} ions are the donors of electrons while the Ce^{4+} ions are the electron traps. The effect of reduction is, therefore, to decrease the number of traps by converting Ce^{4+} ions to Ce^{3+} ions by the following process:

$$4Ce^{4+} + 2O^{2-} \rightarrow (4Ce^{4+}+2V_O+4e^-)+O_2$$
$$\rightarrow (4Ce^{3+}+2V_O)+O_2. \qquad [5.10]$$

Oxidation, on the other hand, increases the number of traps by converting Ce^{3+} ions to Ce^{4+} ions by the inverse process:

$$(4Ce^{3+}+2V_O)+O_2 \rightarrow 4Ce^{4+}+4e^-+2V_O+2O$$
$$\rightarrow 4Ce^{4+}+2O^{2-}. \qquad [5.11]$$

The theoretical dependence of the two-beam coupling coefficient Γ and the response time τ of the heavily cerium-doped SBN:60 crystal on trap density is shown in Figures 5.15 and 5.16. They indicate that both Γ and τ should decrease with decreasing trap density given by the parameter N_A, the compensative acceptor number density, which is equal to the number density of electron traps in the dark. Although the exact number density of traps was difficult to measure, the two-beam coupling coefficient was varied from less than 0.1 cm^{-1} to 15 cm^{-1} by heating the crystal in atmospheres with different oxygen partial pressures, thereby changing its oxidation state.

The predicted variation of the photorefractive response

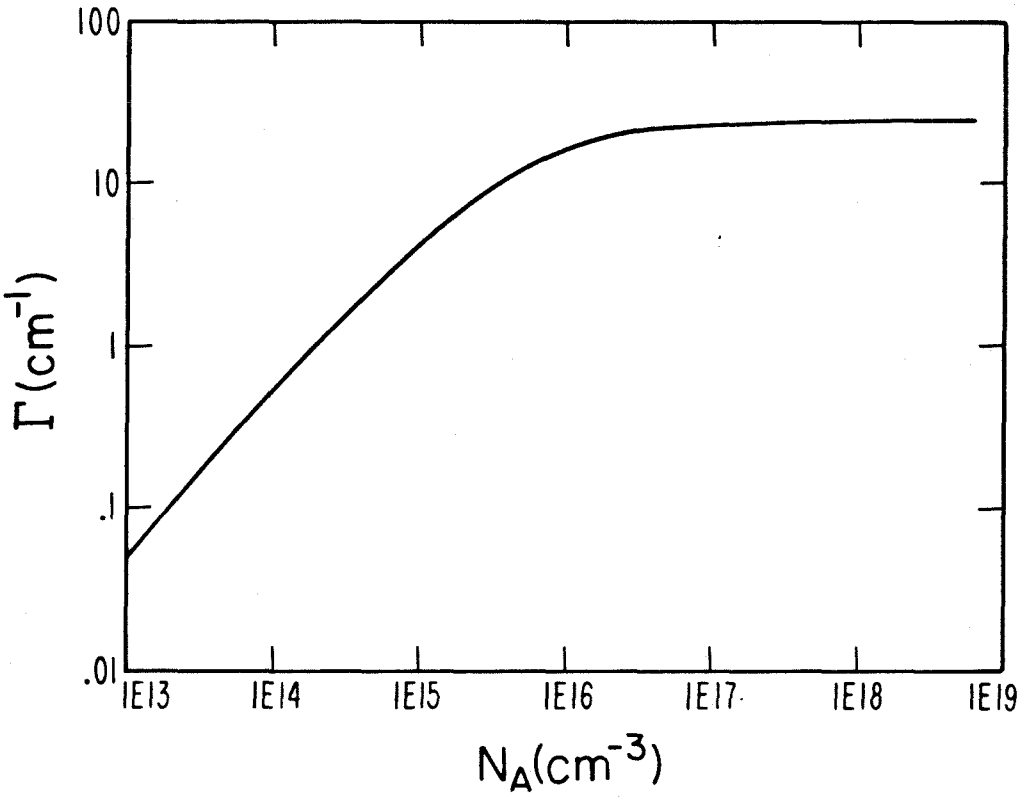

Figure 5.15. Two-beam coupling coefficient versus trap density for E_0 = 0 V/cm and λ_g = 5 μm.

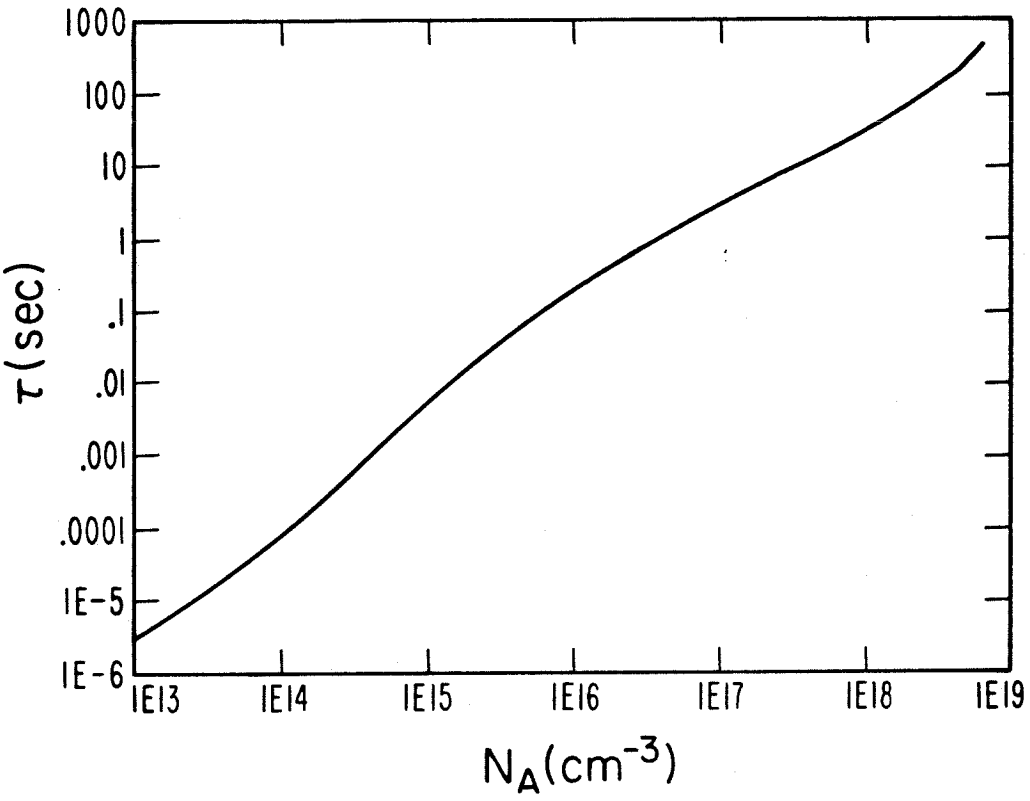

Figure 5.16. Photorefractive response time versus trap density at $I_0 = 1\ W/cm^2$, assuming $\mu = 0.1\ cm^2V^{-1}sec^{-1}$, $\gamma_R = 5 \times 10^{-8}\ cm^3/sec$, $s = 1.6 \times 10^{-19}\ cm^2$, $N_D = 10^{19}\ cm^{-3}$, and $\lambda_g = 5.0\ \mu m$.

time was not observed. Although Γ decreased as expected when the crystal was heated in a reducing atmosphere, the time constant remained unchanged at a typical value of 100 msec at $1W/cm^2$ irradiance, regardless of the oxidation state of the crystal. Thus, the changes in the photorefractive properties of the Ce-doped SBN:60 could not be due to variations in the trap number density, but rather to some other phenomena in the crystal manifested by the oxidation and reduction treatments.

In order to investigate these other effects an undoped SBN:60 sample was highly reduced by heating in a vacuum. The resultant crystal was very deep blue in color. Its spectrum is given in Figure 5.17 which shows significant absorption in the red, possible due to an absorption band centered in the infrared. Furthermore, the crystal was semiconducting. Although, normally, the resistivity of the SBN:60 crystal is greater than 10^{12} Ωcm, values less than 10^{5} Ωcm were measured in this reduced sample.

These effects were attributed to the formation of F centers in the crystal as a result of the reduction treatment. Rather than reducing the valence state of a multivalent dopant, such as Fe, the excess electrons left over in the crystal by the removal of oxygen are captured and trapped by an oxygen vacancy. The F centers can then act as donors of electrons with ionization energies dependent on whether one or two electrons are trapped. The energy levels are thought to be quite shallow - 0.025eV for V_0 with two trapped

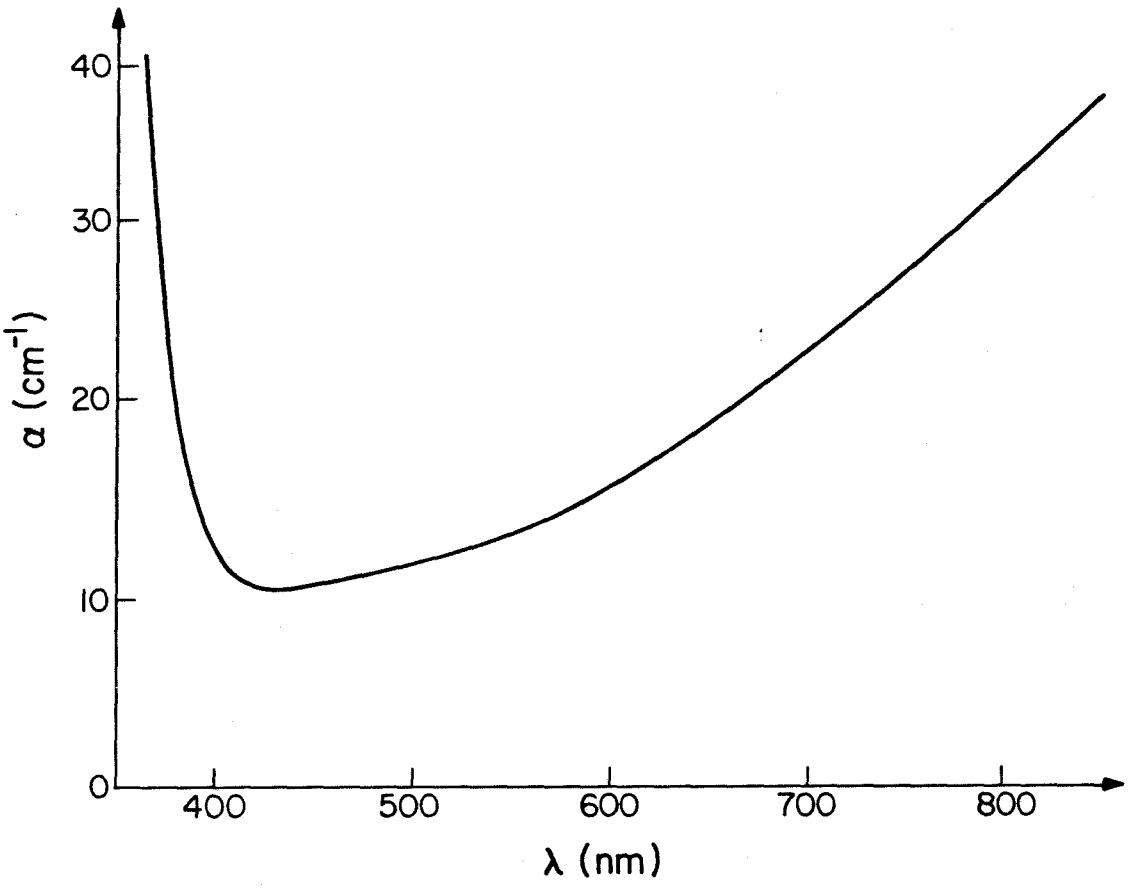

Figure 5.17. Absorption spectrum of reduced undoped SBN:60.

and 0.2eV for V_0 with one trapped electron[15]. At room temperature the oxygen vacancies are singly ionized, thus explaining the increased dark conductivity of the reduced crystal.

In order to further substantiate this claim, the resistivity of the sample was measured as a function of temperature so that the second ionization energy of the F centers could be determined and compared with theory. The experimental points are shown in Figure 5.18 along with a curve of the form $\exp(E_i/k_BT)$ that was fit to the data. A value of 0.27eV was found for E_i, in agreement with the expected value of 0.2eV.

The anomalous behavior of the photorefractive properties of Ce-doped SBN:60 on the oxidation state was, therefore, attributed to the formation of oxygen vacancies and their subsequent effect on the dark conductivity of the crystal. The decrease in Γ with reduction was the result of an increase in the dark conductivity of the crystal which would reduce the overall magnitude of any internally generated space charge fields. Since the refractive index change is directly proportional to these space charge fields, a decrease in the two-beam coupling coefficient Γ followed immediately.

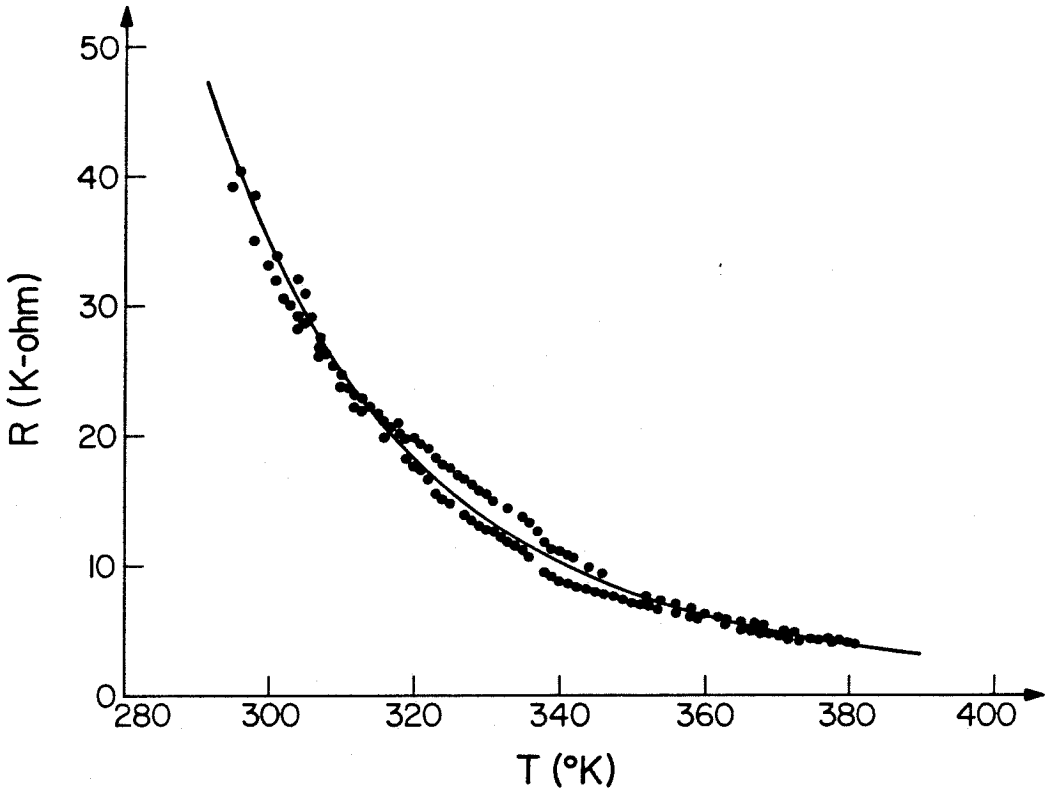

Figure 5.18. Resistance versus temperature of reduced undoped SBN:60.

5.7 Dependence of τ on the Mobility, the Two-body Recombination Rate, and the Photoionization Cross Section

Figures 5.19, 5.20, and 5.21 show the theoretical dependencies of the photorefractive response time τ of the heavily cerium-doped SBN:60 crystal on the electron mobility μ, the two-body recombination rate γ_R, and the photoionization cross section s, respectively. Since the two-beam coupling coefficient does not depend on these parameters, changes in the speed of response of a photorefractive crystal can be made independently of Γ. However, these three qualities are not easily controlled in practice.

Figure 5.19 indicates that the response τ time should decrease with increasing carrier mobility. Since μ is predominantly an intrinsic quantity of the host crystal, little can be done to increase its value other than eliminating unnecessary scattering centers from the crystal by the use of purer starting materials during the crystal growth.

However, s and γ_R are extrinsic parameters that depend on the dopant properties. If a different dopant is chosen that has either a larger photoionization cross section or a smaller two-body recombination rate coefficient than that of cerium, then, according to Figures 5.20 and 5.21, the resulting doped sample of SBN:60 should have a shorter response time. The selection of such a dopant, unfortunately, is a nontrivial task.

Although the dependence of τ on mobility is as expected,

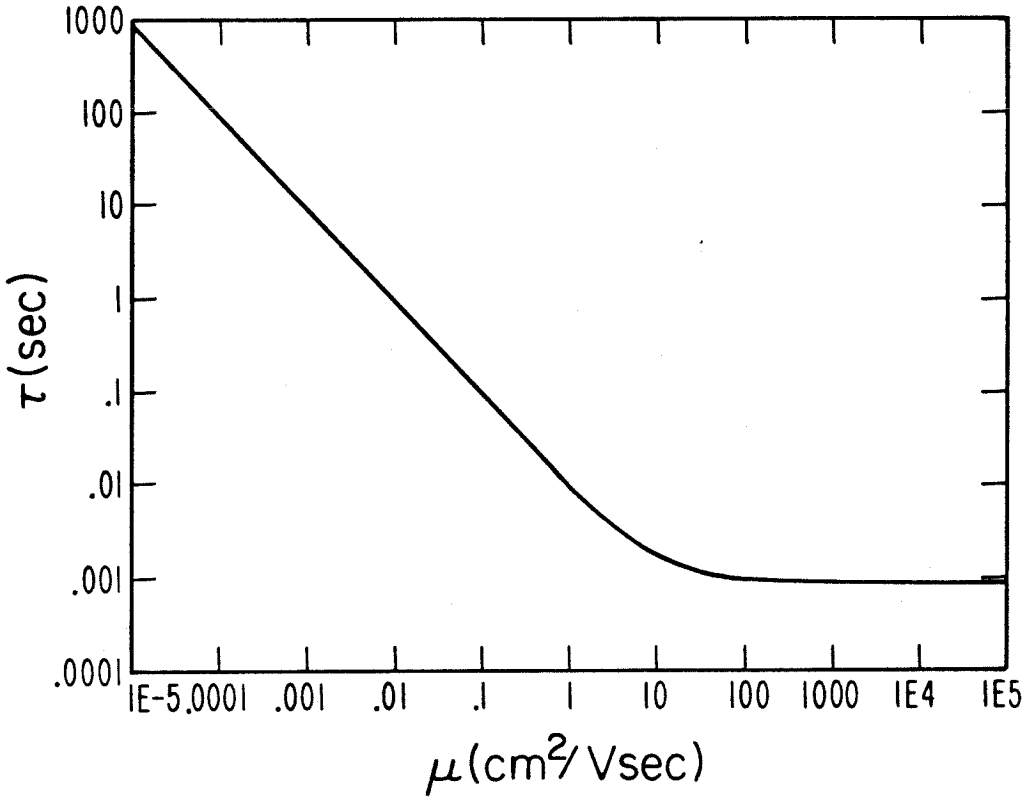

Figure 5.19. Photorefractive response time versus mobility at I_0 = 1 W/cm^2, assuming $N_A = 10^{16}$ cm^{-3}, $\gamma_R = 5 \times 10^{-8}$ cm^3/sec, s = 1.6×10^{-19} cm^2, $N_D = 10^{19}$ cm^{-3}, and λ_g = 5 μm.

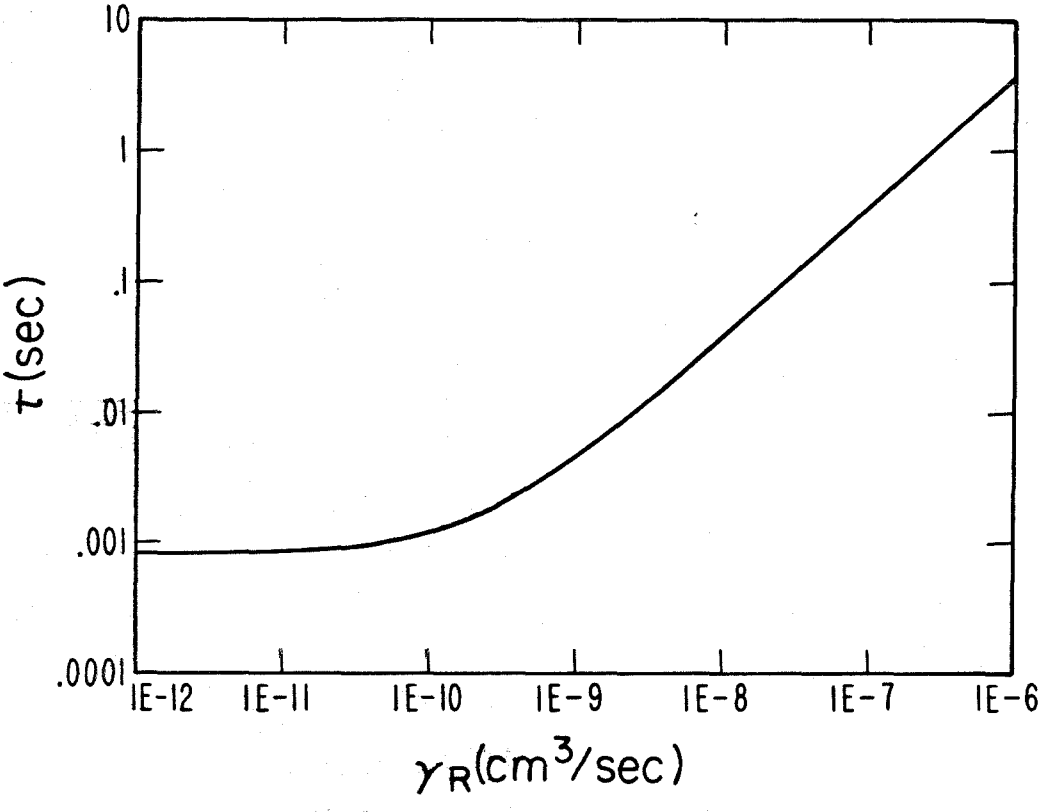

Figure 5.20. Photorefractive response time versus two-body recombination rate coefficient at I_0 = 1 W/cm^2, assuming $N_A = 10^{16}$ cm^{-3}, μ = 0.1 cm^{2}V^{-1}sec^{-1}, s = 1.6 X 10^{-19} cm^2, $N_D = 10^{19}$ cm^{-3}, and λ_g = 5.0 μm.

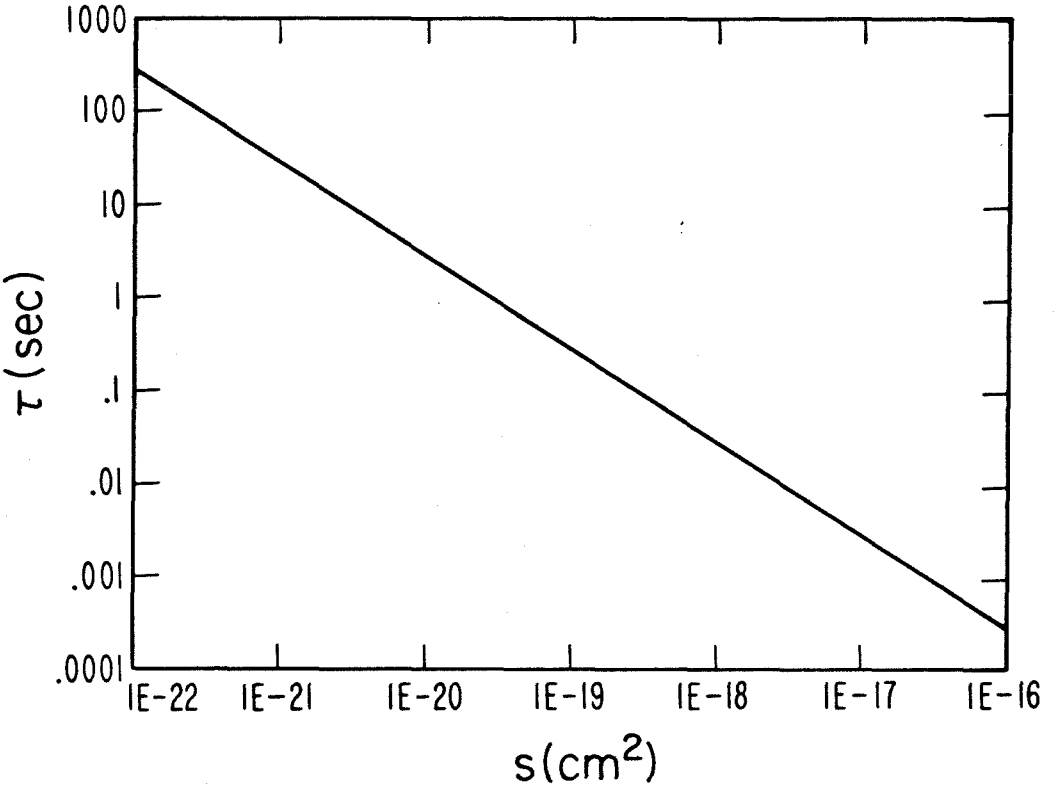

Figure 5.21. Photorefractive response time versus photoionization cross section at I_0 = 1 W/cm^2, assuming $N_A = 10^{16}$ cm^{-3}, μ = 0.1 cm^2 V^{-1}sec^{-1}, $\gamma_R = 5 \times 10^{-8}$ cm^3/sec, $N_D = 10^{19}$ cm^{-3}, and λ_g = 5 μm.

the effects of s and γ_R on τ may not be intuitively obvious. If the photoionization cross section is considered to be a measure of the quantum efficiency of the donors, then the decrease in τ with increasing s is plausible. However, if the two-body recombination rate coefficient is taken as a measure of the capture cross section of the traps, then an immediate response may suggest that traps with large γ_R are desirable. This is not the case since the ultimate goal is to transport charges a distance on the order of microns, which is some one hundred times the average spacing between neighboring traps. In a crystal characterized by a large γ_R, charges would recombine with traps before traveling the full distance. Thus, multiple photoexcitations would be needed to transport a single charge the required distance. Hence, traps with small values of γ_R are preferred since less photons per charge are necessary to obtain the same results.

5.8 Dependence of Γ and τ on Optical Wavelength

Consider the two-beam coupling coefficient Γ given by Eqs. [2.18], [3.7], and [3.8]. It is proportional to the optical frequency ω and to the first order component of the space charge field, E_1. For small grating periods $E_d >> E_q$ and $E_1 \approx E_q$, while for large grating periods, $E_q >> E_d$ and $E_1 \approx E_d$. Although $E_d = k_B T k/e$ is independent of the optical wavelength λ, $E_q = eN_A^C[1+N_A^C/(N_{Ce}-N_A^C)]^{-1}/\varepsilon k$ does indeed depend on λ though the term $(N_{Ce}-N_A^C)$ which is number density of donors in the

dark that are photoionizable by the wavelength of light in question. Therefore, the two-beam coupling coefficient can be given by

$$\Gamma = \lambda^{-1}[1+N_A^C/(N_{Ce}-N_A^C)]^{-1}\Gamma^{(1)} \text{ for small } \lambda_g, \quad [5.12a]$$

and

$$\Gamma = \lambda^{-1}\Gamma^{(2)} \text{ for large } \lambda_g, \quad [5.12b]$$

where the relation $\omega=2\pi c/\lambda$ was used, and where the constants $\Gamma^{(1)}$ and $\Gamma^{(2)}$ are defined by $\Gamma^{(1)}=\lambda[1+N_A^C/(N_{Ce}-N_A^C)]\Gamma$ and $\Gamma^{(2)}=\lambda\Gamma$.

Similarly, from Eqs. [2.22] and [2.23] the photorefractive response time can be written as

$$\tau=[S_e^C(N_{Ce}-N_A^C)\lambda]^{-1}\ \tau^{(1)} \quad [5.13]$$

where $\tau^{(1)}$ is defined by $\tau^{(1)}=S_e^C(N_{Ce}-N_A^C)\lambda\tau$. Assuming that the optical absorption within the bandap of the crystal is due solely to the photoionization of photorefractive sites, then $S_e^C(N_{Ce}-N_A^C)=\alpha$, the absorption coefficient, and the expression for τ becomes

$$\tau=(\alpha\lambda)^{-1}\tau^{(1)} \quad [5.14]$$

Figures 5.22 and 5.23 show the results of the two-beam coupling experiments performed on the $BaTiO_3$ crystal with an argon-ion laser, an R6G dye laser, a He-Ne laser, and a GaAlAs semiconductor laser. The direction of the grating wavevector remained constant throughout the experiments. The theoretical curves were obtained from equations [5.12b] and [5.14] by choosing appropriate values for $\Gamma^{(2)}$ and $\tau^{(1)}$ in

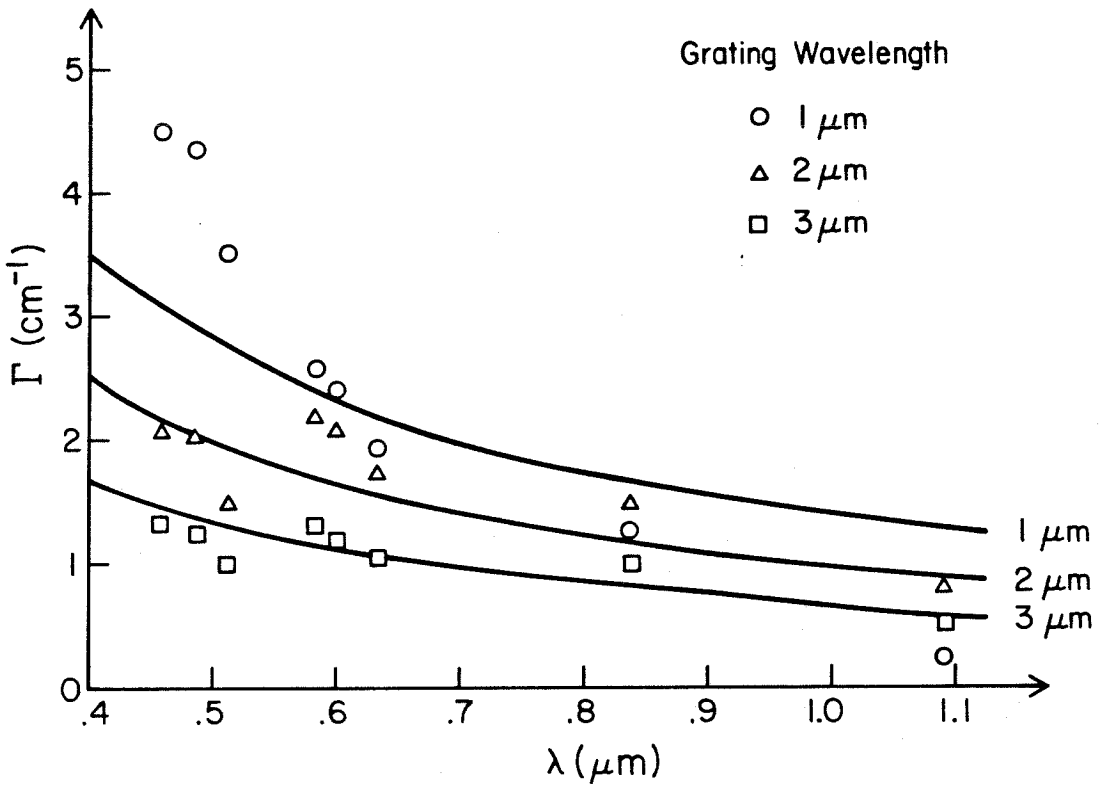

Figure 5.22. Two-beam coupling coefficient versus optical wavelength for $BaTiO_3$.

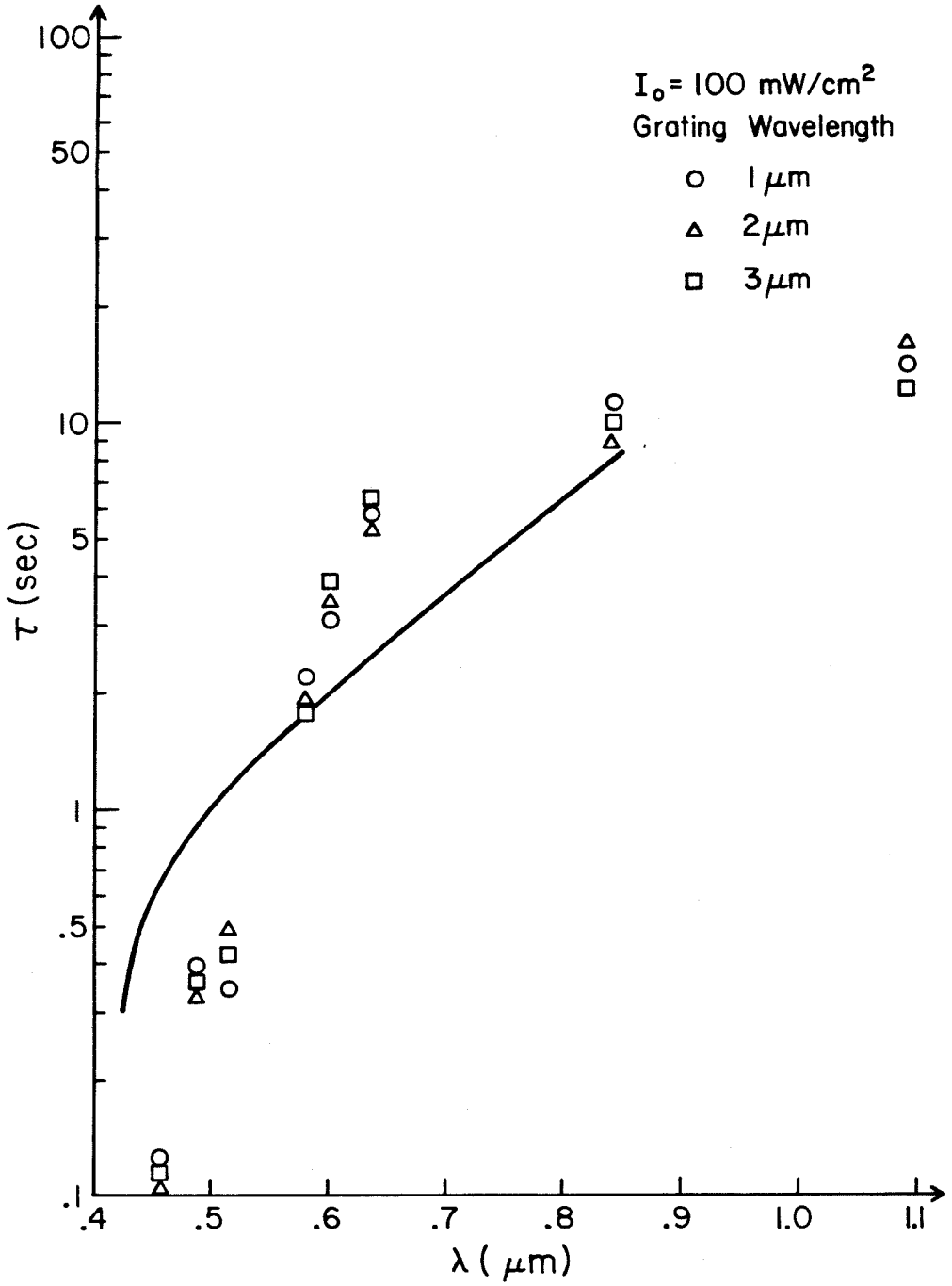

Figure 5.23. Photorefractive response time versus optical wavelength for $BaTiO_3$.

each case.

The data in Figures 5.22 and 5.23 indicate that $BaTiO_3$ is photorefractive throughout the visible and into the near infrared. For grating wavelengths greater than 1μm, the two-beam coupling coefficient is only a factor of 2 or 3 less at 1.09μm than it is at 0.45μm. As expected, the curves for Γ are seen to fit the experimental data best at the longer grating periods.

The response time of barium titanate, however, is significantly more wavelength dependent than Γ. In fact, throughout this wavelength domain, τ varies by two orders of magnitude; from 100 msec at 0.45μm to greater than 10 sec at 1.09μm for $I_0=100mW/cm^2$. Also, the dependence of τ on grating wavelength is apparently quite weak in the range from 1μm to 3μm. The theoretical variation of τ with λ was obtained from the absorption spectrum of $BaTiO_3$ given in Figure 4.3 and is seen to fit the experimental points only to within a factor of 3 or 4. This implies that there is still significant wavelength dependence in the $\tau^{(1)}$ term. Furthermore, the assumption that led to the expression $\alpha=S_e^C(N_{Ce}-N_A^C)$ is certainly not entirely valid since not all optical absorption will necessarily contribute to the photorefractive process.

The near infrared photorefractive properties of the tungsten bronze ferroelectrics are shown in Figures 5.24 to 5.27. At 0.84μm all of the crystals were photorefractive with responses comparable to that of $BaTiO_3$. As expected the

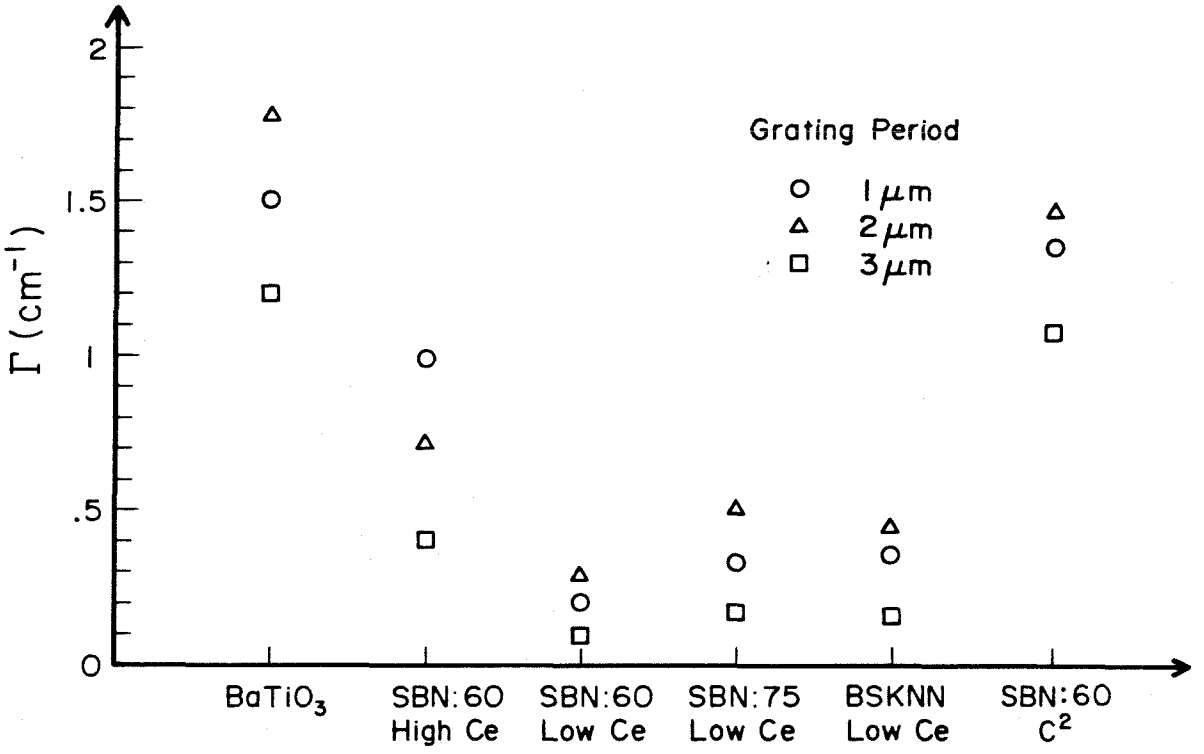

Figure 5.24. Two-beam coupling coefficients of the crystals at λ = 0.84 μm.

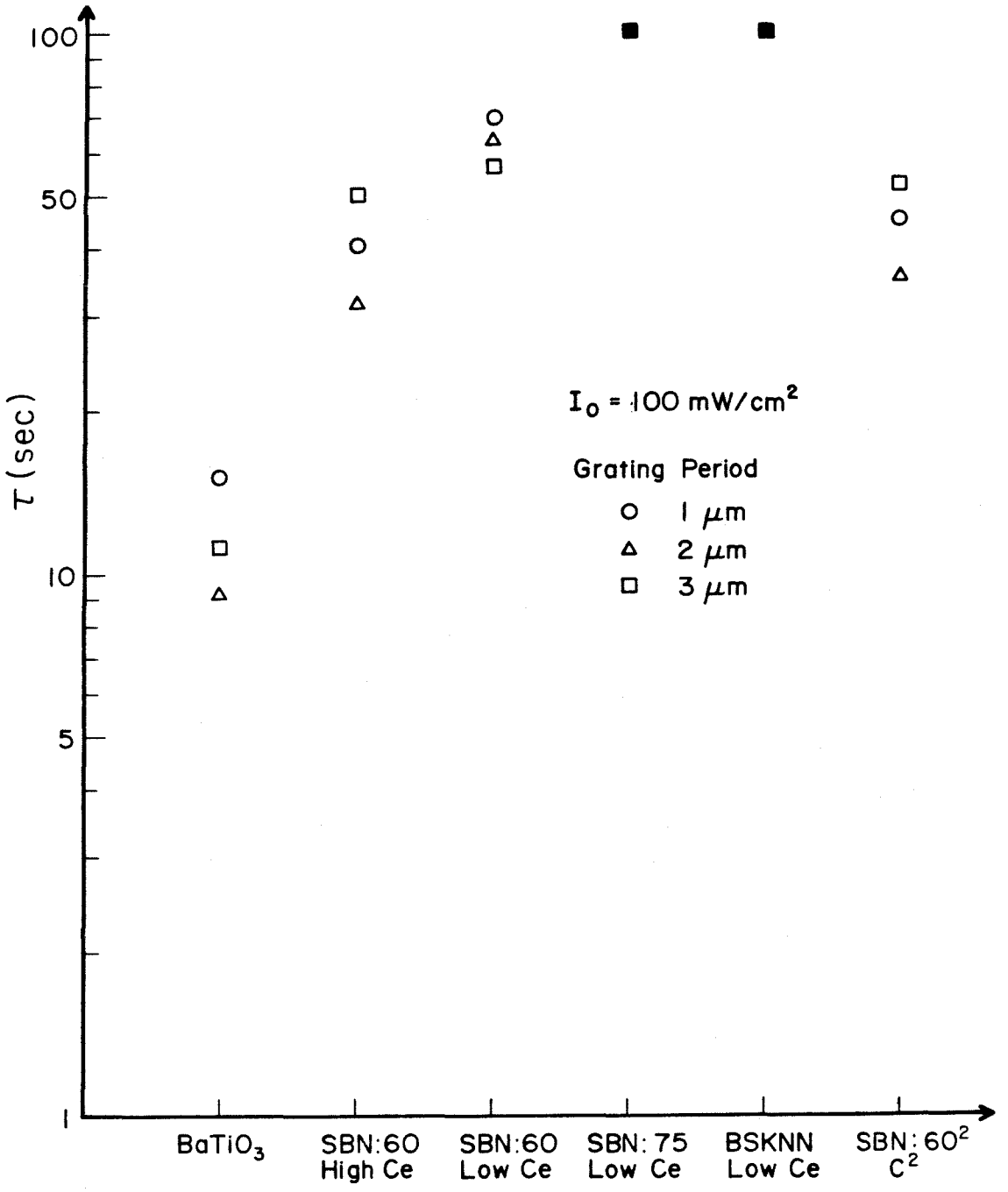

Figure 5.25. Photorefractive response times of the crystals for λ = 0.84 μm.

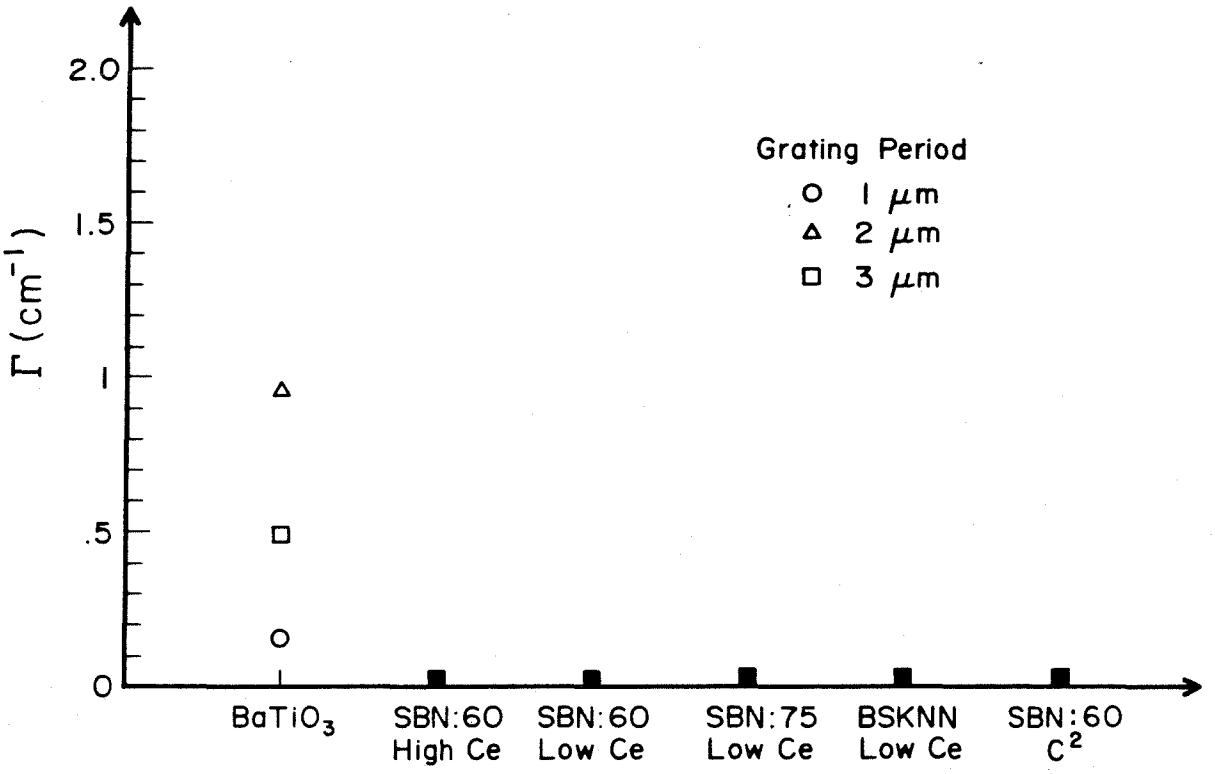

Figure 5.26. Two-beam coupling coefficients of the crystals for λ = 1.09 μm.

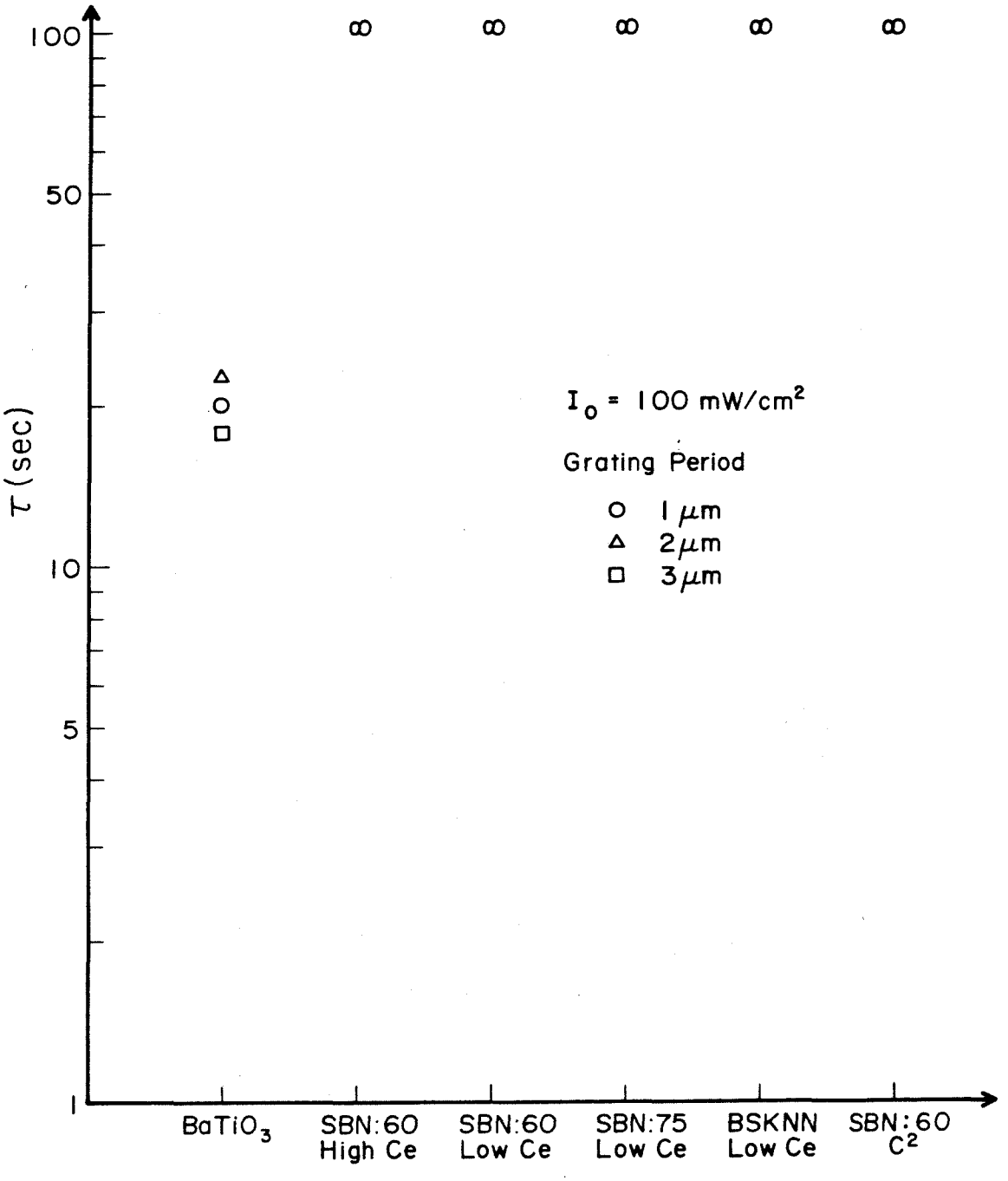

Figure 5.27. Photorefractive response times of the crystals for λ = 1.09 μm.

doubly-doped SBN:60 crystal did exhibit enhanced photorefractive properties in the near infrared due presumably to the absorption band centered in the red near 0.65μm (see Fig. 4.9). However, at 1.09μm, none of the tungsten bronzes displayed a photorefractive effect, unlike the barium titanate sample. A cutoff must, therefore, exist in these crystals between 0.84μm and 1.09μm. This implies that the energy levels created by the cerium impurities in the tungsten bronze ferroelectrics must necessarily lie deeper in the bandap than those formed by iron in barium titanate.

5.9 Dependence of Γ and τ on Temperature

Although an obvious temperature dependence exists in the expressions for the two-beam coupling coefficient Γ and the photorefractive response time τ through the characteristic field $E_d=k_BTk/e$ (see Eqs.[2.18], [2.22], and [3.7]), such an effect would be quite weak over a limited temperature range. Much larger temperature effects should exist near the phase transitions of the crystals due to dramatic changes in both the electrooptic coefficients of the materials and their dielectric constants. In barium titanate this temperature dependence should be greatest near its tetragonal to orthorhombic phase transition at 5^oC[23], while in SBN:60 this effect should be largest near its tetragonal to cubic phase transition[24] at 72^oC.

These predictions can be justified by examining the expressions of Γ and τ in the limit of large grating spacings

where $E_d << E_q$. In this case it follows from Eqs. [2.18], [2.22], and [3.7] that

$$\Gamma \alpha r E_d \alpha r \qquad [5.15]$$

and

$$\tau \alpha E_q^{-1}(E_d+E_\mu) \alpha \varepsilon. \qquad [5.16]$$

Thus, as the temperature of the crystal approaches that of the phase transition, both the two-beam coupling coefficient and the photorefractive response time should, therefore, increase. Although the effect is not as pronounced at shorter grating spacings, it still does exist[25].

These results were experimentally investigated by examining the temperature dependence of the fanning effect in $BaTiO_3$ and cerium-doped SBN:60. When an extraordinarily polarized laser beam passes through a photorefractive crystal, two-beam coupling causes light scattered from crystal to be amplified into a broad fan[26]. This effect is sufficiently strong to be used as an optical limiting mechanism[27]. Figure 5.28 is a plot versus temperature of the power T transmitted through the optical limiter at steady state normalized by the power transmitted before the buildup of any holographic gratings. Also shown as a function of temperature is the intensity normalized response time. The angle between the incident beam and the crystal c-axis was 49° measured outside the crystal. Temperature control was achieved by immersing the sample in an oil filled cuvette mounted on a thermoelectrically cooled copper block. As expected, between $10^\circ C$ and $60^\circ C$ the response time decreased

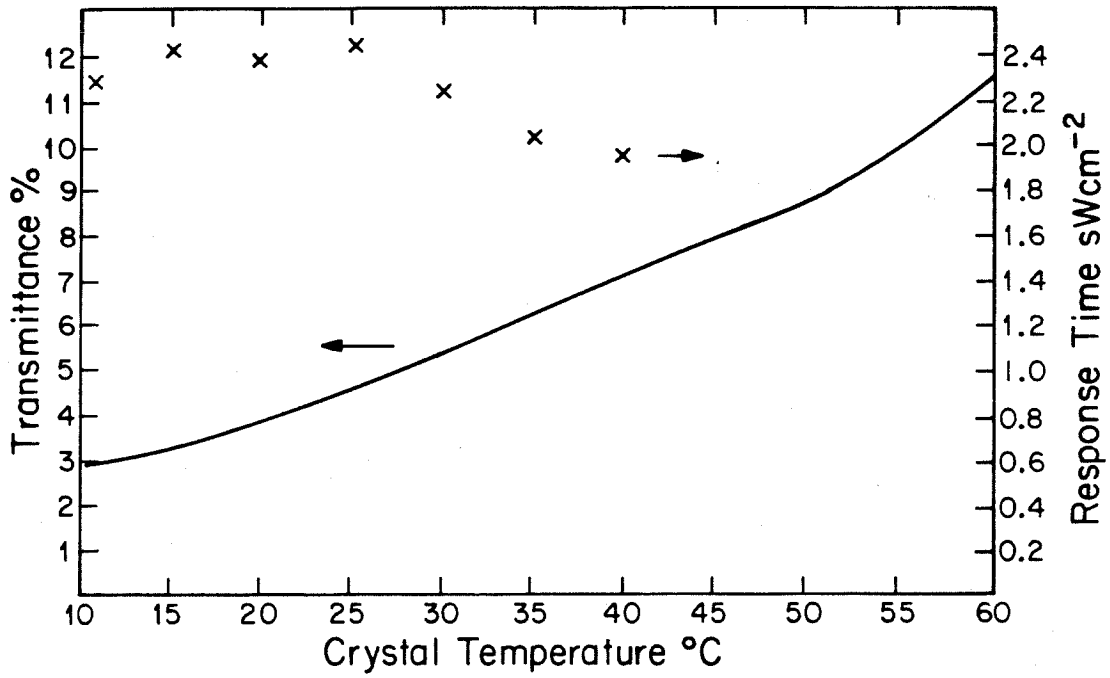

Figure 5.28. Temperature dependence and speed of response of the fanning limiter in $BaTiO_3$.

slightly while the transmissivity increased from 3% to 11.5% which corresponded to a decrease in the two-beam coupling coefficient.

Figure 5.29 is a plot of steady state transmissivity versus temperature for the heavily Ce-doped SBN:60 crystal. As the theory predicted, the efficiency of the limiter became larger as the temperature was increased towards the tetragonal to cubic phase transition. However, the efficiency increase, as well as the overall efficiency, was much smaller than for barium titanate.

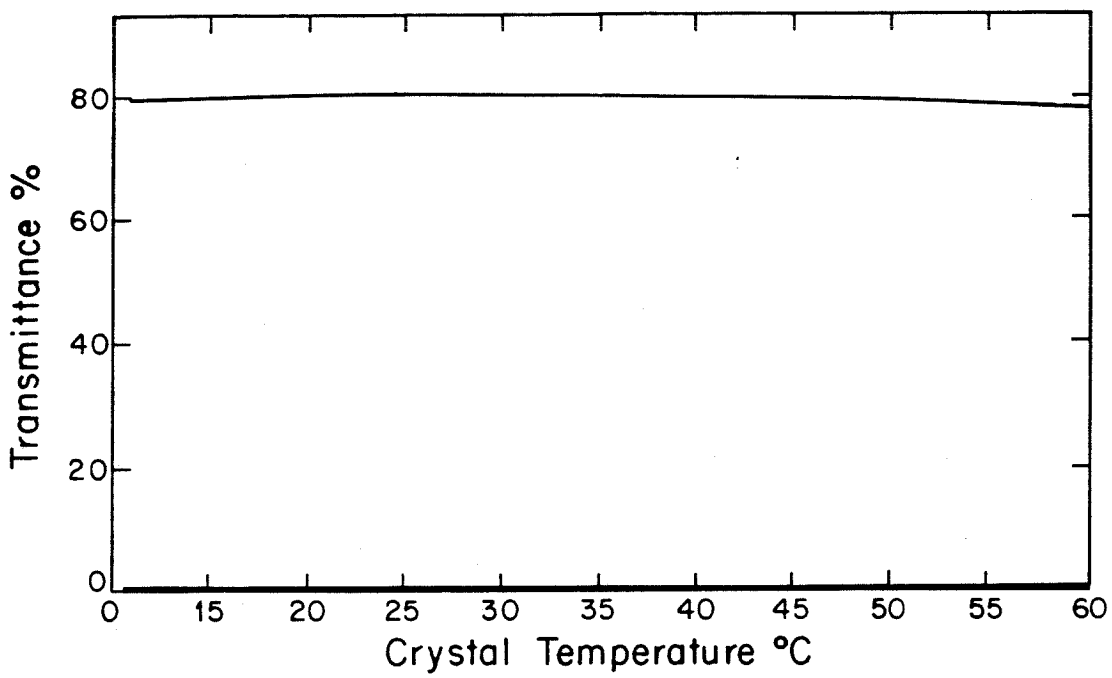

Figure 5.29. Temperature dependence of the transmittance of the fanning limiter in heavily Ce-doped SBN:60.

5.10 References

1. See, for example, A. Yariv, Quantum Electronics, (Wiley, New York, 1975).

2. J. Feinberg, D. Heiman, A. R. Tanguay, Jr., and R. W. Hellwarth, J. Appl. Phys. 51, 1297 (1980).

3. J. O. White, M. Cronin-Golomb, B. Fisher, and A. Yariv, Appl. Phys. Lett. 40, 450 (1982).

4. J. Feinberg and R. W. Hellwarth, Opt. Lett. 5, 519 (1980).

5. Nuclear Activation Services Limited, Hami Hon, Ontario, Canada L8S 4K1.

6. W. Phillips, J. J. Amodei, and D. L. Staebler, RCA Rev. 33, 94 (1972).

7. M. B. Klein and R. N. Schwartz, J. Opt. Soc. Am. B 3, 293 (1986).

8. See, for example, Table 4.1 and I. P. Kaminow and E. H. Turner, Handbook of Lasers with Selected Data on Optical Technology, the Chemical Rubber Co., 447 (1971).

9. G. C. Valley and M. B. Klein, Opt. Eng. 22, 704 (1983).

10. E. V. Bursian, Ya. G. Girshberg, and A. V. Ruzhnikov, Phys. Stat. Sol. (b), 74, 689 (1976).

11. G. A. Cox and R. M. Tredgold, Phys. Lett. 11, 22 (1964).

12. L. K. Lam, T. Y. Chang, J. Feinberg and R. W. Hellwarth, Opt. Lett. 6, 475 (1981).

13. S. Ducharme and J. Feinberg, J. Opt. Soc. Am. B, 3, 283 (1986).

14. M. B. Klein and G. C. Valley, J. Appl. Phys. 57, 4901 (1985).

15. C. N. Berglund and H. J. Braun, Phys. Rev. 164, 790 (1967).

16. N. H. Chan, R. K. Sharma, and D. M. Smyth, J. Am. Chem. Soc. 64, 556 (1981).

17. J. Daniels, Philips Res. Rep. 31, 505 (1976).

18. S. Ikegami and I. Ueda, J. Phys. Soc. Jpn. 19, 159 (1964).

19. C. N. Berglund and W. S. Baer, Phys. Rev. 157, 358 (1967).

20. F. D. Ho, Phys. Stat. Sol. (a), 66, 793 (1981).

21. K. L. Sweeney and L. E. Halliburton, Appl. Phys. Lett. 43, 336 (1983).

22. G. A. Rakuljic, A. Yariv, and R. R. Neurgaonkas, Proc. SPIE 613, 110 (1986).

23. A. R. Johnston and J. M. Weingart, J. Opt. Soc. Am. 55, 828 (1965).

24. A. J. Fox, J. Appl. Phys. 44, 254 (1973).

25. M. Cronin-Golomb, G. A. Rakuljic, and A. Yariv, Proc. SPIE 613, 106 (1986).

26. V. V. Voronov, I. R. Dorosh, Yu. S. Kuz'minov, and N. V. Tkachenko, Sov. J. Quantum Electron. 10, 1346 (1980).

27. M. Cronin-Golomb and A. Yariv, J. Appl. Phys. 57, 4906 (1985).

6. COMPARISON OF PHOTOREFRACTIVE CRYSTALS

Photorefractive crystals are promising materials for optical data processing applications. A large number of parallel operations can be processed in a single crystal. Photorefractive materials can store optical holograms for time durations of hours to years, depending on the dark conductivity. Optical amplifiers with gain factors of 4000 have been constructed[1], and phase conjugate reflectivities greater than 20 have been observed in $BaTiO_3$ with four-wave mixing[2]. Operation on nanosecond time scales has been demonstrated[3-5] with Q-switched pulses from doubled Nd:YAG lasers. Finally, the requirements on write and erase energy density in photorefractive crystals such as BSO[6] are comparable to the best photographic plates.

There are two major factors that limit widespread application of photorefractive materials at present. First, some of the promising crystals such as $BaTiO_3$, SBN, and $KNbO_3$ are not widely available in large samples with high optical quality. Second, the crystals that are available are not optimal in all respects. For instance, in order to demonstrate high speed, low write energy, long memory, or large gain, it is necessary to use several different types of materials. The purpose of this chapter is, therefore, to compare photorefractive materials including $BaTiO_3$, SBN, and BSKNN on the basis of several figures of merit which are introduced in the next section. Both ferroelectric and

non-ferroelectric materials will be considered in the comparison.

6.1 Figures of Merit

6.1.1 Steady-state index change

The steady-state change in the refractive index is defined as the index change reached after illumination for a time that is long compared to the photorefractive response time τ. The index change is related directly to the space charge field through

$$\Delta n_{ss} = \frac{1}{2} n_b^3 r_{eff} E_{sc}, \qquad [6.1]$$

where n_b is the background refractive index, r_{eff} is the effective electrooptic coefficient, and E_{sc} is the internally generated space charge electric field. The steady-state index change is also related to the two-beam coupling coefficient Γ by

$$\begin{aligned} \Delta n_{ss} &= \Gamma c/\omega \\ &= \lambda\Gamma/2\pi, \end{aligned} \qquad [6.2]$$

where λ is the wavelength of light.

In order to determine the materials dependence of Δn_{ss}, the space charge field E_{sc} needs to be considered. Using the one species, one carrier model of Chapter 2, three limits for E_{sc} exist:

(1): $E_{sc} \simeq E_d$. From Eq. [2.18], this occurs when $E_o < E_d < E_q$ which is a common condition when no electric field is applied and the grating period is large. In this case

$$\Delta n_{ss} \propto n_b^3 r_{eff} E_d$$
$$\propto n_b^3 r_{eff} , \qquad [6.3]$$

since E_d does not depend on material parameters.

(2): $E_{sc} \simeq E_q$. This occurs when $E_q < E_d$ or E_o; that is, when a large electric field is applied or when the grating period is small. In this case

$$\Delta n_{ss} \propto n_b^3 r_{eff} E_q$$
$$\propto n_b^3 r_{eff}/\varepsilon, \qquad [6.4]$$

where ε is the dielectric constant of the material.

(3): $E_{sc} \simeq E_o$. This occurs when $E_d < E_o < E_q$ which holds in cases where moderately large electric fields are applied to the crystal. Hence,

$$\Delta n_{ss} \propto n_b^3 r_{eff} E_o$$
$$\propto n_b^3 r_{eff}. \qquad [6.5]$$

Therefore, photorefractive crystals with large values of $n_b^3 r_{eff}$ and $n_b^3 r_{eff}/\varepsilon$ are desirable for applications such as passive phase conjugation that require large steady-state index changes.

6.1.2 Response time

The photorefractive response time τ is a useful figure of merit for applications in which available energy limits the illumination time, or in which the grating must be written or erased in a set time scale. The response time scales with intensity until times as short as either the time for a charge carrier to move one grating period or the time necessary for the electrooptic effect to respond to the

Coulomb field of the displaced charge. The longer of these times is the fundamental limit. Diffusion times in semiconductors such as GaAs are known to be < 10 psec[7]. The electrooptic response time is of the order of attoseconds for the electronic component of the electrooptic coefficient, r_{eff}, and picoseconds for the ionic part. The mix of these two components varies, but the ultimate response time of a photorefractive crystal is in the picosecond range.

6.1.3 Photorefractive Sensitivity

The photorefractive sensitivity S is defined as the index change per absorbed energy per unit volume[8-11]. That is,

$$S = \frac{\Delta n}{\alpha I_0 t} . \qquad [6.6]$$

The photorefractive sensitivity is a useful figure of merit because it tells us how well a material uses a given amount of optical energy. Alternatively, it allows comparison of crystals with different absorption coefficients on an equal basis. From Eq. [2.18], Δn can be given by

$$\Delta n = \Delta n_{ss}(1-e^{-t/\tau}) , \qquad [6.7]$$

where a stationary index grating is assumed ($\Omega = 0$). For $t \ll \tau$,

$$\Delta n = \Delta n_{ss} t/\tau . \qquad [6.8]$$

Since τ is inversely proportional to αI_0, (see Eq. [2.22]), then

$$S \propto \Delta n_{ss} \frac{E_o+i(E_d+E_q)}{E_o+(E_d+E_\mu)} . \qquad [6.9]$$

Clearly, a large steady-state index change is preferred. Moreover, large mobilities and long recombination times, corresponding to small recombination rates, are generally desirable because these properties allow the carriers to diffuse or drift longer distances before they recombine, thereby reducing the drift field E_μ. In either case the photorefractive sensitivity is increased.

6.2 Summary of Material Parameters and Figures of Merit for Photorefractive Crystals

Table 6.1 summarizes the material parameters of interest for $BaTiO_3$, SBN, and BSKNN along with other photorefractive crystals, while in Table 6.2 the corresponding figures of merit are given. Included is the wavelength range in which the crystals are known to be photorefractive.

As expected the ferroelectric crystals $BaTiO_3$, SBN:60, SBN:75, BSKNN, $LiNbO_3$, and $KNbO_3$ exhibit the largest photorefractive effect due to their large $n_b^3 r_{eff}$ values. Although $n_b^3 r_{eff}/\varepsilon$ is approximately equal in all the materials, the former term apparently is more important for determining the steady state refractive index change. However, the non-ferroelectric crystals BSO, GaAs, and InP:Fe are significantly faster than the ferroelectrics. Owing primarily to their larger mobilities and their generally favorable transport properties, these materials have photorefractive response times 2 to 3 orders of magnitude smaller than those of the ferroelectric crystals.

Table 6.1. Material parameters of select photorefractive crystals.

Crystal	$n_i^3 r_{ij}$ (pm/V)	$n_i^3 r_{ij}/\epsilon_j$ (pm/V)	μ (cm^2/Vsec)	γ_R (cm^3/sec)
$BaTiO_3$	11300	4.9	0.5	5×10^{-8}
SBN:60	5100	5.8	0.5	5×10^{-8}
SBN:75	17000	5.0	0.5	5×10^{-8}
BSKNN	4600	13.2	---	---
$LiNbO_3$[10,12-15]	320	11.0	0.8	---
$KNbO_3$[16-19]	690	14.0	0.5	---
BSO[20,21]	82	1.8	0.03	2×10^{-11}
GaAs[22,23]	43	3.3	5800.0	---
InP[24]	52	4.1	>5000.0	---

Table 6.2. Figures of merit of select photorefractive crystals.

(E_0 = 0 V/cm)

Crystal	Wavelength Range (μm)	Δn_{ss}	τ for 1W/cm^2, λ	S(cm^3/J)
$BaTiO_3$	0.4-1.1	4.8×10^{-5}	50msec, 0.5μm	2.4×10^{-4}
SBN:60	0.4-0.85	3.2×10^{-5}	120msec, 0.5μm	5.3×10^{-3}
Ce-doped SBN:60	0.4-0.85	9.6×10^{-5}	80msec, 0.5μm	6.0×10^{-4}
Ce-doped SBN:75	0.4-0.85	4.0×10^{-5}	150msec, 0.5μm	3.0×10^{-4}
Ce-doped BSKNN	0.4-0.85	4.0×10^{-5}	200msec, 0.5μm	2.0×10^{-4}
$LiNbO_3$[10,12-15]	0.4-0.7	$10^{-5} - 10^{-3}$	>1sec	$5\times10^{-6} - 5\times10^{-5}$
$KNbO_3$[16-19]	0.4-0.7	5.0×10^{-5}	<100msec, 0.5μm	1.7×10^{-4}
BSO[25-27]	0.4-0.7	5.0×10^{-6}	< 1msec, 0.5μm	3×10^{-3}
GaAs[22,23]	0.8-1.8	6.4×10^{-6}	80μsec, 1.06μm	5.0×10^{-2}
InP:Fe[24]	0.85-1.3	0.2×10^{-6}	<100μsec, 1.06μm	$>2 \times 10^{-3}$

Since the photorefractive sensitivity is proportional to $\Delta n_{ss}/\tau$, these differences in the values of Δn_{ss} and τ between the non-ferroelectrics and the ferroelectrics essentially cancel, and large values of S are, therefore, possible with either type of crystal. It is interesting to note that the photorefractive sensitivity of SBN:60 is reduced by the addition of cerium although such a doped crystal exhibits improved values of Δn_{ss} and τ. This implies that not all of the optical absorption in the cerium-doped SBN:60 crystal contributes to the photorefractive effect.

Finally, the wavelength ranges given in Table 6.2 indicate that photorefractive effect in the oxides is observed only with visible or very near infrared radiation. At longer wavelengths only the semiconductors such as GaAs and InP are known to be photorefractive.

6.3 References

1. F. Laeri, T. Tschudi, and J. Albers, Opt. Commun. 47, 387 (1983).

2. J. Feinberg and R. W. Hellwarth, Opt. Lett. 5, 519 (1980).

3. C. T. Chen, D. M. Kim, and D. Von der Linde, IEEE J. Quantum Electron. QE-16, 126 (1980).

4. J. P. Hermann, J. P. Herriau, and J. P. Huignard, Appl. Opt. 20, 2173 (1981).

5. L. K. Lam, T. Y. Chang, J. Feinberg, and R. W. Hellwarth, Opt. Lett. 6, 475 (1981).

6. J. P. Huignard and J. P. Herriau, Appl. Opt. 17, 2671 (1978).

7. G. C. Valley, A. L. Smirl, M. B. Klein, K. Bohnert, and T. F. Boggess, Opt. Lett. 11, 647 (1986).

8. P. Gunter, Phys. Reports 93, 200 (1983).

9. D. Von der Linde and A. M. Glass, appl. Phys. 8, 85 (1975).

10. A. M. Glass, Opt. Eng. 17, 470 (1978).

11. E. Kratzig and R. Orlowski, Appl. Phys. 15, 133 (1978).

12. A. M. Glass, J. Electron. Mater. ^{4}, 915 (1975).

13. H. Kurz, Philips Tech. Rev. 37, 109 (1977).

14. H. Kurz, E. Kratzig, W. Keune, H. Engelmann, U. gonser, B. Dischler, and A. Rauber, Appl. Phys. 12, 355 (1977).

15. R. Orlowski, E. Kratzig, and H. Kurz, Optics Commun. 20, 171 (1977).

16. P. Gunter and A. Krumins, Appl. Phys. 23, 199 (1980).

17. P. Gunter and F. Micheron, Ferroelectrics 18, 27 (1978).

18. P. Gunter, Ferroelectrics 22, 671 (1978).

19. A. E. Krumins and P. Gunter, Phys. Stat. Sol. (a) 55, K185 (1979).

20. J. P. Huignard and F. Micheron, appl. Phys. Lett. 29, 591 (1976).

21. M. Peltier and F. Micheron, J. Appl. Phys. 48, 3683 (1977).

22. K. Tada and N. Susuki, Jpn. J. Appl. Phys. 19, 2295 (1980).

23. M. B. Klein, Opt. Lett. 9, 350 (1984).

24. A. M. Glass, A. M. Johnson, D. H. Olson, W. Simpson, and A. A. Ballman, Appl. Phys. 58, 45 (1985).

25. Ph. Refregier, L. Solymar, H. Rajenbach, and J. P. Huignard, J. Appl. Phys. 58, 45 (1985).

26. R. A. Mullen and R. W. Hellwarth, J. Appl. Phys. 58, 40 (1985).

27. S. L. Hou, R. B. Lauer, and R. E. Aldrich, J. Appl. Phys. 44, 2652 (1973).

7. APPLICATIONS OF PHOTOREFRACTIVE CRYSTALS

7.1 Optical Phase Conjugation in Nonlinear Media

Highly phototrefractive crystals such as $BaTiO_3$ and $Sr_xBa_{1-x}Nb_2O_6$ are important nonlinear materials for many of the recently developed passive (self-pumped) phase conjugate mirrors (PPCM's)[1-4]. The ability of these mirrors to correct for linear refractive index inhomogeneities has been well documented[5-7]. However, when the distorting medium is nonlinear, the distortion correction property of phase conjugate mirrors was only theoretically considered[8]. In this section the experimental compensation of a nonlinear distortion - the optical self-focusing phenomenon in photorefractive crystals - with a PPCM is described along with the corresponding theory.

This particular optical nonlinearity was chosen since the power level required for significant nonlinear effects was quite low. In fact, only a few tens of milliwatts of laser power were necessary to initiate self-focusing in a reduced sample of $Sr_{.6}Ba_{.4}Nb_2O_6$. The experimental setup used is illustrated in Figure 7.1. A photorefractive crystal was illuminated by a Gaussian laser beam at 514.5 nm from an Ar^+ laser. Due to linear absorption in the crystal, the Gaussian intensity profile will give rise to a nonuniform temperature variation which, in turn, will produce a nonuniform index profile via the thermo-optic effect. This index variation

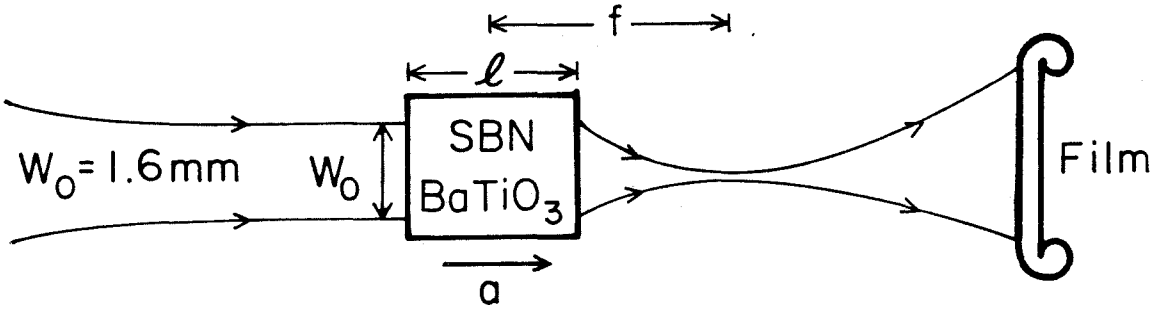

Figure 7.1. Self-focusing set-up. Photorefractive crystal is illuminated by a 514.5 nm Gaussian laser beam which is then self-focused due to crystal nonlinearities.

will then give the crystal lens-like properties which produce the self-focusing and self-diffraction effects.

Mathematically, the self-focusing effect can be attributed to a displacement vector containing nonlinear terms;

$$\bar{D} = \bar{D}\ (\text{linear}) + \bar{D}\ (\text{non-linear})$$

where

$$D_i\ (\text{linear}) = \varepsilon_{ij}E_j,$$

$$D_i\ (\text{non-linear}) = \xi_{ij}TE_j,$$

ξ_{ij} = thermo-optic coefficient,

and T = local temperature.

The refractive index is, therefore, given by

$$n_i = \left[\frac{1}{\varepsilon_0}\left(\frac{\partial D_i}{\partial \bar{E}_i}\right)\right]^{1/2} = \frac{1}{\varepsilon_0}[\varepsilon_{ii} + \xi 11^T]^{1/2} \qquad [7.1]$$

where the temperature dependence of the refractive index, which gives rise to the self-focusing effects, can be seen.

In the experiment depicted in Figure 7.1, it was found that the incident laser beam came to focus a distance f past the crystal. Figure 7.2 summarizes the results of such an experiment for several different photorefractive crystals. As one would expect, the highly reduced sample of $Sr_{.6}Ba_{.4}Nb_2O_6$ produces the greatest effect since its absorption coefficient is the largest of the samples considered.

Since the effective radius of the induced lens is on the order of the laser beam radius, the crystal should not only focus the beam, but it should modulate its phase in a manner

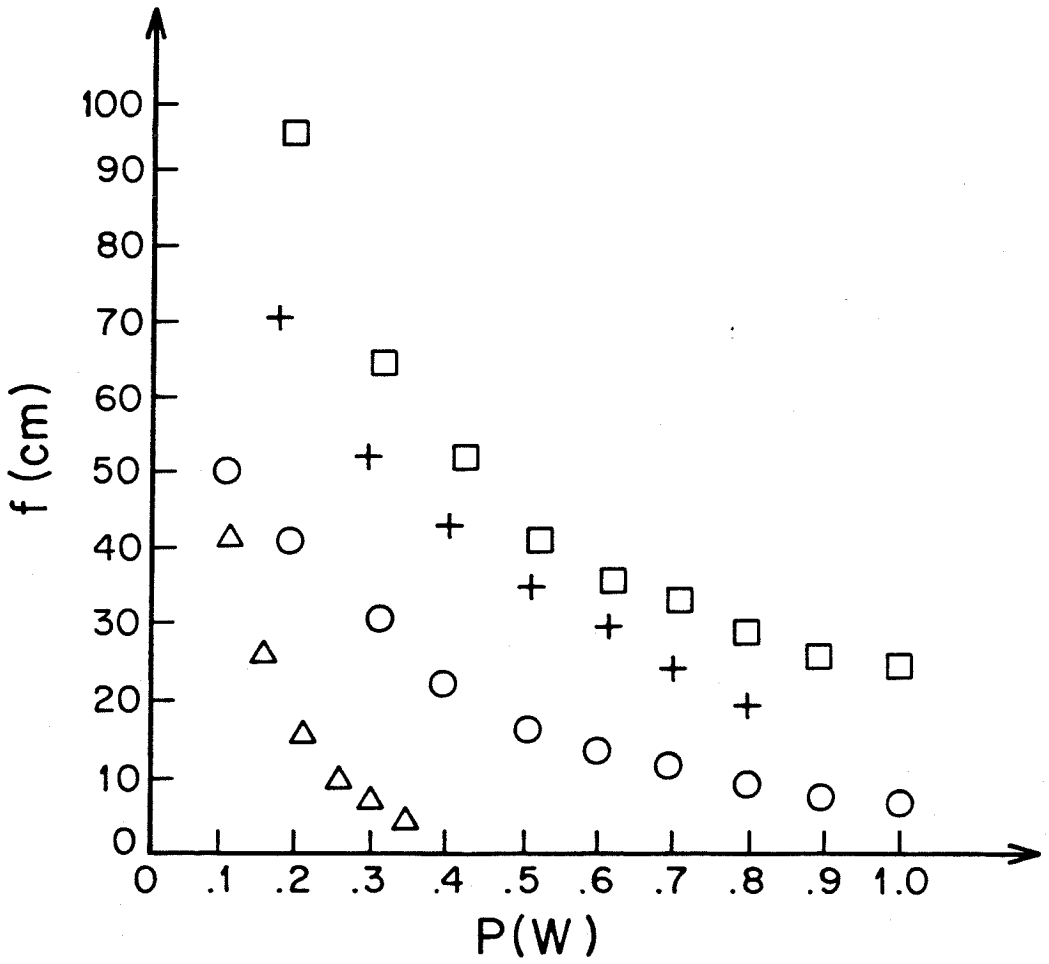

Figure 7.2. Self-focusing focal lengths f as a function of incident power P. □ = undoped SBN:60, ℓ = 0.66 cm. △ = reduced undoped SBN:60, ℓ = 0.071 cm. ○ = heavily Ce-doped SBN:60, ℓ=0.52 cm. + = $BaTiO_3$, ℓ = 0.41 cm.

that produces diffraction rings much as a lens of finite aperture would. This phenomenon is evident in Figure 7.3 which gives the intensity profiles of the transmitted beam at a position indicated by the film plane in Figure 7.1.

To analyze the nonlinear self-focusing and self-phase modulation effects and their compensation, refer to Figure 7.4 and the analysis of Pepper and Yariv[8]. Let E_1 and E_2, given by

$$E_1 = \psi(\bar{r})e^{i(\omega t-kz)} + cc \qquad [7.2]$$

$$E_2 = f(\bar{r})e^{i(\omega t+kz)} + cc, \qquad [7.3]$$

represent the fields traveling essentially in the positive and negative z-directions, respectively. The total field E is, therefore,

$$E = [\psi(\bar{r})e^{-ikz} + f(\bar{r})e^{ikz}]\, e^{i\omega t} + cc. \qquad [7.4]$$

For simplicity, assume that the nonlinear medium is isotropic. The dielectric constant responsible for the self-focusing and self-phase modulation effects will then consist (see Eq. [7.1]) of two terms; the first one describes linear, spatially dependent refractive index inhomogeneities while the second term depicts the nonlinear (temperature dependent), spatially dependent refractive index contributions. That is,

$$\varepsilon = \varepsilon_0(\bar{r}) + \varepsilon_2(\bar{r})T. \qquad [7.5]$$

Assuming that $1/\varepsilon\ d\varepsilon/dx\ \lambda << 1$, the wave equation in cgs units is given by

$$\nabla^2 E - \frac{\mu}{c^2}\,\varepsilon_0(\bar{r}) + \varepsilon_2(\bar{r})T\,\frac{\partial^2 E}{\partial t^2} = 0 \qquad [7.6]$$

Figure 7.3. Intensity profiles of the laser beam at the film plane in Figure 7.1.

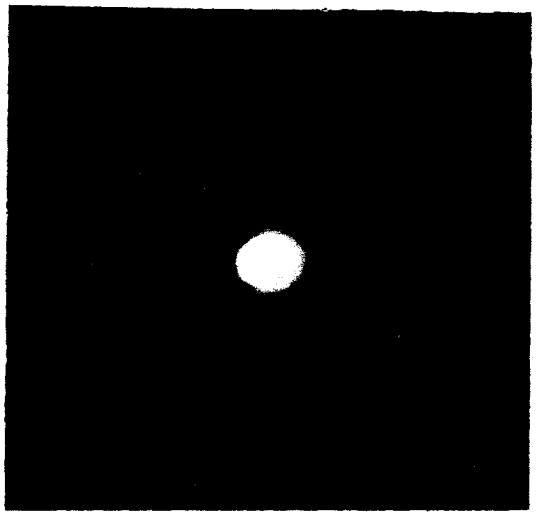

(a) $P \ll 100$ mW

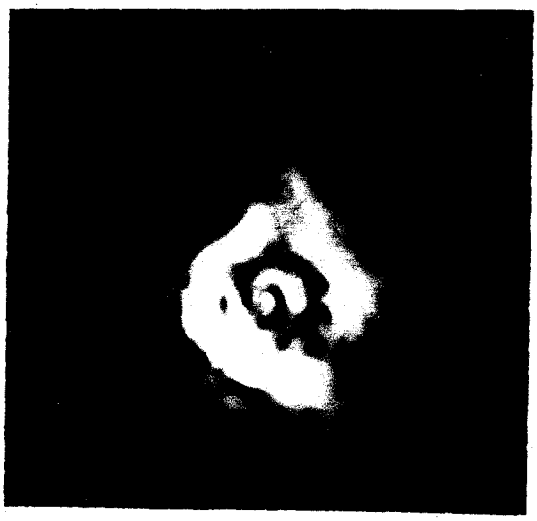

(b) $P \simeq 100$ mW

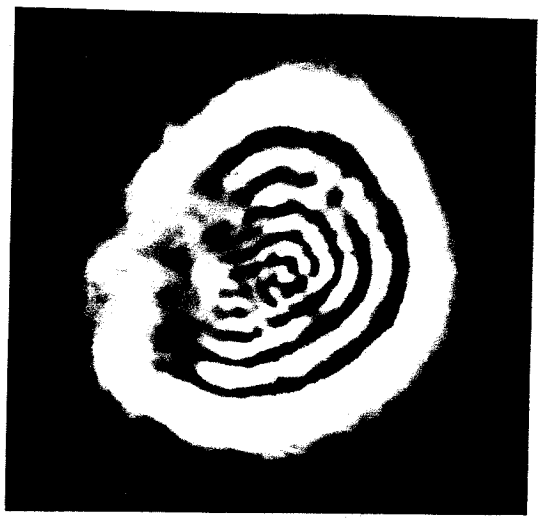

(c) $P \gg 100$ mW

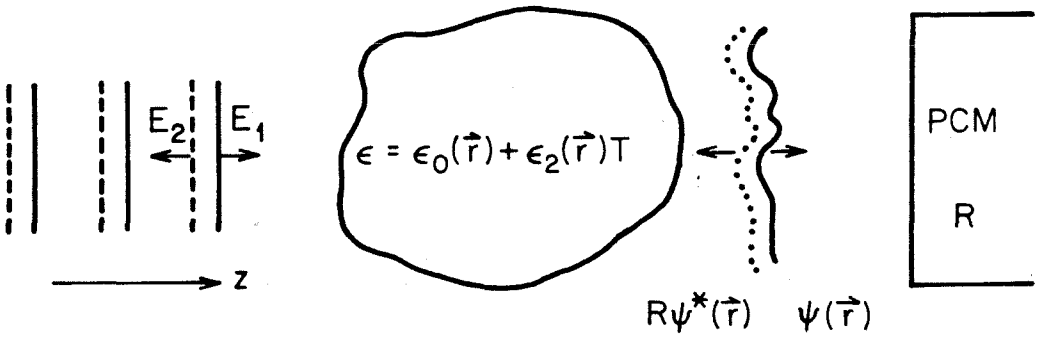

Figure 7.4. Geometry for a PCM in order to compensate for temperature dependent phase distortions. Solid (dashed) curves correspond to the incident (conjugate) equiphase surfaces.

Substituting Eq. [7.4] into Eq. [7.6] yields

$$\left\{\nabla^2\psi(\bar{r}) + \left[\frac{\omega^2\mu}{c^2}\,\varepsilon_0(\bar{r}) - k^2\right]\psi(\bar{r}) + \frac{\omega^2\mu}{c^2}\,\varepsilon_2(r)T\psi(r)\right.$$

$$\left. -2ik\,\frac{\partial\psi(\bar{r})}{\partial z}\right\} e^{-ikz} + \left\{\nabla^2 f(\bar{r})\right. \qquad [7.7]$$

$$+\left[\frac{\omega^2\mu}{c^2}\,\varepsilon_0(\bar{r}) - k^2\right] f(\bar{r}) + \frac{\omega^2\mu}{c^2}\,\varepsilon_2(\bar{r})Tf(\bar{r})$$

$$\left. + 2ik\,\frac{\partial f(\bar{r})}{\partial z}\right\} e^{ikz} = 0$$

Consider now the temperature term T. In the experiments where the nonlinear medium was a ferroelectric crystal, the temperature was not permitted to rise beyond the Curie point of the material. Also, it appeared that the thermal conductivity of the photorefractive crystals was large enough to prevent high frequency thermal gratings from forming. Hence, T was only a slowly varying function of position in these materials which, thus, did not lead to coupling of the forward ψ and backward f waves in the distorting medium.

Using this result in Eq. [7.7] and equating to zero the sum of all the terms with exp(ikz) and, separately, those of exp(-ikz) dependence leads to

$$\nabla^2\psi + \left[\frac{\omega^2\mu\varepsilon_0(\bar{r})}{c^2} - k^2\right]\psi + \frac{\omega^2\mu\varepsilon_2(\bar{r})}{c^2}\,T\psi - 2ik\,\frac{\partial\psi}{\partial z} = 0 \qquad [7.8]$$

and

$$\nabla^2 f + \left[\frac{\omega^2\mu\varepsilon_0(\bar{r})}{c^2} - k_2\right] f + \frac{\omega^2\mu\varepsilon_2(\bar{r})}{c^2}\,Tf + 2ik\,\frac{\partial f}{\partial z} = 0 \qquad [7.9]$$

Taking the complex conjugate of Eq. [7.8] yields

$$\nabla^2\psi^* + \left[\frac{\omega^2\mu\varepsilon_0(\bar{r})}{c^2} - k^2\right]\psi^* + \frac{\omega^2\mu\varepsilon_2(r)}{c^2}\,T\psi^* + 2ik\frac{\partial\psi^*}{\partial z} = 0. \quad [7.10]$$

Equations [7.9] and [7.10] indicate that $\psi^*(\bar{r})$, the conjugate amplitude of the forward wave, and the amplitude of the backward wave, $f(\bar{r})$, obey the same propagation equation. It follows immediately by a self-consistent argument that if the reflectivity of the phase conjugate mirror located at $z = z_{pcm}$, is equal to R then

$$f(\bar{r}) = R\psi^*(\bar{r})$$

for all $z<z_{pcm}$. In other words, the reflected field is proportional to the complex conjugate of the incident field everywhere in the distorting medium and outside it. At the input plane, then, the wave is healed of any distortion caused by the propagation through the distorting nonlinear medium.

The experimental arrangement used to investigate the effect is depicted in Figure 7.5. A Gaussian laser beam is self-focused by a photorefractive crystal onto a self-pumped phase conjugate mirror composed of a concave mirror and another photorefractive crystal which did not self-focus at the power levels used in this experiment. This "semi-linear" mirror[1] redirects the light back into the distorting medium which is then projected onto a film plate by the beam-splitter. Figure 7.6(a) shows the profile of the original laser beam while Figure 7.6(b) displays the distorted beam. The reflectivity of the PPCM is ≈30%. Figure 7.6(c) is a

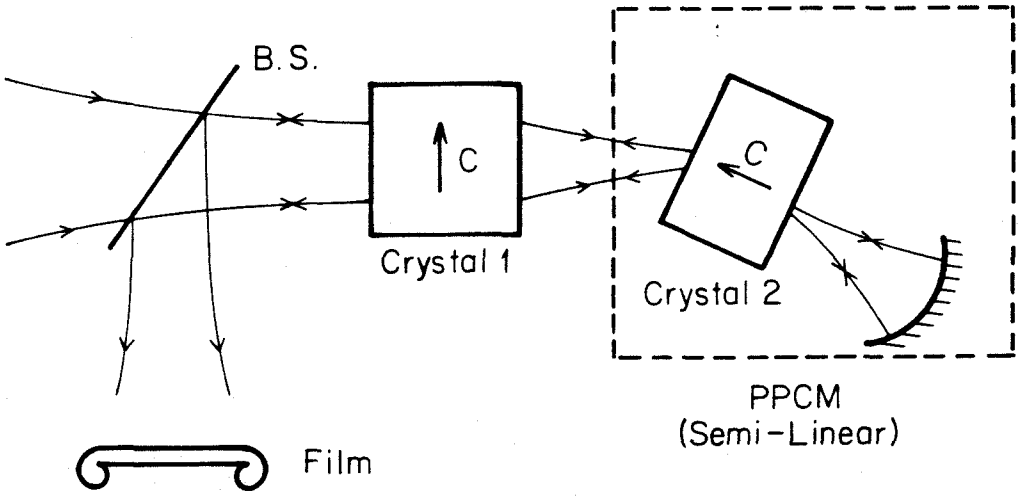

Figure 7.5. Experimental equivalent of Figure 7.4. Crystal 1 provides the nonlinear distortion while crystal 2 and the concave mirror form a PPCM. The conjugate beam is directed to the film plane by beamsplitter BS.

Figure 7.6. Intensity profiles of the beams in Figure 7.5.

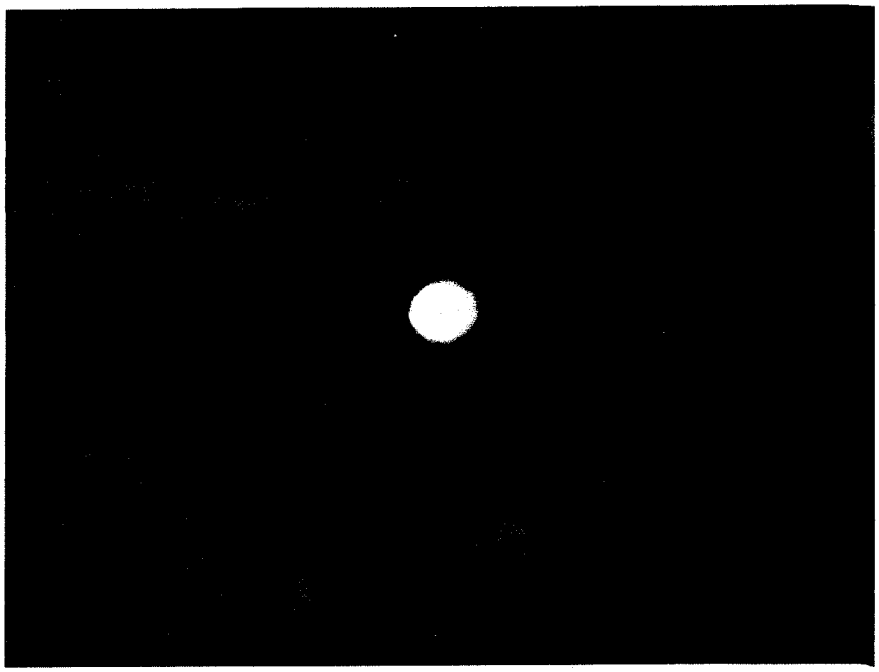

(a) Original Gaussian beam.

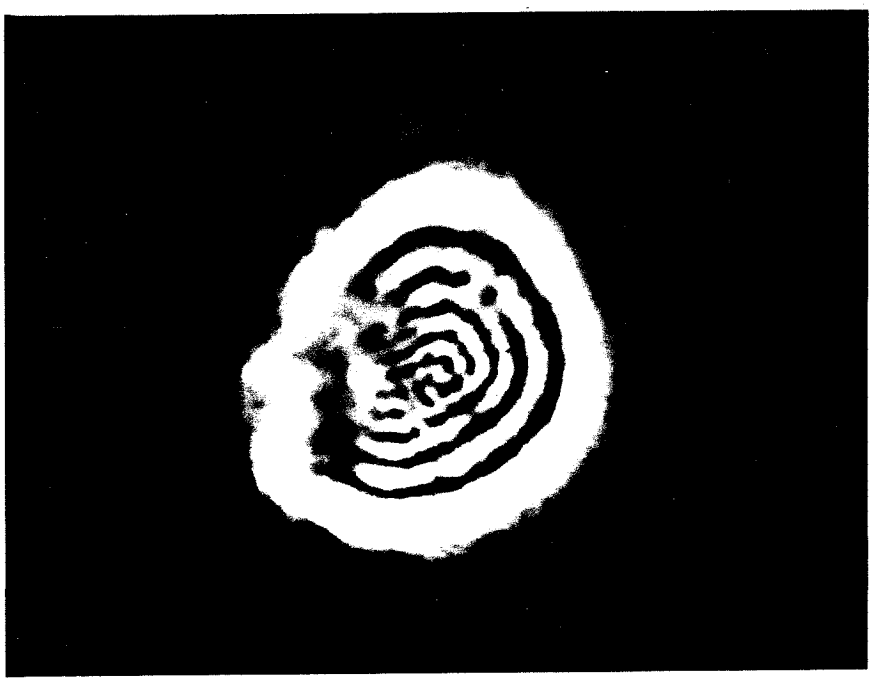

(b) Distorted beam due to self-focusing in crystal 1.

Figure 7.6. (Continued)

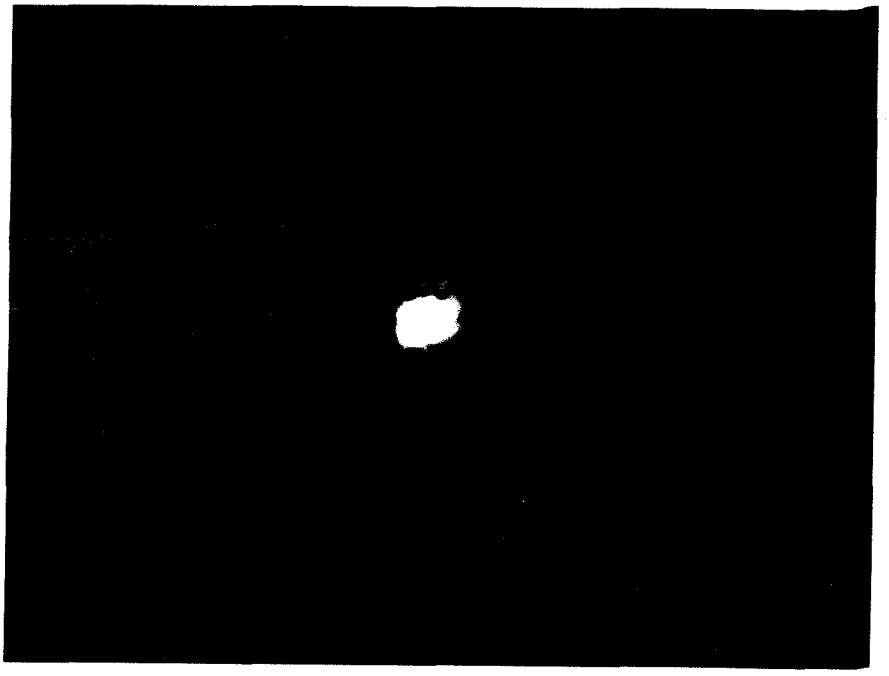

(c) Phase-conjugate or corrected beam after passing back through the distortion.

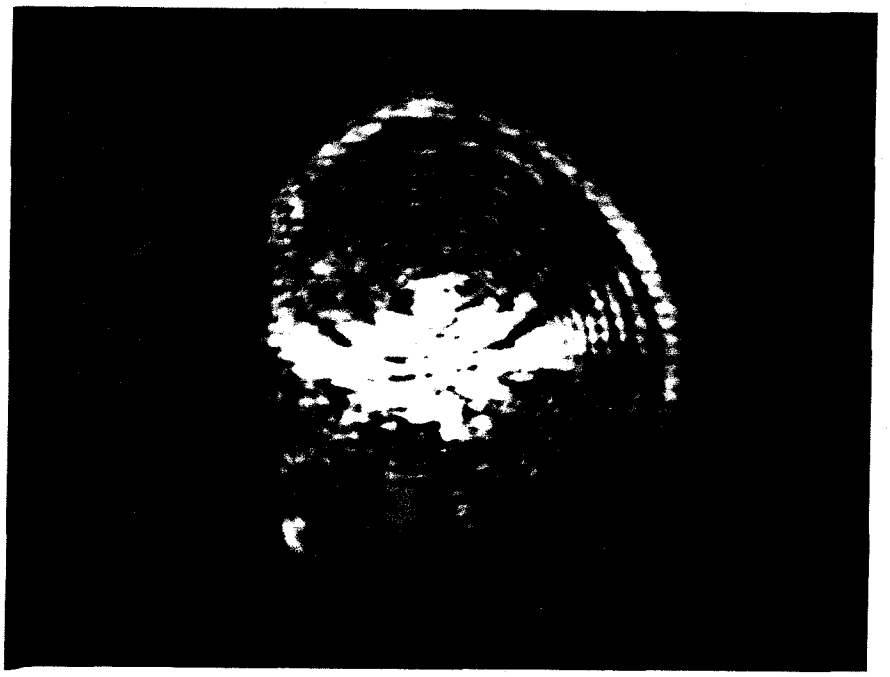

(d) Beam obtained when PPCM is replaced by an ordinary mirror.

photograph of the phase conjugate reflected beam and shows that it is indeed corrected of virtually all wavefront distortions. For comparison, Figure 7.6(d) shows the profile of the same Gaussian beam reflected back through the nonlinear distortion by an ordinary mirror rather than a PPCM.

Hence, it was shown both theoretically and experimentally that optical self-focusing and self-phase modulation effects can be compensated to a high degree by phase conjugation. Since the thermal conductivity of the photorefractive crystals was large enough to prevent high frequency thermal grating from forming, it was possible to demonstrate the above results with a self-pumped phase conjugator.

These results should be of importance to research in areas such as atmospheric propagation of high power laser beams, thermally induced lensing effects within intra-cavity laser gain media, and high intensity transmission through optical fibers and crystals.

7.2 Self-starting Passive Phase Conjugate Mirror with Ce-doped Strontium Barium Niobate

Two-beam coupling in photorefractive crystals has been used to demonstrate passive phase conjugate mirrors which do not require external pump beams[9,1,2,]. A more recent version of such a device[3,10,11] introduces an important simplification by using total internal reflection in the

photorefractive crystal instead of external mirrors. Such a mirror, however, requires a higher coupling threshold than that of the earlier devices. In this section, the construction of this phase conjugate mirror using cerium-doped strontium barium niobate photorefractive crystals as the holographic four-wave mixing media is described.

The experimental setup for studying phase conjugation with SBN is shown in Figure 7.7. Initially the lenses and transparency were removed so that the response of the phase conjugate mirror could be studied with a simple Gaussian beam. The reflectivity of two mirrors, one with Ce-doped SBN:60 and the other with Ce-doped SBN:75, is given in Figure 7.8 as a function of time. Not only do the data of Figure 7.8 show that phase conjugation using internal reflection is possible with SBN, but also that the steady-state phase conjugate reflectivity measured with Ce-doped SBN:75 is comparable to the 30% reflectivity obtained with $BaTiO_3$[3]. A photograph of the SBN:75 phase conjugator in operation is shown in Figure 7.9.

The imaging characteristics of the SBN phase conjugator were also determined with the arrangement shown in Figure 7.7, but now with the transparency and lenses in place. The transparency, an Air Force resolution chart, was illuminated by the argon ion laser and focused onto the crystal by the lenses. The phase conjugate reflection was picked off by the beamsplitter and projected onto the screen. Figures 7.10(a) and 7.10(b) show the resolution chart and the phase conjugate

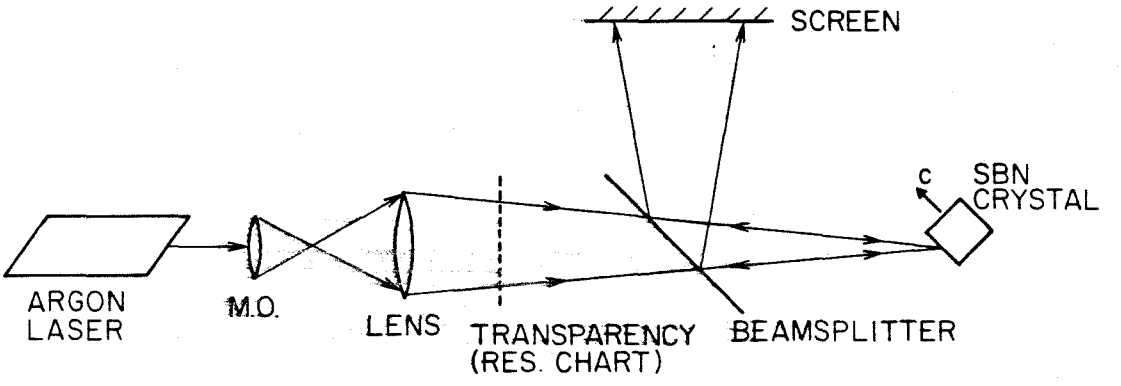

Figure 7.7. Experimental set-up for studying phase conjugation with SBN.

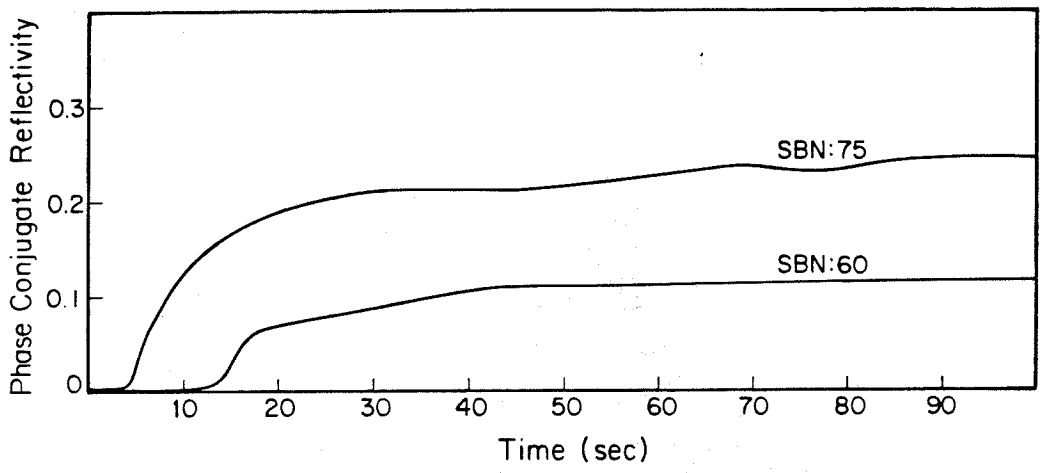

Figure 7.8. Phase conjugate reflectivities of the SBN phase conjugators as a function of time. Pump beam power density was approximately 1.5 W/cm^2.

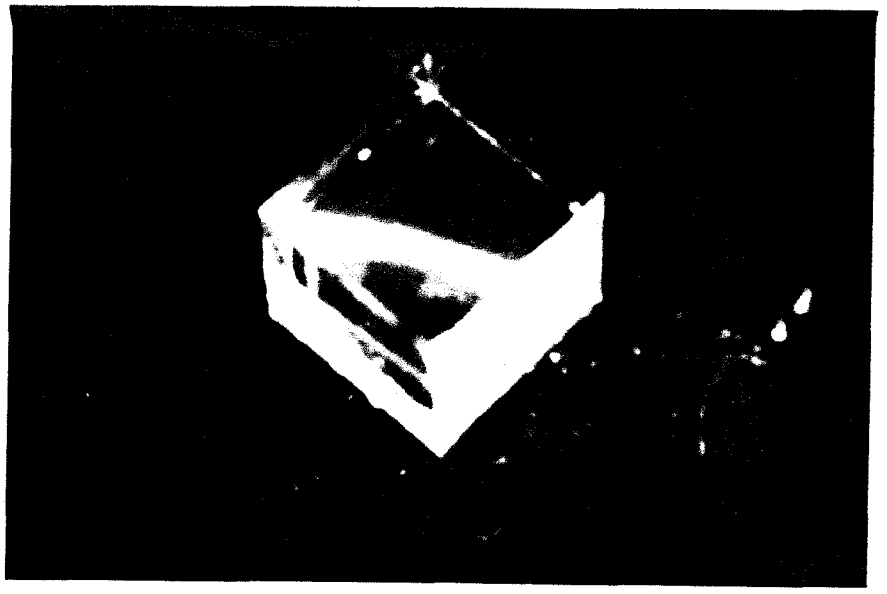

Figure 7.9. Photograph of the lightly Ce-doped SBN:75 mirror in operation.

Figure 7.10.

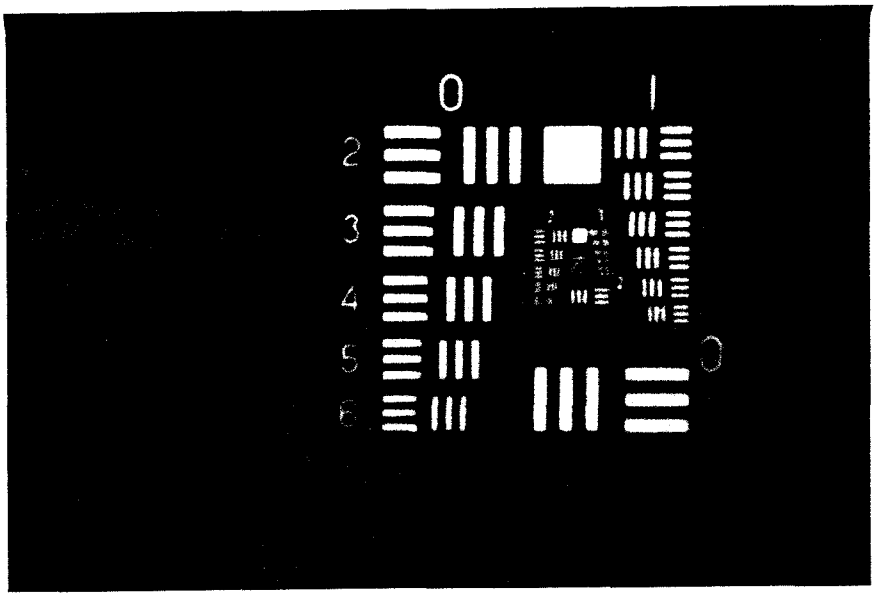

(a) Air Force resolution chart.

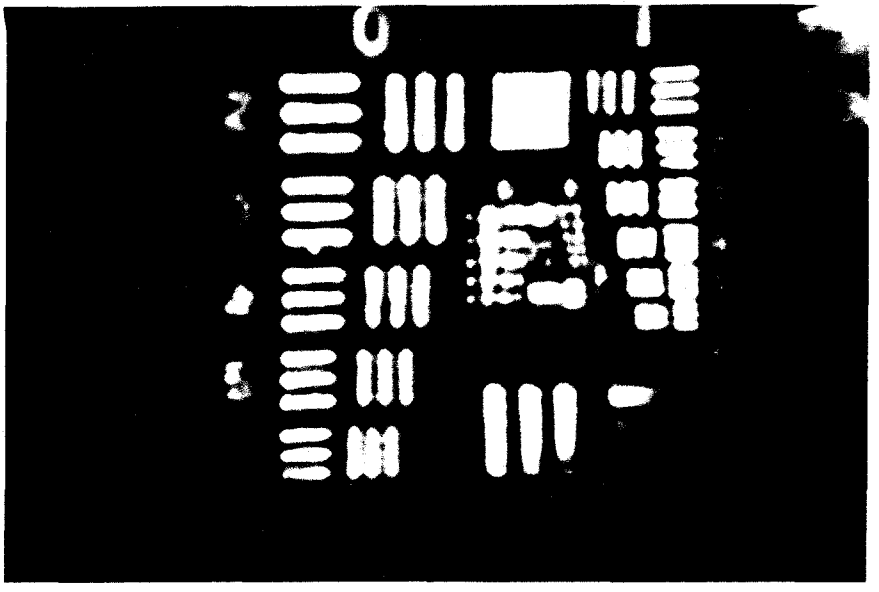

(b) Phase conjugate image of the resolution chart.

Figure 7.10. (Continued)

(c) Image of the resolution chart with distortion.

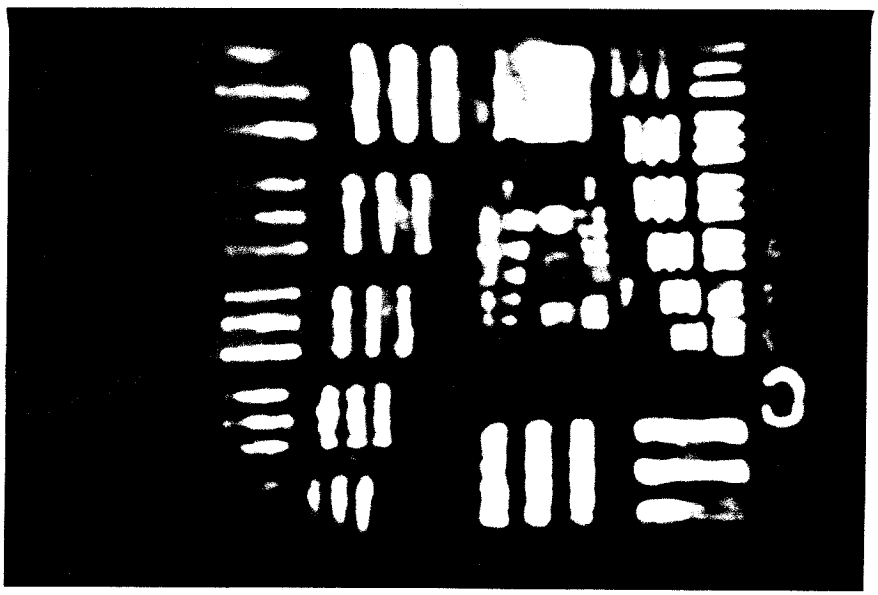

(d) Phase conjugate image of the resolution chart with distortion.

image of the chart. Next a phase distortion was placed between the transparency and the crystal, which, as shown in Figure 7.10(c), rendered the chart indiscernible, and the phase conjugate image was once again viewed as it was projected onto the screen. Since the phase conjugate wavefront at the crystal surface is that of the resolution chart after passing through the distortion, but with time reversal, the beam emerging from the distortion is the original undistorted image of the chart. This distortion correcting property of the SBN phase conjugator is shown in Figure 7.10(d).

In summary, it was shown that the self-starting passive phase conjugate mirror using internal reflection can be constructed with cerium-doped strontium barium niobate. Phase conjugate reflectivities of 25 and 12%, not corrected for Fresnel reflections, were measured with Ce-doped SBN:75 and SBN:60, respectively. The imaging and distortion correcting properties of the SBN phase conjugator were also demonstrated.

7.3 Thresholding Semilinear Phase Conjugate Mirror

Phase conjugate mirrors have been used as nonlinear thresholding devices by using background illumination, pump depletion, semi-self-pumped phase conjugation, and optical bistability[12-15]. The background illumination and semi-self-pumped phase conjugation schemes were self-pumped phase conjugate mirrors which ideally generated the phase

conjugate of the incident beam if its intensity was above a threshold I_{th} and no output if it was less than I_{th}. Both of these configurations rely on an external reference beam that determines the threshold intensity[12,13]. In this section, a different method is demonstrated for obtaining phase conjugate thresholding - by using a moving grating inside the photorefractive crystal and relying on the dependence of photorefractive response time on the incident beam intensity to vary the coupling constant γl.

The basic semilinear phase conjugate mirror configuration has been described in earlier works and is illustrated in Fig. 7.11[1,16]. It is a passive device, relying only on the incident beam to generate the phase conjugate of that beam. Light scattered and amplified by the fanning effect is reflected back into the crystal by external mirror. The grating in the crystal is formed by the light interference pattern between this reflected fanning beam and the incident beam. Since the phase of the light interference pattern is a direct function of the optical path difference of the two beams, the grating can be translated by ramping the phase of the light reflected by the external mirror. In the experiment, this was done by varying continuously the optical path length traveled by the reflected fanning beam. The external mirror was mounted on a piezo-electric micrometer, and a high voltage ramp was applied to the device to translate it at a constant velocity.

The reflectivity of a semilinear phase conjugate mirror

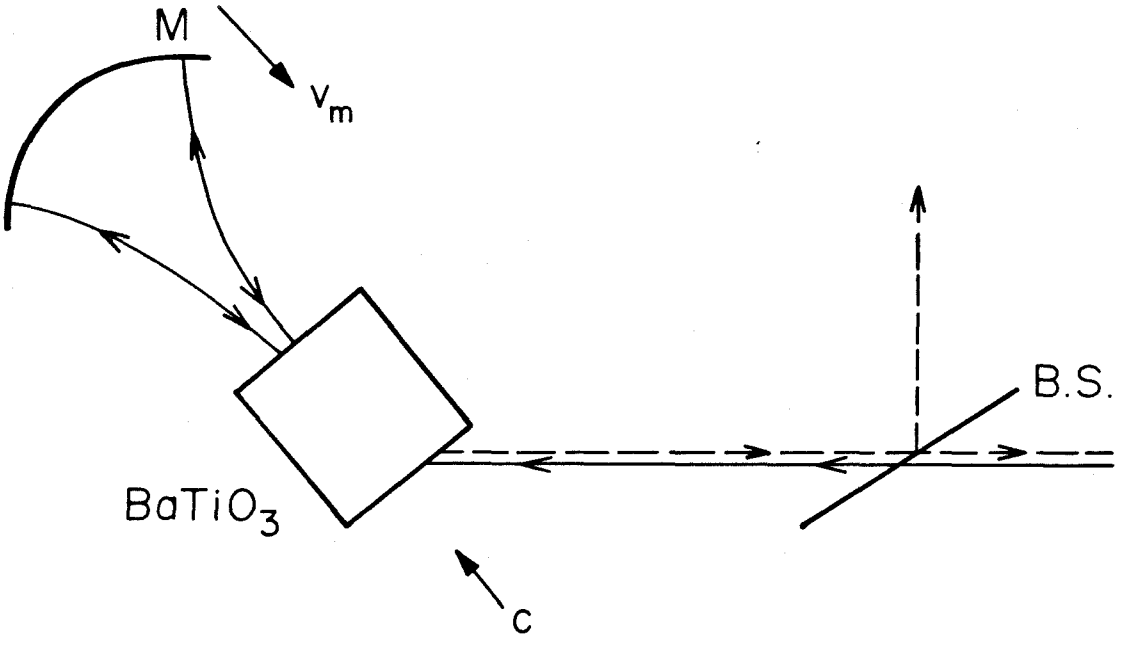

Figure 7.11. Configuration for a semilinear self-pumped phase conjugate mirror. The external mirror M is mounted on a piezoelectric micrometer to move it towards the $BaTiO_3$ crystal.

is given by[1]

$$R = \left(\frac{M^{1/2} + [a^2(1+M)-1]^{1/2}}{M+2-M^{1/2}[a^2(1+M)-1]^{1/2}} \right)^2$$

where M is the reflectivity of the external mirror, and a is related to the coupling constant γl by

$$\tanh(-\tfrac{1}{2}\gamma l a) = a \qquad [7.12]$$

There exists a threshold value $(\gamma l)_{th}$ of the coupling constant defined by

$$a_{th}^2 = \frac{1}{1+M} = \tanh^2\left[-\frac{1}{2}(\gamma l)_{th} a \right]$$

for which $R_{th} = \frac{M}{(M+2)^2} \simeq 1/9$ for $M \simeq 1$, but can be made significantly smaller by choosing $M<1$. The result is that R will be high for γl above $(\gamma l)_{th}$, while $R \to 0$ for γl below the threshold; in other words, the mirror phase conjugates essentially only for $I>I_{th}$.

If the external mirror is stationary, the effective coupling constant will be above threshold, the grating will build up after some finite time interval, and the semilinear mirror will produce a phase conjugate output. This time constant τ depends on the intensity of the incident beam. When the mirror is moved, the reflected light is Doppler shifted by $\delta\omega$, causing the interference pattern in the crystal to move with a velocity $v = \frac{c\delta\omega}{2\omega\sin(\theta/2)}$, where θ is the angle between the incident and fanning beams, so that the grating period is $\lambda_g = \frac{\lambda}{2\sin(\theta/2)}$. The dependence of the effective coupling constant γl on the parameters of interest

here is given by (see Eq. [3.7])

$$\gamma l = (\gamma l)_0 F(I,\tau,v) \qquad [7.14]$$

where I is the total intensity of the incident plus any background erase beam, τ is the time constant of the crystal, and v is the velocity of the light interference pattern inside the crystal. Specifically, this dependence is given by

$$\gamma l \;\alpha\; \Delta n_{grating} = \left(\frac{\Delta n_0}{1+\alpha I}\right)\left(\frac{1}{1+i\,\frac{2\pi v\tau}{\lambda g}}\right)$$

$$= \left(\frac{\Delta n_0}{1+\alpha I}\right)\left[\frac{1}{1+i(\tau\delta\omega)}\right]$$

where α is some constant.

Figure 7.12 shows the reflectivity of the semilinear mirror versus incident power of the unexpanded Gaussian beam from an argon-ion laser. The piezo-electric micrometer was driven by the ramp generator over a distance of 4 microns at velocities ranging from 180 to 392 Å/sec. With no mirror motion, the threshold was at I = 2 mW. This nonzero value is probably due to some dark conductivity term in the coupling constant. As the mirror velocity was increased, the threshold level I_{th} shifted to higher levels. Defining the threshold intensity somewhat arbitrarily as I_{th} such that $R(I_{th}) = 1/2\ R_{max}$, I_{th} as a function of mirror velocity v is shown plotted in Fig. 7.13.

This device has potential applications in optical associative memories where it is necessary to selectively phase conjugate only the stronger modes among many in an optical resonator. It also has potential applications in

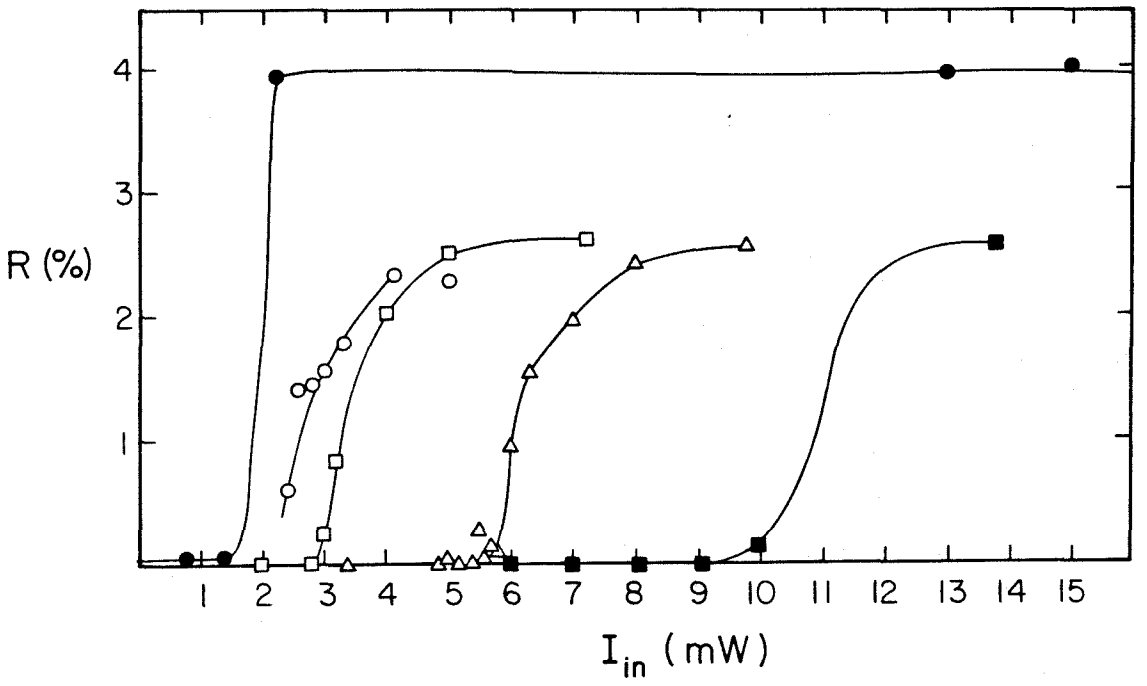

Figure 7.12. Reflectivity versus incident intensity of the thresholding semilinear mirror for various mirror velocities. Values of v_m are, from the left, 0, 18.0, 23.2, 31.5, and 39.2 nm/sec.

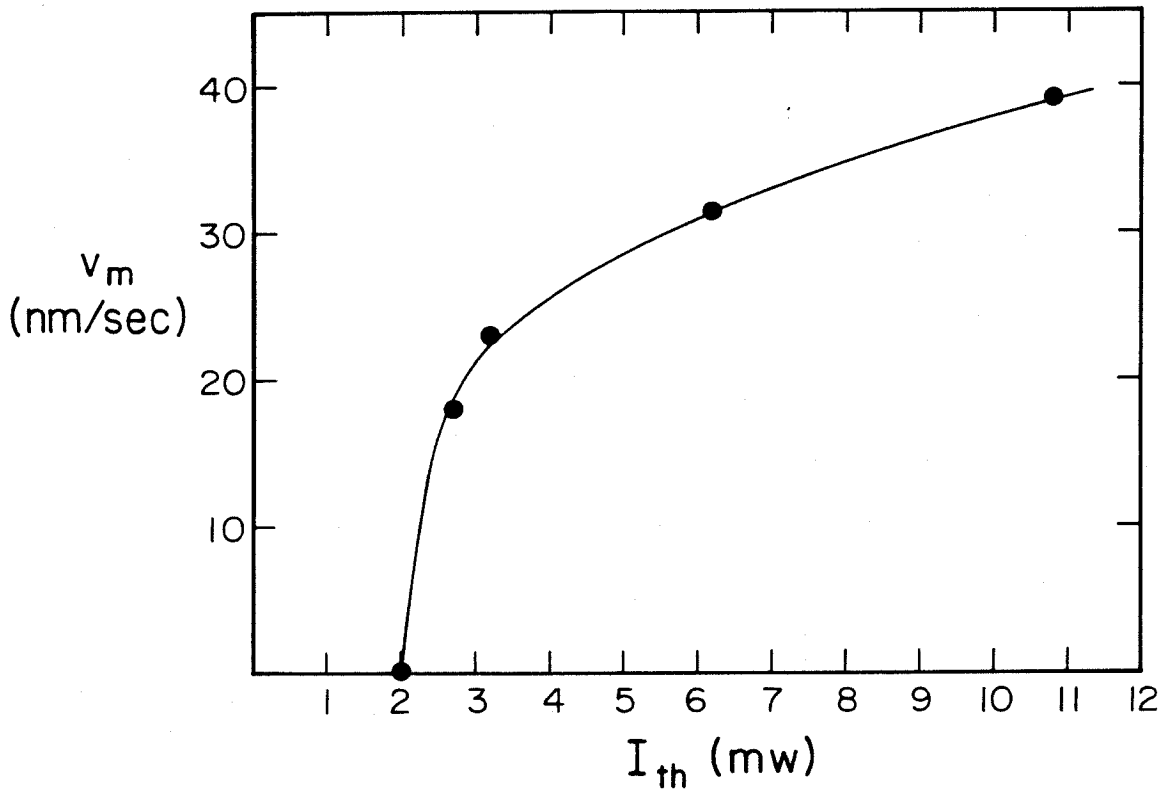

Figure 7.13. Thresholding intensity as a function of mirror velocity.

optical signal processing and switching.

In summary, a method was demonstrated for obtaining optical thresholding in a passive semilinear phase conjugate mirror. This method relies on grating motion in the photorefractive medium introduced by motion of the external mirror and the incident beam intensity dependence of the photorefractive coupling constant. The threshold intensity I_{th} can be selected by varying the mirror translation velocity.

7.4 Mathematical Operations on Images

Photorefractive crystals have been used to perform various real-time image processing operations. For example, real-time convolution and correlation[17], edge enhancement[18], image subtraction[19,20], differentiation[21], division[22], and inversion[23] have been demonstrated. In this section several devices are described that perform mathematical operations on images. An interferometer using a self-pumped phase conjugate mirror is presented in section 7.4.1 which produces the real-time "exclusive or" operation and image subtraction[24,25]. In sections 7.4.2 and 7.4.3. intensity inversion and image differentiation are described. Extensions of these devices to perform higher order differentiation and the Laplacian operation are also discussed.

7.4.1 Real-time "exclusive or" operation and image subtraction

Fig. 7.14 illustrates the system for "exclusive or" operation. A plane wave with amplitude E_{in} is split by beam splitter BS_1 whose reflection and transmission coefficients are equal to r and t, respectively. Without making any assumptions, let r' and t' be the amplitude reflection and transmission coefficients for wave incident from the opposite sides of the beamsplitter. Each of the two resultant waves then passes through a transparency with amplitude transmittance T_1 for beam 1 and T_2 for beam 2. The two beams are then reflected by a self-pumped phase conjugate mirror with phase conjugate amplitude reflectivities R_1 and R_2 for beam 1 and beam 2 respectively (R_1 and R_2 are in general not the same). The phase conjugated beams recombine interferometrically at beam splitter BS_1 to form an output field intensity I_{out} at detector D_1 given by

$$I_{out} = \left| r't^*R_1\left|T_1\right|^2 + tr^*R_2\left|T_2\right|^2\right|^2 I_{in}, \qquad [7.16]$$

where $I_{in} = \left|E_{in}\right|^2$.

From Stokes' principle of the time reversibility of light

$$r't^* + r^*t = 0, \qquad [7.17]$$

so that

$$I_{out} = \left|R_1\left|T_1\right|^2 - R_2\left|T_2\right|^2\right|^2 \left|r^*t\right|^2 I_{in}. \qquad [7.18]$$

If the two phase conjugate reflectivities are identical, i.e. $R_1 = R_2 = R$, then

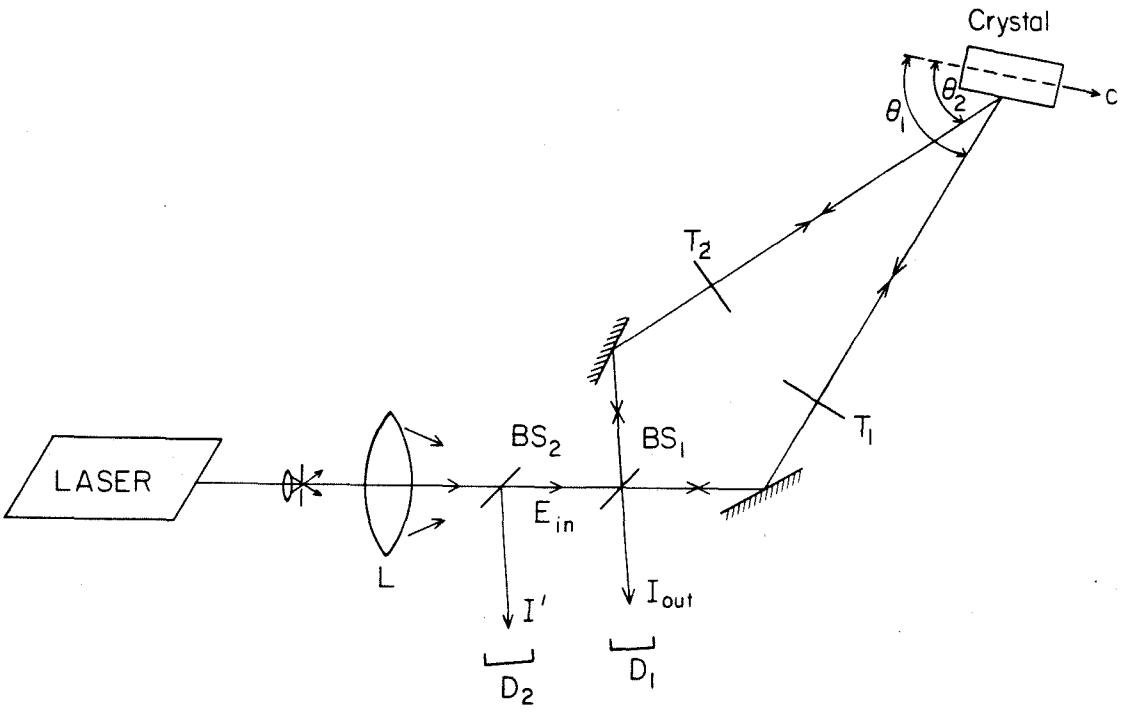

Figure 7.14. Experimental arrangement to demonstrate the "exclusive or" operation.

$$I_{out} = \left| |T_1|^2 - |T_2|^2 \right|^2 |r^* t R|^2 \, I_{in}$$
$$\alpha \; |T_1|^2 \oplus |T_2|^2 \qquad [7.19]$$

where $\oplus$ represents the Boolean "exclusive or" operation. This is the main result. Similarly, the field intensity I' measured by detector D_2 is

$$I' \; \alpha \left| |T_1|^2 + |r|^2 (|T_2|^2 - |T_1|^2) \right|^2 |R|^2 \, I_{in} \qquad [7.20]$$

The π phase shift between the complex fields of the two images, which is the key element of the "exclusive or" operation, is introduced naturally by the time reversibility of light. This is the essential difference between this method and other methods[19,20] in which the π phase shift was artificially provided by a piezo-electric mirror or an electrooptical modulator. This device is only sensitive to intensity differences of the two transparencies and is independent of the phase information of the transparencies or the optical path lengths of the two arms.

In the experiment, a single TEM_{00} mode argon laser beam (5145A, 50mW) was expanded and split into two beams by 50% beam splitter BS_1. Each beam was then passed through separate transparencies T_1 and T_2. A lens L (f=30cm) was used to focus the two expanded beams which were adjusted to overlap completely inside the poled $BaTiO_3$ crystal. The crystal was then aligned to form a self-pumped phase conjugate mirror by setting the angles between the beams and the crystal c-axis to $\theta_1 = 50^\circ$ and $\theta_2 = 40^\circ$. The two image bearing beams were phase conjugated simultaneously with no cross talk[11]. The magnitude of the phase conjugate

reflectivities of beam 1 and beam 2 were approximately the same and equal to 25%. The phases of the complex phase conjugate reflection coefficients of the two beams were also the same, since the PPCM regarded the combination of the two input beams as a single complex input wave, and since the beams overlapped in the crystal, they were both reflected from the same set of gratings[26]. The phase conjugate reflected image bearing beams were then combined interferometrically at the beam splitter BS_1. The two transparencies and the detectors were placed in close to the beam splitters to reduce diffraction aberration.

The transparencies T_1 and T_2 used in the experiment were pictures of a semicolon and a colon, respectively. The phase conjugate images of these two transparencies are shown in Figs. 7.15(a) and 7.15(b), respectively. Fig. 7.15(c) is the image detected by D_1, which represents the "exclusive or" operation (or, in this case, image subtraction) between the two images, $|T_1|^2 \oplus |T_2|^2$. Fig. 7.15(d) is the image recorded by D_2, which represents $\left| |T_1|^2 + |r|^2 (|T_2|^2 - |T_1|^2) \right|^2$, and it is proportional to the sum of intensities, $\left| |T_1|^2 + |T_2|^2 \right|^2$, when $|r|^2 = .5$. Slight edge enhancement effects[18] were also observed in these figures, which are probably due to large object beam intensities as compared to the weaker pump intensities. These results are independent of the optical path lengths of either beam between the BS_1 and the crystal.

The response time of the self-pumped phase conjugate mirror obeyed approximately the relation $\tau \simeq 10/I$ s, where I

Figure 7.15.

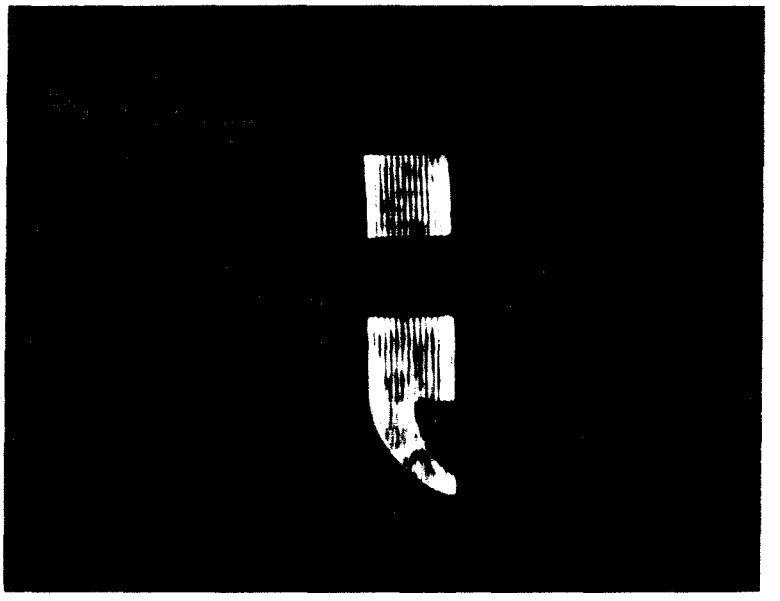

(a) Image of the semicolon after phase conjugation.

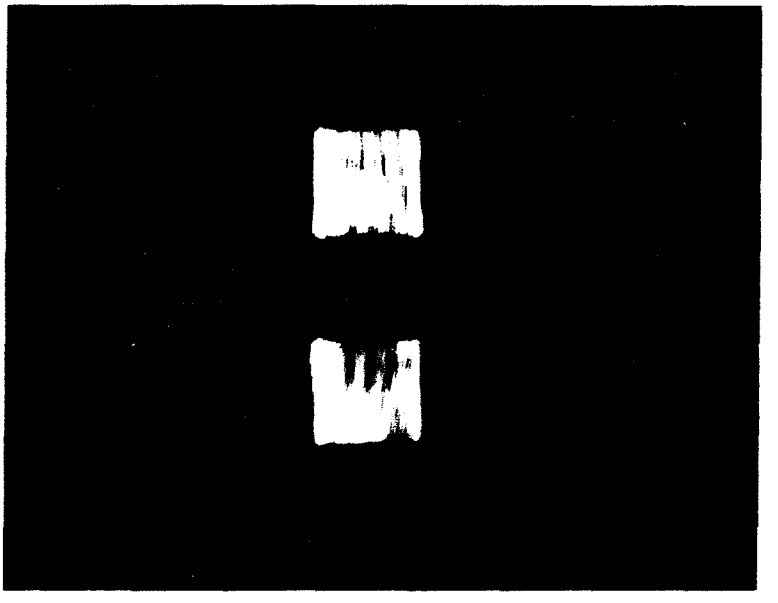

(b) Image of the colon after phase conjugation.

Figure 7.15. (Continued)

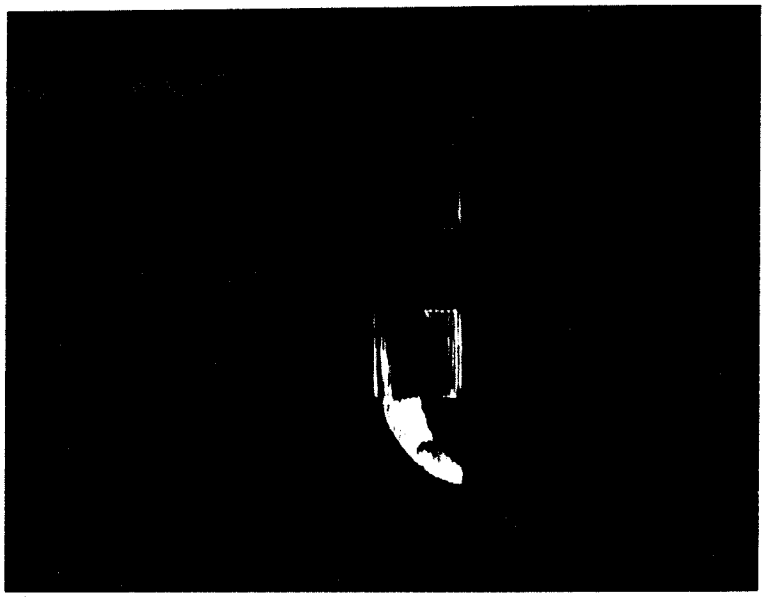

(c) Image subtraction of the semicolon and the colon.

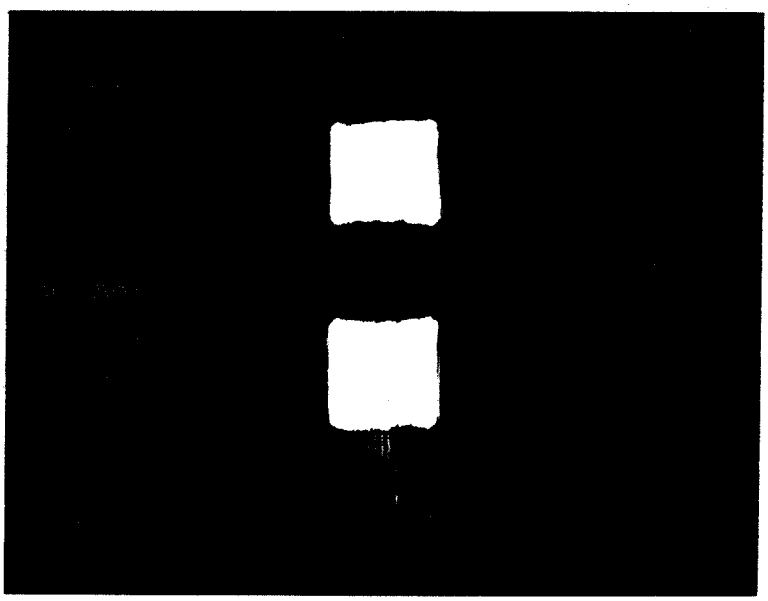

(d) Image detected by detector D_2.

is the total intensity of the interaction beams in mW/mm^2.

7.4.2 Real-time intensity inversion

Optical intensity was also observed by simply removing transparency T_2 so that the intensity detected by D_1 is proportional to $\left|1-|T_1|^2\right|^2$, whose result follows from Eq. 7.19 with $|T_2|^2=1$. Figs.7.16(a) and 7.16(b) are the phase conjugate images of a uniform illumination and a resolution chart, respectively. Fig. 7.16(c) is the intensity inverted image detected by D_1. Fig. 7.16(d) is the image addition observed by detector D_2, which is proportional to $\left|1+|T_1|^2\right|^2$.

Intensity inversion by a different method which uses four wave mixing was reported recently by Ochoa et al[23]. In their method the object beam intensity is required to be much higher than that of the reference beam in order to ensure that the diffraction efficiency of the index grating is inversely proportional to the object beam intensity.

7.4.3 Real-time image differentiation

The differential of a function I(x,y) can be approximated to any degree of accuracy by using finite differences. Using such a method, the first and second-order differentials are given by

$$\frac{\partial I(x,y)}{\partial x} = \frac{I(x+\Delta x,y)-I(x,y)}{\Delta x}$$

$$\frac{\partial^2 I(x,y)}{\partial x^2} = \frac{I(x+\Delta x,y)-2I(x,y)+I(x-\Delta x,y)}{(\Delta x)^2}$$

Therefore, the differential of any order can be obtained

Figure 7.16.

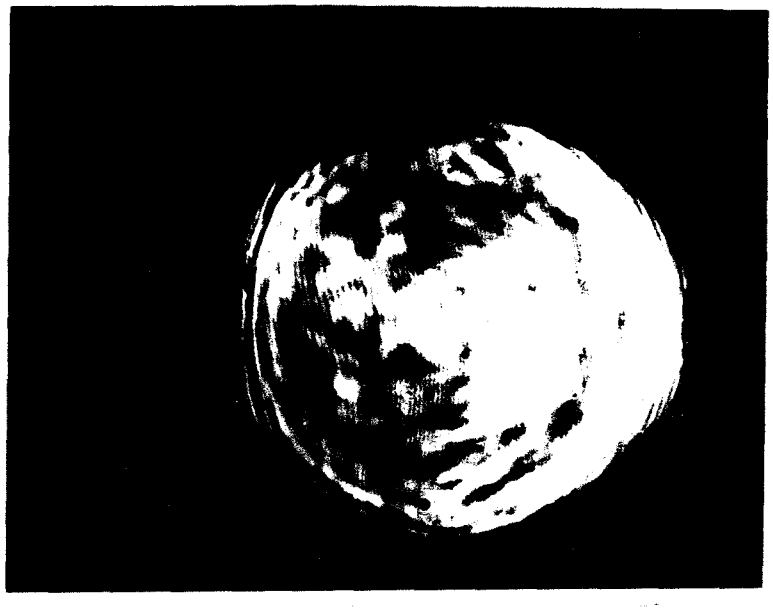

(a) Image of the uniform illumination after phase conjugation.

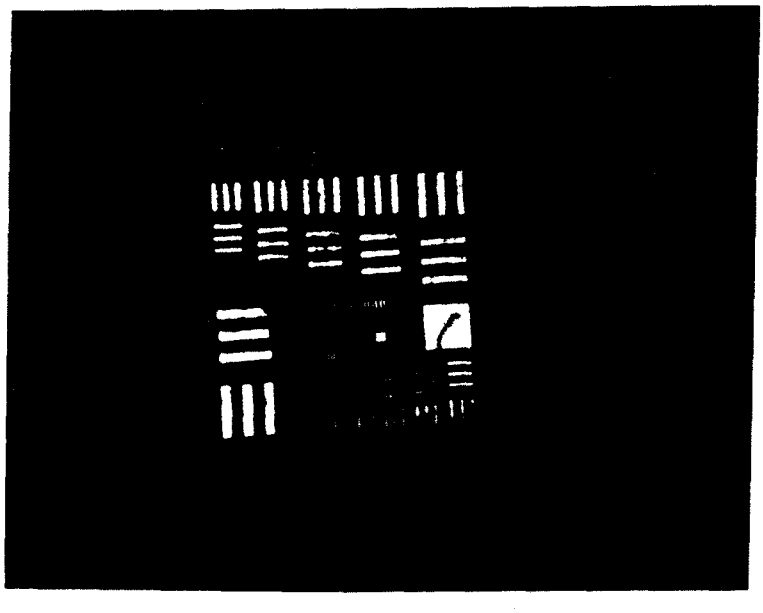

(b) Image of the resolution chart after phase conjugation.

Figure 7.16. (Continued)

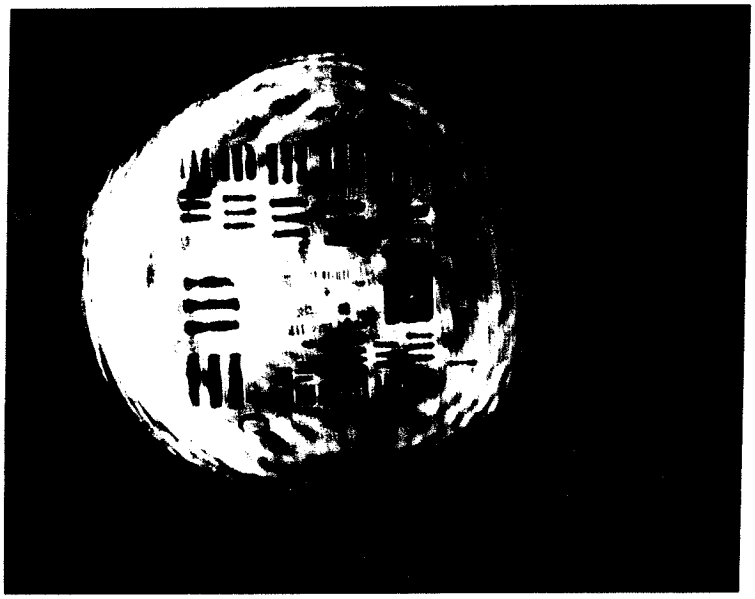

(c) Intensity inversion of the resolution chart.

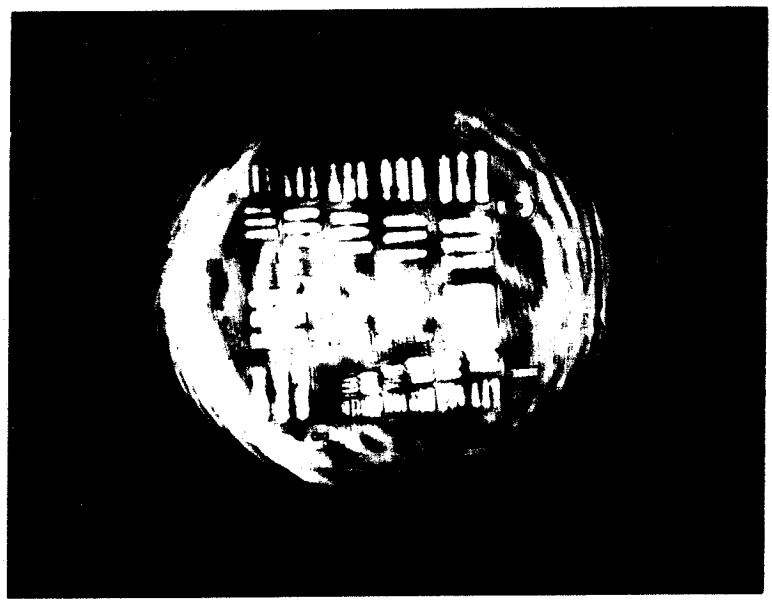

(d) Intensity addition of the resolution chart and the uniform illumination.

by adding and subtracting various shifted images of a pattern function.

The experimental arrangement used to perform first-order differentiation, which is very similar to Fig. 7.14, is shown in Fig. 7.17. Since the transparency is not placed at the intersection of the two beams, each beam reads a slightly shifted image of the other. The two images are then focused down into the $BaTiO_3$ crystal which through total internal reflection forms a self pumped phase conjugate mirror. The phase conjugate images are thus phase locked and can recombine at BS_1, giving an output amplitude which is proportional to the first order differential. Results are given in Fig. 7.18. Also given in Fig. 7.18(d) is $(\partial/\partial x + \partial/\partial y)$ obtained by shifting the images by $\Delta x + \Delta y$.

Fig. 7.19 gives the set up used to perform second-order image differentiation. The two outside beams read $T(x+\Delta x,y)$ and $T(x-\Delta x,y)$, while the center beam reads $T(x,y)$. The reflectivity of beam splitter BS_2 is 50%, giving an output amplitude at BS_1 proportional to the second order differential.

$$I_{out} \alpha \left| |T(x+\Delta x,y)|^2 + |T(x-\Delta x,y)|^2 - 2|T(x,y)|^2 \right|^2 \qquad [7.23]$$

Results are given in Fig. 7.20.

Extensions to higher order image differentiation can be obtained by adding up approximately shifted images into two groups which are then subtracted at the final beam splitter. While the final beam splitter reflectivity can be arbitrary the remaining ones must have their reflectivities chosen to

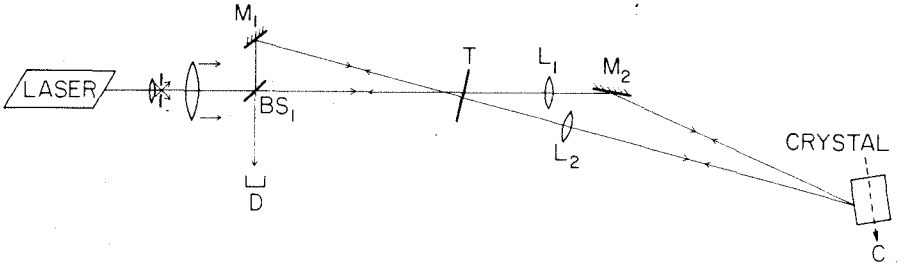

Figure 7.17. Experimental arrangement used to demonstrate first order image differentiation.

Figure 7.18.

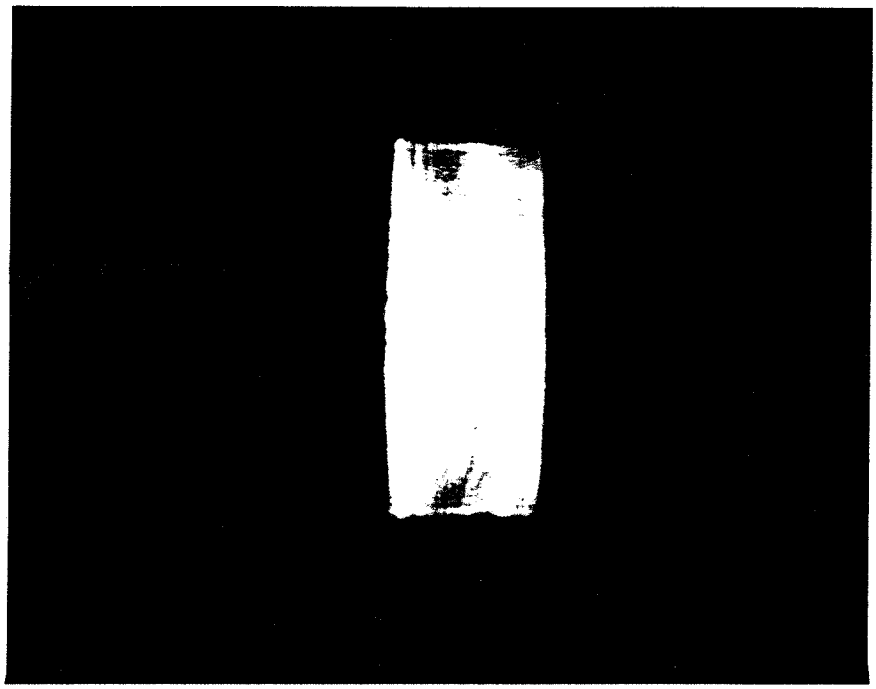

(a) Image of a rectangle after phase conjugation.

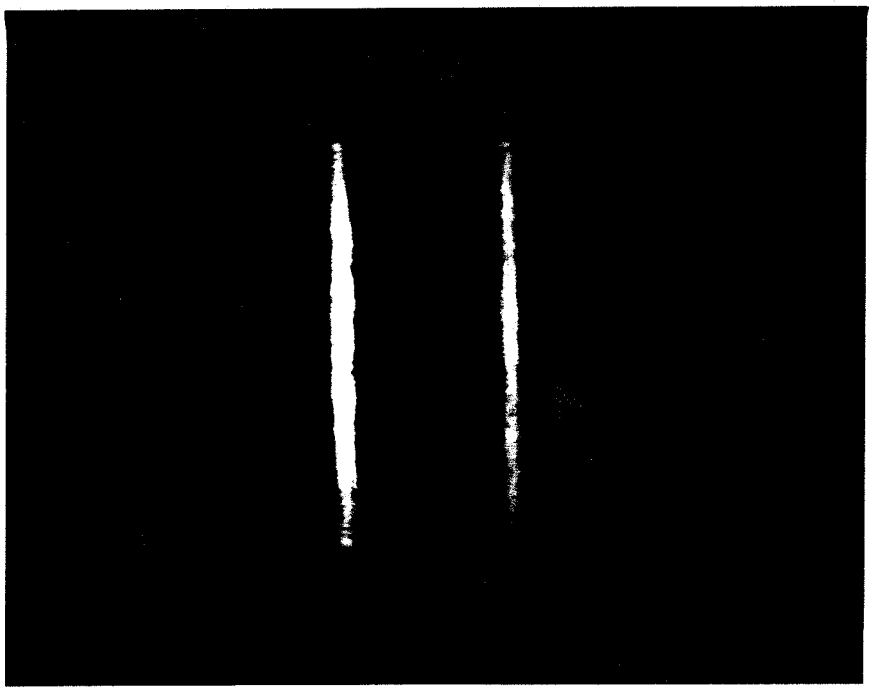

(b) Image of Fig. 7.18(a) after first order differentiation.

Figure 7.18. (Continued)

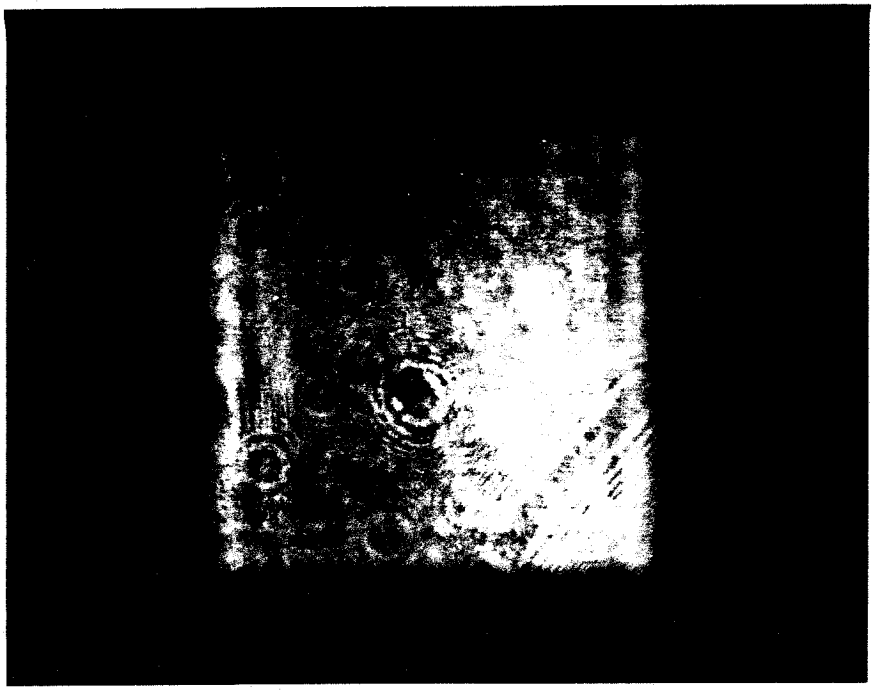

(c) Image of a square after phase conjugation.

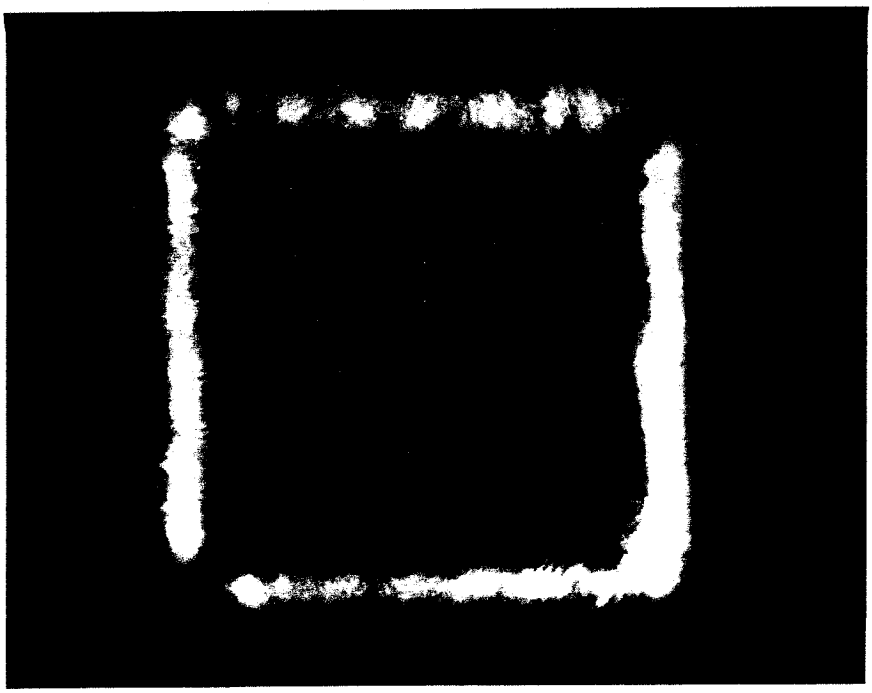

(d) Image of Fig. 7.18(c) after d/dx + d/dy operation.

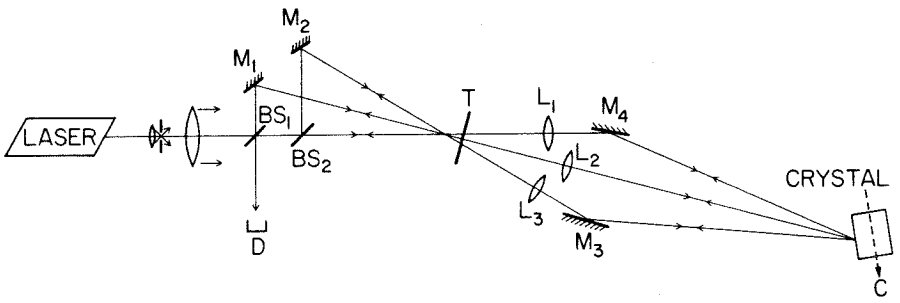

Figure 7.19. Experimental arrangement used to demonstrate second order image differentiation.

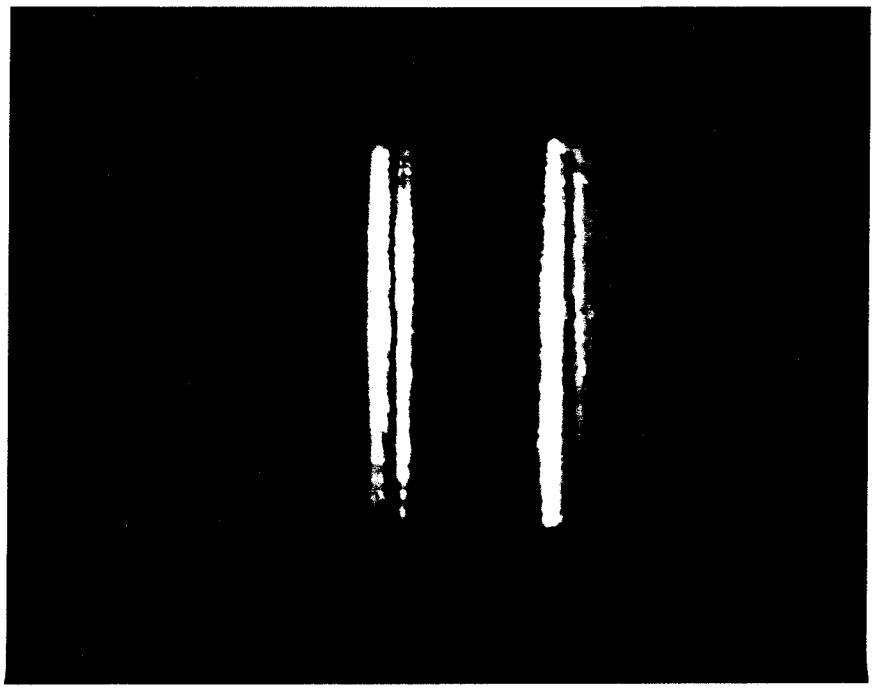

Figure 7.20. Image of Fig. 7.18(a) after second order differentiation.

perform the image additions in the correct proportions. The many shifted images required for higher order derivatives may cause difficulties in focusing all the images into a single crystal. In that case two or more crystals phase locked through spontaneous oscillations[26] could be used to handle the many images. Efforts are also under way to couple the multiple images into the crystal using a single optical fiber.

Using methods similar to those used for image differentiation a device can be constructed whose output amplitude is proportional to $\nabla^2 I(x,y)$, where $I=|T(x,y)|^2$. A beam is expanded and split into two beams. One of the beams will read T(x,y). The other beam will be split into four beams of equal intensity using 50% beam splitters. These beams will then read images of T(x,y) shifted by $\pm\Delta x$ or $\pm\Delta y$. These beams will then recombine at the first beam splitter giving an output proportional to $\nabla^2 I(x,y)$.

7.5 References

1. M. Cronin-Golomb, B. Fisher, J. O. White, and A. Yariv, Appl. Phys. Lett. 41, 689 (1982).

2. M. Cronin-Golomb, B. Fischer, J. O. White, and A. Yariv, Appl. Phys. Lett. 42, 919 (1983).

3. J. Feinberg, Opt. Lett. 7, 486 (1982).

4. G. A. Rakuljic, K. Sayano, A. Yariv, and R. R. Neurgaonkar, App. Phys. Lett. 50, 10 (1987).

5. B. Fischer, M. Cronin-Golumb, J. O. White, and A. Yariv, Appl. Phys. Lett. 41, 141 (1982).

6. Optical Phase Conjugation, (Ed. R. A. Fisher, Academic Press, New York, 1983).

7. M. Cronin-Golumb, B. Fischer, J. O. White,and A. yariv, IEEE Journ. Quant. Electron. QE-20, 12 (1984).

8. D. M. Pepper and A. Yariv, Opt. Lett. 5, 59 (1980).

9. J. O. White, M. Cronin-Golumb, B. Fischer, and A. Yariv, Appl. Phys. Lett. 40, 450 (1982).

10. K. R. MacDonald and J. Feinberg, J. Opt. Soc. Am. 73, 548 (1983).

11. J. Feinberg, Opt. Lett. 8, 480 (1983).

12. M. Cronin-Golumb and A. Yariv, Technical Digest, Optical Society of America Annual Meeting, Seattle, WA, 1986, paper MM1.

13. M. B. Klein, G. J. Dunning, G. C. Valley, R. C. Lind, and T. R. O'Meara, Technical Digest, Conference on Lasers and Electro-optics, Washington D.C., 1985, paper PD5.

14. S. K. Kwong, M. Cronin-Golomb, and A. Yariv, Appl. Phys. Lett. 45, 1016 (1984).

15. S. K. Kwong and A. Yariv, Opt. Lett. 11, 377 (1986).

16. M. Cronin-Golumb, B. Fischer, J. Nilsen, J. O. White, and A. Yariv, Appl. Phys. Lett. 37, 5 (1980).

17. J. O. White and A. Yariv, Appl. Phys. Lett. 37, 5 (1980).

18. J. Feinberg, Opt. Lett. 5, 330 (1980).

19. J. P. Huignard, J. P. Herriau, and F. Micheron, Appl. Phys. Lett. 26, 256 (1975).

20. Y. H. Ja, Opt. Commun. 42, 377 (1982).

21. Y. H. Ja, Appl. Phys. B, 36, 21 (1985).

22. Y. H. Ja, Opt. Commun. 44, 24 (1982).

23. E. Ochoa, L. Hesselink, and J. W. Goodman, Appl. Opt. 24, 1826 (1985).

24. S. K. Kwong, G. A. Rakuljic, and A. Yariv, Appl. Phys. Lett. 48, 201 (1986).

25. S. K. Kwong, G. A. Rakuljic, V. Leyva, and A. Yariv, Proc. SPIE 613, 36 (1986).

26. In M. D. Ewbank, P. Yeh, M. Khoshnevisan, and J. Feinberg, Opt. Lett. 10, 282 (1985), another method for obtaining phase locking between the two phase conjugate beams is described in which a self-induced oscillation locks the relative phase between the two phase conjugate beams.